



Review

# A Comprehensive Review of High-Pressure Laser-Induced Materials Processing, Part III: Laser Reactive Synthesis within Diamond Anvil Cells

Mohamad E. Alabdulkarim , Wendy D. Maxwell, Vibhor Thapliyal and James L. Maxwell \*

Department of Engineering (E $\epsilon$ MC<sup>2</sup> Labs), La Trobe University, Bendigo, VIC 3550, Australia

\* Correspondence: j.maxwell@latrobe.edu.au

**Abstract:** The synthesis of advanced materials at high pressures has been an area of growing research interest for several decades. This article is the third in a three-part series that reviews *Laser Materials Processing Within Diamond Anvil Cells* (L-DACs). Part III focuses on the practice of *Laser Reactive Synthesis Within Diamond Anvil Cells* (LRS-DAC). During LRS-DAC processing, chemicals are precompressed within diamond anvil cells, then *microscale chemical reactions* are induced by focused laser beams. The method is distinguished from the well-known *Laser-Heated Diamond Anvil Cell* (LH-DAC) technique (see Part I) through the existence of chemical precursors (reactants), end-products, and quantifiable changes in *chemical composition* upon reaction. LRS-DAC processing provides at least three new degrees of freedom in the search for advanced materials (beyond adjusting static pressures and temperatures), namely: laser-excitation/cleavage of chemical bonds, time-dependent reaction kinetics via pulsed lasers, and pressure-dependent chemical kinetics. All of these broaden the synthetic phase space considerably. Through LRS-DAC experimentation, it is possible to obtain increased understanding of high-pressure chemical kinetics—and even the nature of chemical bonding itself. Here, LRS-DAC experimental methods are reviewed, along with the underlying chemistry/physics of high-pressure microchemical reactions. A chronology of key events influencing the development of LRS-DAC systems is provided, together with a summary of novel materials synthesised, and unusual chemical reactions observed. Current gaps in knowledge and emerging opportunities for further research are also suggested.

**Keywords:** diamond anvil cell; laser deposition; chemical reaction; laser-induced reaction; selective deposition; materials synthesis; high pressure; additive manufacturing



**Citation:** Alabdulkarim, M.E.; Maxwell, W.D.; Thapliyal, V.; Maxwell, J.L. A Comprehensive Review of High-Pressure Laser-Induced Materials Processing, Part III: Laser Reactive Synthesis within Diamond Anvil Cells. *J. Manuf. Mater. Process.* **2023**, *7*, 57. <https://doi.org/10.3390/jmmp7020057>

Academic Editor: Steven Y. Liang

Received: 31 December 2022

Revised: 11 February 2023

Accepted: 22 February 2023

Published: 3 March 2023



**Copyright:** © 2023 by the authors. Licensee MDPI, Basel, Switzerland. This article is an open access article distributed under the terms and conditions of the Creative Commons Attribution (CC BY) license (<https://creativecommons.org/licenses/by/4.0/>).

## 1. Introduction

Recently, many novel advanced functional materials with emergent properties have been discovered under highly compressed conditions [1–5], such as high-temperature superconductors (HTS) [6], superhard compounds [7–12], ferroelectric materials [13], and high-thermal conductivity compounds [14,15]. Ongoing research includes high purity, single-crystal growth [16], and the synthesis of novel metal hydrides [6], borides [17,18], carbides [19,20], nitrides [21,22], oxides [23], and intermetallic compounds [24,25]. These useful materials were formed, not through the application of pressure or temperature alone, but through the combined actions of an incident laser beam and applied pressure.

One emerging high-pressure method is *Laser-Reactive Synthesis Diamond Anvil Cell* (LRS-DAC) experimentation. During *LRS-DAC investigations*, chemical precursors (or reactants) [i] are converted to desired product(s) [ii], within a region known as the *reaction zone* [iii] (See Figure 1). Often, precursor(s) and byproduct(s) [iv] are transported to/from this reaction zone across a region of the DAC's gasket chamber [v] that is filled with a pressure medium [vi]. The precursor may be a solid sample, may be mixed with the pressure medium, or may be the pressure medium itself. Similarly, when laser heating occurs, heat is transported away from the reaction zone to other portions of the gasket

chamber—ultimately conducting away from the chamber through the diamond anvils [vii] or gasket walls.

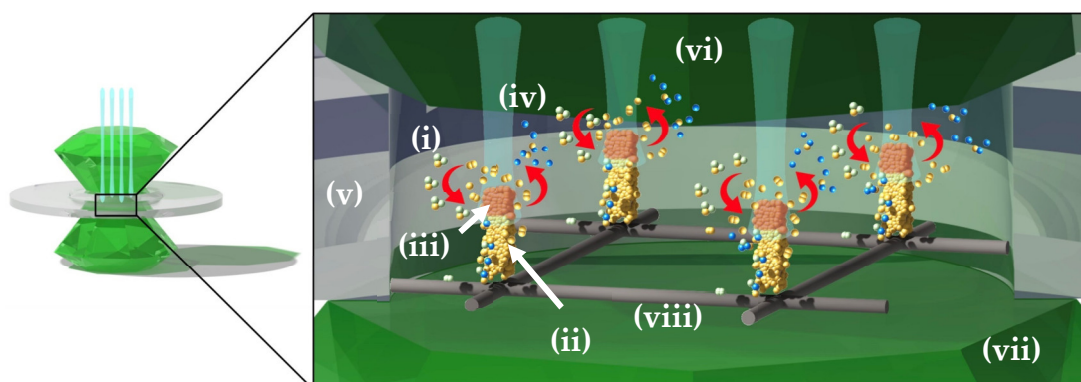


**Figure 1.** Illustration of the LRS-DAC method: (i) chemical precursor(s) (reactants) that transport to the reaction zone, (ii) the resulting product, (iii) the reaction zone where the incident laser interacts with the precursor(s), and (iv) byproducts of the reaction that may diffuse or segregate away from the product. Additional components include the (v) gasket chamber, (vi) pressure medium, and (vii) diamond anvils.

A key distinction between previously reviewed L-DAC modes and LRS-DAC experimentation is that the laser beam(s) are used in conjunction with high pressures to drive *purposeful chemical reactions*. Rather than (solely) modifying a sample material’s phase or microstructure, a new chemical composition is created. During *Laser-Heated Diamond Anvil Cell (LH-DAC)* experimentation, for example, samples are often heated to observe phase or structural transformations (see this review, Part I [26]), whereas changes to a sample’s chemical composition are frequently avoided. Sample contamination and reaction with adjacent materials has been the bane of many LH-DAC experiments [27–29]. At high temperatures, diffusion occurs more rapidly, and undesired reactions often ensue between samples and their surroundings; this includes reactions with the DAC’s pressure media, chamber gasket, and diamond anvils. A classic example includes the works of Santamaria-Perez and Chulia Jordan et al., who cautioned researchers about the use of refractory metal gaskets, e.g., rhenium and tungsten, in conjunction with CO<sub>2</sub> and carbonate samples, as they observed rapid gasket oxidation under high-temperature, high-pressure (HTHP) conditions [30,31]. So, although *unintended* chemical reactions do occur in LH-DAC work, this review distinguishes LRS-DAC studies as those (purposefully) inducing chemical reactions with useful/desired products.

Similarly, we exclude chemical reactions caused only by changes in pressure (i.e., *mechanochemistry*) [32,33]), where lasers do not interact with the sample nor influence the reaction directly. For example, during *Laser Dynamic Compression Diamond Anvil Cell (LDC-DAC)* experimentation, samples are compressed through the passage of laser-induced pressure- or shock-waves (see this review, Part II [34]); in this case, any chemical reactions present are induced by rapid changes in *pressure*—but not by any direct interaction of the laser beam(s) with the samples. Finally, Part III does not include any “beam-induced synthesis” using sources outside of the 225 nm (deep UV) to 300 μm (terahertz) transmission band of diamond anvils [27,35,36].

An LRS-DAC system (e.g., that in Figure 1), typically includes a minimum of one cw or pulsed laser system, a focused laser beam, a precursor or reactant [i], an optional pressure medium [vi], a desired product [ii], a byproduct [iv], a substrate [viii], a reaction zone [iii], one or more diamond anvils [vii], a chamber gasket [v], and characterisation tools (not shown). Although some alternate materials such as sapphire (Al<sub>2</sub>O<sub>3</sub>) or moissanite (SiC) have been substituted during some L-DAC experiments due to their lower cost and transparency in the deep ultraviolet [37–39], diamond is the most common anvil material in LRS-DAC systems [40].

An exceptional range of thermodynamic conditions is made available through LRS-DAC methods, allowing investigators to effectively break chemical bonds and induce reactions that otherwise could not occur [41–43]. It is well-known that the electronic structure and chemical bonding of atoms, molecules, and crystals can be modified greatly through the application of pressure [1,44,45], potentially reducing activation barriers to reaction [1]. For example: (1) Interatomic and intermolecular distances may be reduced, increasing the probability of favourably oriented orbitals forming bonds (or where significant realignment is necessary, reducing the probability of bond formation). (2) Interatomic and intermolecular bonds may also be shortened, which tends to enhance the covalent nature of these bonds. (3) Inner and normally unoccupied orbitals can also become available for bonding. (4) Sometimes, even interstitial orbitals in a lattice, not associated with any particular atom, can also form bonds. (5) In some configurations, bond angles can become distorted greatly, which may lead to dissociation or bond reconfiguration(s). (6) Longer bonds are generally weaker than shorter bonds, may be distorted the most, and are generally dissociated most readily; thus, as the pressure increases, shorter bonds tend to become favoured. (7) The chemical behaviour of elements tends toward those of higher-Z elements within the same group of the periodic table. (8). The number of ligands bound to central atoms or molecules tends to increase (i.e., coordination numbers increase). (9) The structure of molecules and crystals tends to adjust to more compact arrangements, e.g., polymeric chains or cubic- and hexagonally close-packed structures. (10) At extreme pressures (>100 TPa), it has even been theorised that (core) atomic orbitals well below the normal valence levels may become accessible for chemical bonding; this would open up an entirely new landscape of potential chemical compounds that could be synthesised [46]. However, what is less understood is how the combined effects of both pressure and laser stimuli direct the outcome of chemical reactions—and this represents a significant opportunity for further research.

The range of thermodynamic conditions available when both high pressures and laser stimuli are employed is impressive (even when considering only state variables like pressure and temperature). Moreover, when short-pulsed lasers and dynamic pressure DACs are introduced, materials can be processed to states far from equilibrium. This introduces the potential for many novel advanced materials (and metamaterials) to be created—and potentially recovered to ambient conditions.

As shown in Figure 2A, the number of published L-DAC studies has grown steadily for the last three decades, whilst LRS-DAC-related studies have increased by a factor of 6+ times—second only to LH-DAC-related work, this trend appears to be continuing and exponential. Most LRS-DAC research can be categorised according to several material classes, as plotted in Figure 2B. This includes low-Z carbon-containing compounds, and metal -hydrides, -borides, -carbides, -nitrides, and -oxides, as well as high-Z metallic compounds and intermetallics. The majority of articles have been focused on the binary metal nitrides (30%) or the binary metal oxides (22%).

Accordingly, this article describes the physics underlying LRS-DAC experiments, outlines the chronological development of LRS-DAC systems/methods, and summarises key reactive synthesis experiments. Lists of materials created to date via LRS-DAC systems are provided, together with the precursors, process conditions, and laser source wavelengths/powers. It is our hope that this article provides a useful guide to further forthcoming LRS-DAC studies.

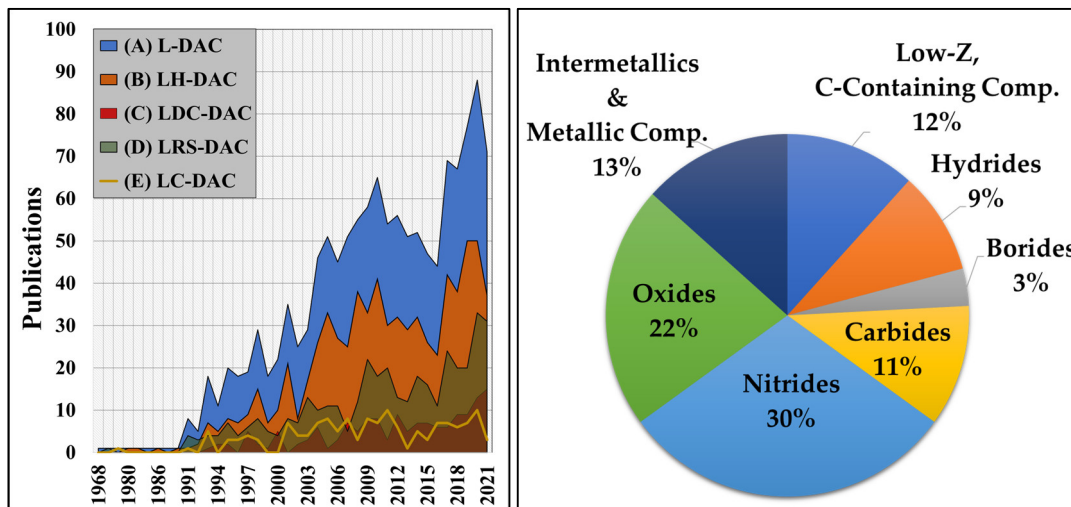


**Figure 2.** At left, (A) the total annual scientific production for laser- and synchrotron-based studies, (B) all L-DAC studies with (just) UV-IR lasers, (C) laser-heated diamond anvil cell (LH-DAC) research papers where primarily laser heating has been conducted for materials modification, (D) LRS-DAC articles where laser-induced chemical reactions/synthesis occurred, and (E) LC-DAC spectroscopic studies, [data for (A–E) obtained from the Web of Science database [26]. At right, the proportion of LRS-DAC-synthesised materials organised by the material categories: low-Z carbon-containing compounds, metal -hydrides, -borides, -carbides, -nitrides, -oxides, and high-Z metallic compounds and intermetallics.

## 2. Methodology

This L-DAC review was conducted using the primary academic research databases: Web of Science<sup>®</sup>, ScienceDirect<sup>®</sup>, ProQuest Science<sup>®</sup>, SCOPUS<sup>®</sup>, Wiley Online Library<sup>®</sup>, IEEE Xplore<sup>®</sup>, Access Engineering<sup>®</sup>, and Google Scholar<sup>®</sup>, as described in Parts I and II [26,34]; initial search outcomes for the keywords ‘diamond anvil cell,’ with no restrictions on publication year, yielded more than 8400 papers. Adding the keywords “laser”, with at least one of: “React\*”, “chemical reaction”, or “synthe\*”, yielded 407 articles. From these articles, 65 studies were manually identified where laser-induced chemical reactions at high pressures were obviously performed. An additional search using the keywords “high pressure” and “laser”, together with any of the following, “react\*”, “chemical reaction”, or “synthe\*”, or “stoichiomet\*”, were searched. This yielded 4429 journal articles. Replacing “laser” with the keywords, “laser-induced” OR “laser-assisted” OR “laser-heated” then down-selected this to only 963 results. Adding the keyword “anvil” then yielded only 388 results. Out of these, an additional 93 studies were manually verified where LRS-DAC studies were conducted. Finally, a third search looking for specific materials in conjunction with high-pressure laser processing was carried out, using the keywords “high pressure”, with the material class in question, e.g., “oxide”, plus any of the following, “react\*”, “chemical reaction”, or “synthe\*”, or “stoichiomet\*”, and with any of the set, “laser-induced”, “laser-assisted”, or “laser-heated”. No “anvil” or reference to the chamber hardware was included in this search. This provided 19 additional articles.

Further articles in all three cases were then found by searching forwards/backwards using key author (and related topical) information. A final tally of 186 LRS-DAC-related research articles was obtained.

The most cited of these articles focused on the synthesis of binary metal nitrides, rare-earth hydrides, and diamond. The 28 most cited articles published to date are listed in Figure 3, together with their authors and topics; each of these had a minimum of 100 citations.

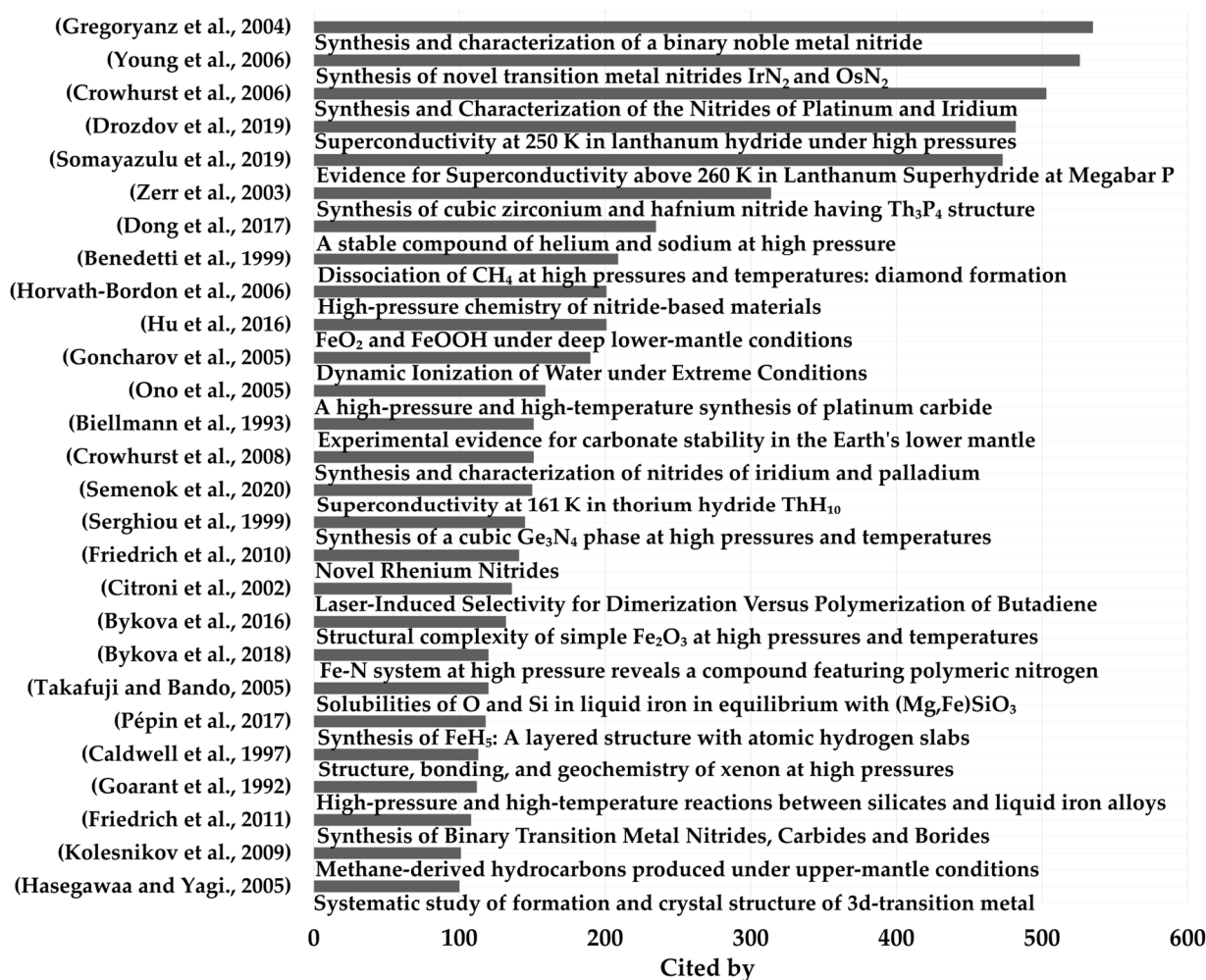


Figure 3. Most cited LRS-DAC works, with a minimum of 100 citations. Highly-cited topics included specific metal nitrides, metal hydrides related to superconductivity, and diamond synthesis [47–72].

### 3. Overview of Laser Reactive Chemical Synthesis in Diamond Anvil Cells (LRS-DAC) Experimentation

LRS-DAC reactions occur via two primary mechanisms: (M1) *decomposition reactions* of at least one precursor to produce one or more stable products (e.g.,  $A \rightarrow B + C$ ), and (M2) *oxidation-reduction (redox) reactions* between two or more chemical precursors, generating at least one stable product (e.g.,  $A + B + \dots \rightarrow C + \dots$ ). One notable subset of the latter reaction set (M2) are the so-called *combustion reactions*, in which a fuel and oxidizing agent are present.

LRS-DAC experimentation is distinctive because the laser spot is often directed onto a smaller subset of the chamber volume, allowing intense thermal and concentration gradients to be generated (e.g.,  $\gg 10^6$  K/m, in the case of temperature gradients) [73]. Such gradients tend to instigate diffusive- and/or convective-transport to/from the reaction zone, enabling fresh reactants to enter and byproducts to exit this zone (refer back to Figure 1).

Note that laser stimulus can be thermally activated (i.e., pyrolysis), or photoactivated (i.e., photoexcitation or photolysis), or it can be a combination of these. Photoexcitation allows researchers to drive electrons to higher energy levels and partially ionize precursor molecules, which may be used to enhance chemical reactivity. Intense, multiphoton laser excitation provides a route to control reaction pathways and thereby select for specific compounds/isomers, some of which may otherwise be inaccessible under ordinary conditions [74]. Photolysis, on the other hand, takes photostimulation to an even higher

level, directly breaking bonds; these are known as dissociation or decomposition reactions (e.g., the  $A \rightarrow B + C$  reactions, described above). All of these non-thermal mechanisms can significantly alter (and broaden) the thermodynamic landscape, as they may enable reactions at reduced temperatures or even eliminate sample heating entirely [1].

Both continuous wave (cw) lasers and pulsed lasers have been successfully employed to induce chemical reactions in LRS-DACs. Frequently, high-powered cw lasers are applied in pyrolytic reactions [75], whereas pulsed lasers are used in photoexcitation [76] and photolysis [77] applications. Most experiments thus far have been cw pyrolysis experiments.

The most common continuous wave laser sources included Nd:YAG (@ 1064 nm), Nd:YLF (@ 1053, 1060, or 1090 nm), YDFL (1.07  $\mu\text{m}$ ),  $\text{Ar}^+$  (351, 488, or 532 nm), and  $\text{CO}_2$  (10,600 nm) lasers [19,22,23,60,61,71,74–84]; many experiments employed constant high powers exceeding 25 W. The most frequently applied pulsed laser sources were the Q-switched Nd:YAG (@ 1064 nm) and  $\text{CO}_2$  (10,600 nm) lasers. Interestingly, no DUV sources below 350 nm, nor IR sources above 10,600 nm, were reported, although many such lasers and masers are commercially available. Likewise, no uses of short-pulsed lasers (with pulse widths shorter than 100 ps) have been reported, nor have uses of tunable light sources been reported, such as optical parametric amplifiers (OPAs). In fact, it would appear that experiments with laser pulses shorter than five nanoseconds have yet to be attempted. This suggests that a wide variety of potentially important LRS-DAC experiments have yet to be performed.

Indeed, the prospective thermodynamic landscape for LRS-DAC experiments is exceedingly large. Not only can pressures applied to the precursor be controlled dynamically, but static/dynamic temperatures can be set to any value ranging from below the background temperature to tens of thousands of degrees Kelvin; induced temperatures can be varied rapidly using femtosecond [85,86] to millisecond pulsed beams, and intense spatial temperature gradients are also usually present [29,87]. Independent of any laser heating, precursor molecules can be photoactivated with intense pulsed sources, preferably at energies approximating those of electron transitions or molecular vibrations/rotations. In the former case, ultraviolet and visible photons are suitable [88], while in the latter case, photon energies ranging from the near infrared through the far IR and into the mm-wave regime can be employed [89,90]. In all cases, tunable light sources, which can match the transitions and vibrational energies of the precursor(s), are desired.

In addition to photon energies, the fluence of the beam is critical in determining the rate at which energy is applied to the chemical precursor, whether or not the beam causes heating of the precursor. For a cw beam, the temperature rise,  $T$ , at a laser-heated sample is proportional to the average laser power delivered,  $P_o$ , and inversely proportional to the thermal conductivities of the various media/components,  $k_i$ , and the beam's  $1/e^2$  Gaussian spot size,  $\omega_0$ , as follows:

$$T \sim \frac{P_o}{k_i} \left( \frac{1}{\omega_0} \right)^2 \quad (1)$$

Thus, the temperature rise depends strongly on the laser spot size, and finely focusing the beam allows one to dramatically increase the peak temperature attained. Note that the spot size attainable with a Gaussian beam is directly proportional to the laser beam's wavelength, so using short laser wavelengths makes it possible to achieve small laser spots. For the reviewed articles,  $1/e^2$  spot sizes ranged from 1–100  $\mu\text{m}$ , with typical sizes of 30  $\mu\text{m}$ , and many of the lasers employed were in the near-infrared regime. Finally, where average power,  $P_o$ , is low, the *average* temperature rise of samples will not be great, even if the peak energy is large. These simple rules of thumb allow one to design LRS-DAC experiments to either: (1) heat samples effectively, or (2) stimulate samples without excessively heating them, decoupling sample temperatures from photoexcitation and other factors.

Accordingly, one can see that parametric inputs to any reaction within an LRS-DAC system include at least the following: (1) instantaneous applied (static) pressures,  $P$ ; (2) pressure profiles vs. time  $P(t)$ ; (3) laser pulse wavelength,  $\lambda$ ; (4) laser pulse width,  $\tau$ ; (5) laser spot size,  $\omega_0$ ; (6) number of pulses within a pulse train (or total illumination time,  $t$ );

(7) optical absorbance of the sample, thermofluid properties of the precursor(s) and/or pressure medium, such as (8) heat capacity, (9) thermal conductivity, (10) absolute viscosity, (11) dynamic viscosities; (12) number of reactants; (13) relative concentrations of reactants; and (14) thermal conductivity of the diamond anvils and chamber walls, etc. Consequently, an LRS-DAC process can be quite complex to model, irrespective of the chemistry involved, with many potential input parameters affecting reaction outcomes. Furthermore, there are many potential outcomes for a material's composition and microstructure. Thus, to successfully map the entire parameter space for the synthesis of even one set of binary or ternary compounds can indeed be time-consuming and challenging.

Nonetheless, more than 100 distinct binary/ternary compounds have been synthesised using the LRS-DAC method thus far, and many of these compounds have been newly discovered or unusual materials not ordinarily found in nature. Most of these materials were reported with at least some compositional and phase mapping versus the pressure, temperature, and fluence (P-T-F) conditions under which they were generated. For example, a novel material,  $\text{Ru}_2\text{C}$ , was identified, among other conditions, and one set of optimal conditions was identified as (8 GPa, 2000 K, 120 W) [14]. Another example was the mapping and the synthesis of molybdenum nitride,  $\gamma\text{-Mo}_2\text{N}$ , from molybdenum metal foil and liquid nitrogen at (7 GPa, ~2000 K, 100 W) [41].

#### 4. LRS-DACs: Physical Processes, Historical Development, and Key Experiments

Figure 4 provides a synopsis of the maximum pressure and temperatures attained during LRS-DAC experiments (green-shaded region), as compared to those used during LH-DAC experiments (orange-shaded box) and LDC-DAC experiments (red-shaded region). For comparison, estimated P-T conditions of various astrophysical and geophysical sources are also provided (cross-symbols), including Jupiter's moon Europa at a depth of 250 km and Jupiter's central core. Observe that LRS-DAC experiments have been conducted within a comparable range of conditions to LH-DAC investigations; this is to be expected, as many of the chemical reactions were pyrolytic in nature. Maximum pressures apparent in the LRS-DAC studies range from just 1 GPa to over 900 GPa, while maximum temperatures begin at room temperature and reach to >7300 K. Of course, these are the reported *maximum or peak* values in each study; many of these reactions were also investigated at more moderate P-T conditions. It is noteworthy that most LRS-DAC experiments reported maximum temperatures lower than 3000 K, whereas LH-DAC studies clustered somewhat at higher temperatures (as the research emphasis has been on high-temperature phase transitions). Interestingly, there is a dearth of (peak) reaction data between 300 K and 1000 K, with no data at temperatures below 293 K. This leaves many reactions at more moderate conditions less explored. Additionally, extreme conditions well above 7500 K (which would include plasmas) have not been studied in LRS-DAC systems. This is also an invitation for further investigation, as plasma enhancement is a useful tool for controlling chemical reaction pathways, as is often observed in high-pressure sintering [91,92] or plasma-jet processing [93–95].

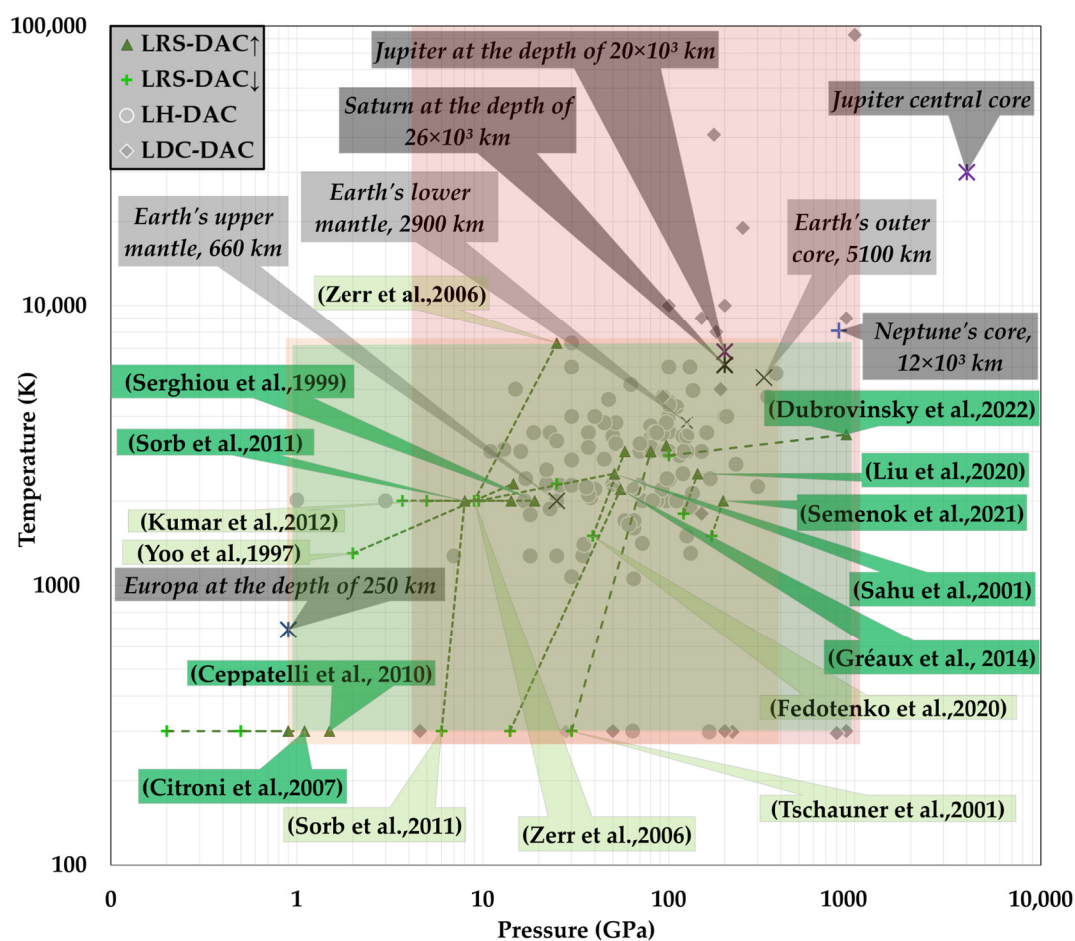


**Figure 4.** (A—Green) Peak P-T Map of LRS-DAC experiments [14,19,56,61,74,76–80,84,96–104], as contrasted with other L-DAC methods, such as: (B—Orange) LH-DAC experiments [28,29,73,105–220] and (C—Red) LDC-DAC experiments [46,221–227]. For reference, several P-T conditions are provided, including: 250 km down in Europa’s oceans [228]; 660, 2900, and 5100 km below the Earth’s surface [136,190,221];  $12 \times 10^3$  km deep within Neptune’s core [229];  $26 \times 10^3$  km deep inside Saturn’s liquid- hydrogen mantle [230]; and  $20 \times 10^3$  km deep in Jupiter’s upper atmosphere [231].

LRS-DAC systems can be implemented as single-sided configurations in which the incident beam is directed through one diamond anvil [18,75,77], such as illustrated in Figure 1, or as dual-sided configurations with two incident beams arriving on either side of the DAC [232]. Although the laser beam focal spot can encompass the entire clear aperture of the L-DAC, it is often much smaller to accommodate localised reactions. It is even possible to have multiple laser spots within the chamber, as depicted in Figure 1. The laser beam wavelength is selected to interact with the precursor (i), the pressure medium (vi), the substrate (such as the grid (viii) displayed in Figure 1), or the product (ii), depending on the type of reactions planned.

For localised pyrolytic reactions, the laser beam wavelength is typically selected to be absorbed by the precursor, the substrate, or the product, without being absorbed by the pressure medium or other materials in the chamber. Incident photons are converted into heat, which ultimately defines the reaction zone (iii). For localised photoexcitation or *photolysis*, laser wavelengths are chosen to cleave bonds within the precursor material [233,234], without exciting other media or substrates in the chamber. One potential exception to this is photocatalysis, in which a substrate or pressure medium may act as a catalyst for the reaction of the precursor(s) [235,236]. For photoexcitation or photolysis, pulsed laser sources are often employed to reduce the average power delivered to the sample [237], and tuneable

sources, e.g., optical parametric amplifiers (OPA), may be used to match the relevant bond energies [238].

Important elements of a complete *LRS-DAC system are shown in* Figure 5. This includes cw or pulsed laser sources (i), beam delivery optics designed to provide a well-focused laser spot (viii), transparent anvils (iv), a gasket chamber enclosing the experiment (v), diamond seats (vi), and a mechanism for driving the diamond anvils (vii). In addition, measurement and characterisation tools observing the reaction zone typically include (at a minimum): infrared pyrometers (x) to monitor the temperature profile in the reaction zone, a high-resolution spectrometer for pressure measurements (e.g., using Ruby fluorescence [239]) (xi), and microscopes for general observation and process control (xii) [27,240].

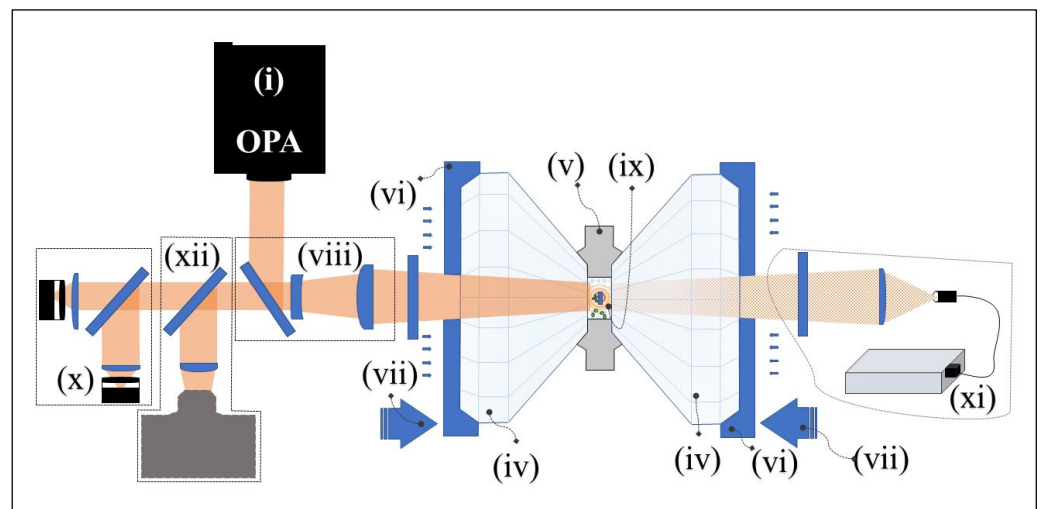


**Figure 5.** Typical arrangement of a Laser Reactive Synthesis Diamond Anvil Cell (LRS-DAC) for scientific or engineering experiments. The various components of this system are described in the text.

#### 4.1. Chemical Reactions

For a given set of precursors, the reaction rate for an LRS-DAC process is determined by the slowest (rate-limiting) step. At high pressures, all of the following can limit the reaction rate: (1) chemical thermodynamics, (2) chemical kinetics, and (3) mass transport of products, adsorbates, and byproducts. We will discuss each of these in more detail below.

##### 4.1.1. Chemical Thermodynamics

It is well-known that the application of pressure can alter the Gibbs Free Energy,  $G$ , and shift the equilibrium of a reaction [241–244]. In terms of the state variables—internal energy,  $U$ , enthalpy,  $H$ , entropy,  $S$ , temperature,  $T$ , molar volume,  $V$ , and pressure,  $P$ —the Gibbs free energy is defined by:

$$G \equiv U + PV - TS = H - TS \quad (2)$$

Assuming a constant temperature and taking the differential of Equation (2) gives:

$$dG \equiv dH - TdS \quad (3)$$

Then, by applying the definitions of enthalpy and internal energy, one further obtains the equation:

$$dG = +VdP - SdT \quad (4)$$

From Equation (4), one can see that the natural variables for Gibbs free energy are *pressure* and *temperature*, and that large changes in pressure can indeed influence the outcome of a chemical reaction. In fact, it has been shown that decomposition reactions

can be driven solely by pressure rises without any heating [1,245,246]. By again assuming isothermal conditions ( $dT \rightarrow 0$ ) in Equation (4), one obtains:

$$\left(\frac{dG}{dP}\right)_T = V \quad (5)$$

For highly incompressible materials, such as liquids and solids, the molar volume ( $V$ ) is relatively small compared to gases, so changes in the Gibbs free energy with pressure are often neglected under ordinary conditions (and over limited pressure ranges), and  $V$  is assumed to be constant. However, given the extended pressure ranges of diamond anvil cells, especially above 1 GPa,  $V$  becomes a significant function of pressure. To find the change in Gibbs free energy, Equation (5) must be integrated using an appropriate empirical function, e.g.,  $V(P, T)$  in:

$$\Delta G = \int_{P_0}^{P_f} V(P, T) dP \quad (6)$$

Depending on the sign of  $V(P, T)$ , the change in Gibbs free energy can be positive or negative, and where  $\Delta G$  becomes  $\leq 0$ , spontaneous reactions may occur [247]. For most materials, the sample volume decreases with pressure, and there are many examples in the literature where reactions have been enhanced through the application of pressure [248]. However, there are also examples of negative compression [249].

For the opposite extreme of a compressible ideal gas, the molar volume can be replaced using the ideal gas law, and Equation (6) becomes:

$$\Delta G = \int_{P_0}^{P_f} \frac{\mathcal{R}T}{P} dP = \mathcal{R}T \ln\left(\frac{P_f}{P_0}\right) \quad (7)$$

Of course, no gas behaves ideally when compressed to the pressures typical of a diamond anvil cell (including small atoms like helium), so caution should be used in applying Equation (7). This is because the ideal gas law assumes that a gas's molecular size and intermolecular attractive forces are negligible, which is no longer true at pressures where molecules are forced into close contact.

Thus far we have focused on pressure dependencies, but during LRS-DAC experiments both pressure and temperature are factors. When a laser heats a sample, the  $-SdT$  term in Equation (4) can significantly alter the Gibbs free energy; for many reactions, increased temperatures are needed to activate the reaction, even with the application of pressure [99,250–252]. This is one reason why extreme pressures are often seen in LRS-DAC studies.

#### 4.1.2. Chemical Kinetics:

For *kinetically limited (KL)* reactions in gases at low pressures, the reaction rate,  $r$ , follows the well-known Arrhenius rate equation, with associated activation energy,  $E_a$ , and preexponential factor,  $A$ , as follows:

$$r = A \cdot e^{-E_a/\mathcal{R}T} \quad (8)$$

Here,  $T$  is the temperature at the reaction zone, and  $\mathcal{R}$  is the universal gas constant. The differential form of this equation is:

$$\ln(r) = \ln(A) - \frac{E_a}{\mathcal{R}T} \quad (9)$$

Equation (9) is often used to curve-fit experimental data in an Arrhenius plot. Where pressure and other dependencies are anticipated, the preexponential factor,  $A$ , in Equation (8) is sometimes expanded as follows:

$$r = r_0 \cdot f(T) \cdot g(P) \cdot e^{-E_a/\mathcal{R}T} \tag{10}$$

Here,  $r_0$  is a constant,  $g(P)$  is a function describing the pressure dependency, and  $f(T)$  accommodates any temperature dependencies in the preexponential factor, and is often empirically derived or estimated from models [253,254].

For gas-phase reactions, one often-used form of Equation (10) defines  $g(P) \equiv P^n$ , where  $n$  is a simple exponential reaction order, i.e.,:

$$r = r_0 \cdot P^n \cdot e^{-E_a/\mathcal{R}T}, \tag{11}$$

Now, it is important to understand that Equations (8)–(11) are all based on collisional dynamics models of gases [241,255], which are not generally applicable to liquid- or solid-state reactions. Nevertheless, these equations have regularly been applied to high-pressure reactions, even when condensed phases have been present [253].

A more relevant rate equation based on *transition-state theory* that applies to liquid, solid, and mixed phases was developed by H. Eyring and M. Polanyi in 1935 [256–258]:

$$r = \frac{k_B T}{h} \cdot e^{-\Delta G^\ddagger/\mathcal{R}T} \tag{12}$$

Here,  $\Delta G^\ddagger$  is the change in the *Gibbs Free Energy of Activation*,  $k_B$  is Boltzmann’s constant, and  $h$  is Planck’s constant.  $\Delta G^\ddagger$  is the energy required to bring the reactants to an intermediate activated state. The logarithmic form of Equation (12) is:

$$\ln(r) = \ln\left(\frac{k_B T}{h}\right) - \Delta G^\ddagger/\mathcal{R}T \tag{13}$$

Now, similar to the derivation of Equation (5), the activation volume,  $\Delta V^\ddagger$ , is obtained by taking the derivative of Equation (13) with respect to pressure [259–261]:

$$\mathcal{R}T \frac{d\ln(r)}{dP} \ln(r) = -\Delta V^\ddagger \tag{14}$$

Via analogy with Gibb’s equation (Equation (3)),  $\Delta G^\ddagger$  depends on changes in *the enthalpy of activation*,  $\Delta H^\ddagger$ , and the *entropy of activation*,  $\Delta S^\ddagger$ :

$$\Delta G^\ddagger = \Delta H^\ddagger - T\Delta S^\ddagger \tag{15}$$

Substituting Equation (15) into Equation (12) affords Equation (16):

$$r = \left[ \frac{k_B T}{h} \cdot e^{+\Delta S^\ddagger/\mathcal{R}} \right] \cdot e^{-\Delta H^\ddagger/\mathcal{R}T} \tag{16}$$

Note that the term,  $e^{+\Delta S^\ddagger/\mathcal{R}}$ , induces positive changes in the reaction rate when the entropy of activation increases, which is consistent with the Second Law of Thermodynamics. While this term is (nominally) independent of temperature, it does depend on pressure and the activation volume. Note also that the expression in square brackets is analogous to the preexponential factor,  $A$ , in the Arrhenius relation Equation (8) above.

From Equations (14) and (16), one finally obtains:

$$r = \left[ \frac{k_B T}{h} \cdot e^{+\frac{P\Delta V^\ddagger}{\mathcal{R}}} \right] \cdot e^{-\Delta H^\ddagger/\mathcal{R}T} \tag{17}$$

Equation (17) is very useful for understanding the influence of high pressures on the reaction kinetics inside a diamond anvil cell. By analogy with Le Chatelier's principle [262,263], one would expect a reaction to proceed from precursor  $\rightarrow$  product, where an increase in pressure results in a decreased volume of the product, e.g., as through a reduced number of moles in the product and/or rearrangements into a more compact lattice. Similarly, the reaction should proceed where a decrease in pressure results in an increased volume of the product, e.g., an increased number of moles and/or rearrangements into a less compact lattice. Indeed, one can see that increases in applied pressure,  $P$ , result in an increasing reaction rate in Equation (17), provided  $\Delta V^\ddagger$  is of the correct sign. This is illustrated in Figure 6, where a dimensionless version of Equation (17) is plotted, with changes in pressure,  $P$ , and sign of  $\Delta V^\ddagger$  indicated. Although the reaction rate's pressure dependency is small at pressures near STP, it is much more significant in LRS-DACs where pressures may be  $\gg 0.1$  GPa [264].

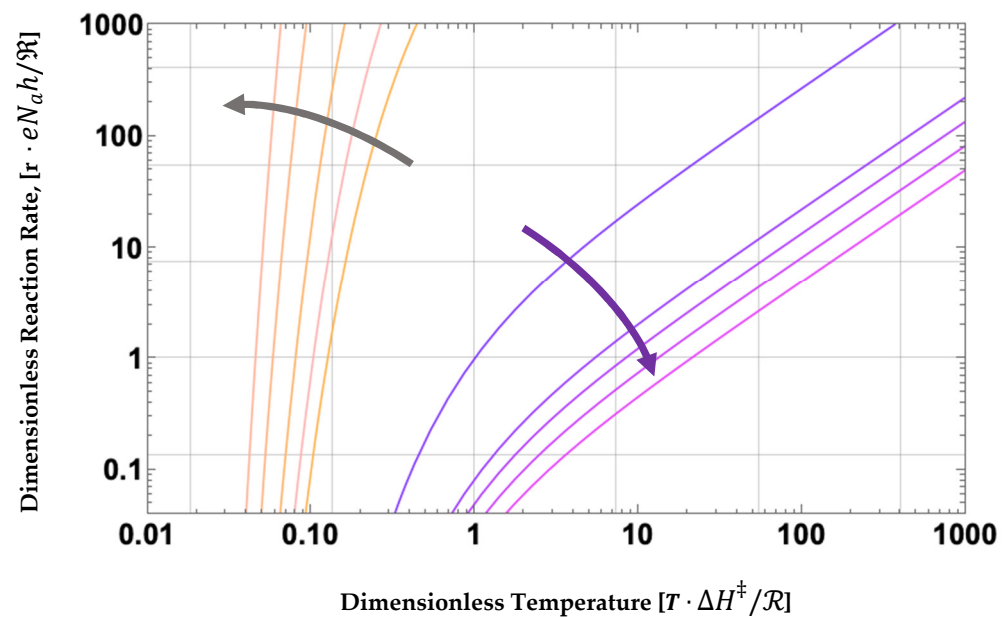


**Figure 6.** Log-Log parametric plot of reaction rates from Equation (17) vs. dimensionless temperature,  $T$ . The yellow-grey family of curves is for positive  $\Delta V^\ddagger \equiv 1$ , while the purple to red family of curves is for negative,  $\Delta V^\ddagger \equiv -1$ . Pressure is increasing in the directions shown by the arrows.

Thus, one significant difference in the kinetics of LRS-DAC processes is that the pressures applied by the DAC must be accounted for, in addition to the temperatures induced by the laser beam [254]. Furthermore, this pressure dependency is unlikely to fit well onto a simple reaction order model, e.g., Equation (11); rather, Equation (17) or a variation of Equation (12) should be used. Several possible variants have been proposed [265–267]. Unfortunately, reaction kinetic studies within diamond anvil cells are few, and where laser-induced processes are involved, there are even fewer [47]. This is definitely an opportunity for further research.

Finally, when materials are synthesised at high pressures, there is always the risk that they are not thermodynamically stable at ambient conditions and cannot be recovered upon release of compression [268–271]. It is well-known, for instance, that diamond is a metastable material—it is thermodynamically unstable at STP, but exists at ambient conditions due to the presence of a large activation barrier in its phase-transition kinetics, preventing its reversion to the more thermodynamically-stable graphite. Similarly, when compression is released following a chemical reaction, the nature of some newly formed bonds may change; some may revert to their earlier configurations, or where the kinetic barriers are sufficiently high, they may be recovered to ambient conditions. As chemical kinetics is time-dependent, rapid release of pressure and/or quenching can be attempted to recover (metastable) materials [272]. Of course, pulsed and modulated lasers may be used during LRS-DAC studies to quench materials at extremely high rates ( $\gg 10^6$  K/s).

Analysis of the pressure-dependence of both the chemical thermodynamics and kinetics aids in understanding whether a particular material may be recovered or not [273,274]. In many cases, although the chemical thermodynamics are relatively well-understood during LRS-DAC experiments, the reaction (and recovery) kinetics may not be known a priori, and tend to be less well-documented.

#### 4.1.3. Diffusive and Convective Mass Transport:

The rate of a decomposition or redox reaction will usually follow an exponential rise with temperature, e.g., in Equation (12), until  $T$  is sufficiently high that the precursor in the reaction zone cannot be resupplied at a faster rate; when this occurs, the reaction becomes limited instead by the transport rate of the precursor(s)/byproduct(s), whether this transport occurs through diffusion, convection, or advection. In this case, the process is considered to be *mass transport limited (MTL)*. This situation occurs quite often in diamond anvil cells, where the sample in the chamber may be a solid, semi-solid, or viscous fluid, and the reaction rate is sufficiently high to locally deplete the precursor(s) within the reaction zone. When this occurs, the reaction rate is governed by the generalised convection-diffusion equation (CDE), where  $D(x,t)$  is the diffusion constant,  $c(x,t)$  is the one-dimensional concentration vs. time,  $u(x,t)$  is the convection fluid velocity, and  $d(x,t)$  is a retardation factor [275]:

$$d(x,t) \cdot \frac{\partial c(x,t)}{\partial t} = \frac{\partial}{\partial x} \left[ D(x,t) \frac{\delta c(x,t)}{\delta x} - u(x,t) \cdot c(x,t) \right] \quad (18)$$

Here we provide only the one-dimensional form of the CDE for a single diffusing species. In reality, Equation (18) must be solved for  $c(x,t)$ , given multiple species and an LRS-DAC three-dimensional geometry with a set of known material properties and physical arrangements within the cell. With the exception of a few simple geometries, this is usually done numerically [276,277].

One useful simple geometry is that of a spherical *sink*, of radius  $a_0$ , within an infinite medium; this is similar to the geometry in which a laser induces a reaction at a reaction zone within a DAC that is much smaller than the gasket chamber. Smoluchowski et al. provided the steady-state rate at the sphere's surface,  $a_0$  [278]:

$$r(a_0, t \rightarrow \infty) = 4\pi a_0 D c_0 \quad (19)$$

Solutions have also been derived analytically for the case of multiple spherical sinks [279]; this situation is similar to the illustration of Figure 1, where multiple laser spots are focused inside the chamber. In the simplest case of two spherical sinks, both of radius,  $a_0$ , separated by a centre-to-centre distance,  $L$ , an approximate solution was developed by Calef and Deutch [280]:

$$c(a = a_0, t \rightarrow \infty) = 8\pi a_0 D c_\infty \left[ \frac{1}{1 + a_0/L} \right] \quad (20)$$

Equation (20) shows that the concentration profile is proportional to the diffusivity and background concentration,  $c_\infty$ . It also suggests that having more than one reaction zone occurring simultaneously within the gasket chamber slows down the diffusive-limited reaction rate of each zone slightly, depending on their separation distances,  $L$ . This can be seen in Figure 7 where the calculated diffusive reaction flux,  $r'$ , at each spherical reaction zone is provided, by dividing Equation (20) with the surface area of each sphere and normalising by  $8\pi D c_\infty$ . One can see that as the separation distance,  $L$ ,  $\rightarrow 1$  (close contact), the diffusive flux reaches a minimum that is typically half that of the  $L \rightarrow \infty$  asymptote. Interestingly, at sufficient distances,  $L \gg a_0$ , the reaction flux is almost unaffected by the presence of a second competing sink, which has implications for the parallel processing of materials within diamond anvil cells. This is also a potentially fruitful area that should be explored further.

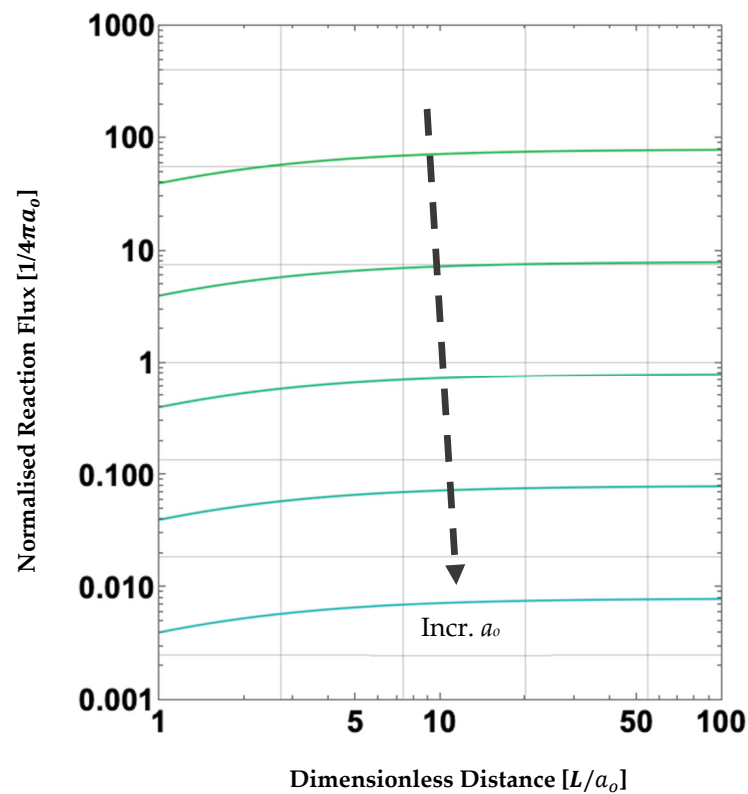


**Figure 7.** Log-Log parametric plot of diffusion-limited reaction fluxes for two reaction zones (diffusive sinks), which depend on the reaction zone radii,  $a_0$ , and the centre-to-centre distances between these zones,  $L$ . Note that the smaller the reaction zone, the more rapid the diffusion-limited reaction flux.

Finally, observe that in Figure 7, the smaller the reaction zone radii,  $a_0$ , the more rapid the diffusive reaction flux,  $r'$ , to both spherical sinks (direction of dotted arrow indicates increasing  $a_0$ ). Note that  $r'$  scales as  $1/a_0$ . This enhanced reaction-flux effect has been observed previously in other microchemical processes [281], e.g., hyperbaric-pressure laser chemical vapour deposition (HP-LCVD), in which rapid growth of fibres along the direction of the beam axis is made possible by minimising the size of the reaction zone [282].

The diffusion constant in liquids tends to decrease upon application of pressure as the viscosity of the fluid increases. This will, of course, dampen diffusion-limited reaction rates. When reactions involving solids are diffusion-limited, it is anticipated that such reactions will progress quite slowly compared to those in low-viscosity fluids, because solid-state diffusion constants are 6–10 orders of magnitude smaller than in the liquid state [283,284]. To minimise this drawback, researchers may take steps to: (1) thoroughly mix all solid precursors at the nano/microscale prior to processing [82], (2) use porosities in solids to provide transport “highways” across the solid [285], or (3) use strong thermal gradients to drive diffusive transport, including applying phenomena such as the thermodiffusion (or Soret) effect [185].

Now, up until this point, we have treated the diffusion constant,  $D$ , in Equation (18) as a constant.  $D(P)$  is weakly dependent on the pressure, so this dependency is frequently overlooked in the literature. However, within diamond anvil cells,  $D(P)$  can no longer be treated as negligible. Nachtrieb’s law describes the diffusion constant’s dependence on  $T$  and  $P$  in solids [286,287], as follows:

$$D(T, P) = D_0 e^{-[\beta \cdot T_m(P)/T]} \tag{21}$$

Here,  $D_0$  and  $\beta$  are empirically derived constants, and  $T_m(P)$  is an expression for the observed melting temperature versus pressure for the matrix material in question;

auspiciously,  $T_m(P)$  has been determined for a wide range of solid materials in DACs, allowing Equation (21) to become a practical model in this context.

Outside of determining diffusion constants [288], there is little data available on mass transport within diamond anvil cells, especially during LRS-DAC experiments. This is undoubtedly due to the confined spaces within gasket chambers and the difficulty in making in situ measurements. Consequently, few detailed models of the *mass transport limited behaviour of high-pressure reactions* have been developed in the literature [289]. However, due to the extreme pressures involved in LRS-DAC experiments, it is anticipated that many reactions are mass-transport limited, with solid-state or liquid-state diffusion being the rate-limiting step [1]. This is also an area ripe for future development.

#### 4.2. Diffusive and Convective Heat Transfer

As described in Part I for continuous wave (cw) LH-DAC experiments [26], the temperature rise at the reaction zone is dependent on the balance between the incident laser power and the rate of heat transfer to the surrounding precursor medium and DAC components. As illustrated in Figure 8, energy is delivered by the focused laser beam (purple arrow, [ii]), and heat conducts away through the diamond anvils and chamber gasket (black arrows, [xxvi]). Where temperatures are sufficiently high, thermal radiation from the reaction zone can be significant (orange arrows, [xxvii]). This radiation can be used to monitor the reaction temperature (see [x] in Figure 5). The same is true for the LRS-DAC configuration, but in this case, the laser-heated (reaction) zones are often intentionally smaller than those for LH-DAC experiments (where broad constant temperature profiles are desired). For LRS-DAC experiments, the reaction zone is often surrounded by a comparatively large pressure-medium region. Light can also be observed from the backside of the DAC and measured using a spectrometer (green arrows, [xxix]).

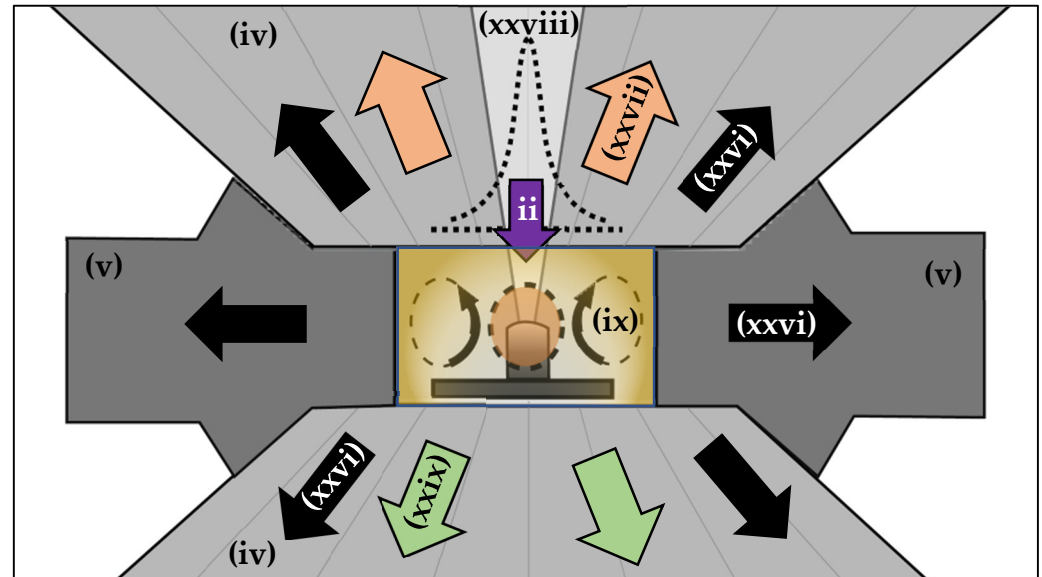


**Figure 8.** Schematic of heat and mass transport in an LRS-DAC. The laser is focused (ii) to selectively heat only a portion of the chamber, specifically a small reaction zone. Where the precursor medium is in a liquid state, (rapid) convection cells (ix) can form inside the gasket chamber. This transfers heat from the reaction zone to the surrounding diamond anvils (iv) and gasket (v), and moves the precursor to the reaction zone and byproducts from this zone.

Note that finely focused laser beams can induce extreme local thermal gradients, such as that illustrated in the temperature profile of Figure 8 (see super-Gaussian dotted graph [xxviii]), and such thermal gradients can drive solid-phase diffusion, allowing fresh reactants to transport into the reaction zone and byproducts to leave this zone. This is very important because diffusive exchange enables reversible chemical reactions to

proceed where they would otherwise stagnate at equilibrium [1]. When diffusive exchange occurs rapidly, it also enables mass-transport-limited reactions to proceed quickly, as fresh precursor is available [290].

Now, when liquid or semisolid precursors/pressure media are present, combined with sufficient laser fluence, it should not be assumed that convective heat and mass transfer are inherently negligible (as is sometimes presumed during LH-DAC or LDC-DAC experiments). Rather, given these conditions, convective cells can form within the pressure medium, allowing the precursor to circulate continuously past the reaction zone. Typically, the more rapid this circulation, the more rapid the reaction rate, as less time is required to exchange reactants/byproducts at the reaction zone. Recent simulations and measurements of convective flows inside L-DACs where melts are present suggest that fluid velocities approaching  $100 \mu\text{m/s}$  may occur within a gasket chamber, depending on fluid viscosities [291]. Such velocities are sufficient to sustain rapid reaction rates, until all available precursor is exhausted. Given sufficient laser irradiation and convective transport, single crystals and whiskers have even been “grown” in LRS-DACs [292], in a manner analogous to solution-liquid-solid (SLS), or supercritical fluid-liquid-solid (SFLS), whisker growth [293]. Of course, the potential for *convective circulation* depends on the precursors’ and pressure media’s thermophysical properties, the incident beam parameters, the overall timescale of irradiation, and the diamond anvil cell’s geometry.

Of course, the rate and manner in which the laser beam energy is applied matters greatly to the induced temperature rise in the reaction zone. Figures 9 and 10 provide an overview of the LRS-DAC laser pulse widths and exposure times that have been reported in the literature for pulsed and cw lasers, respectively. CW lasers and long-pulse lasers are often used for the constant heating of samples; on the contrary, short-pulsed lasers are typically used to drive reactions over short time periods while minimising any large-scale heating.

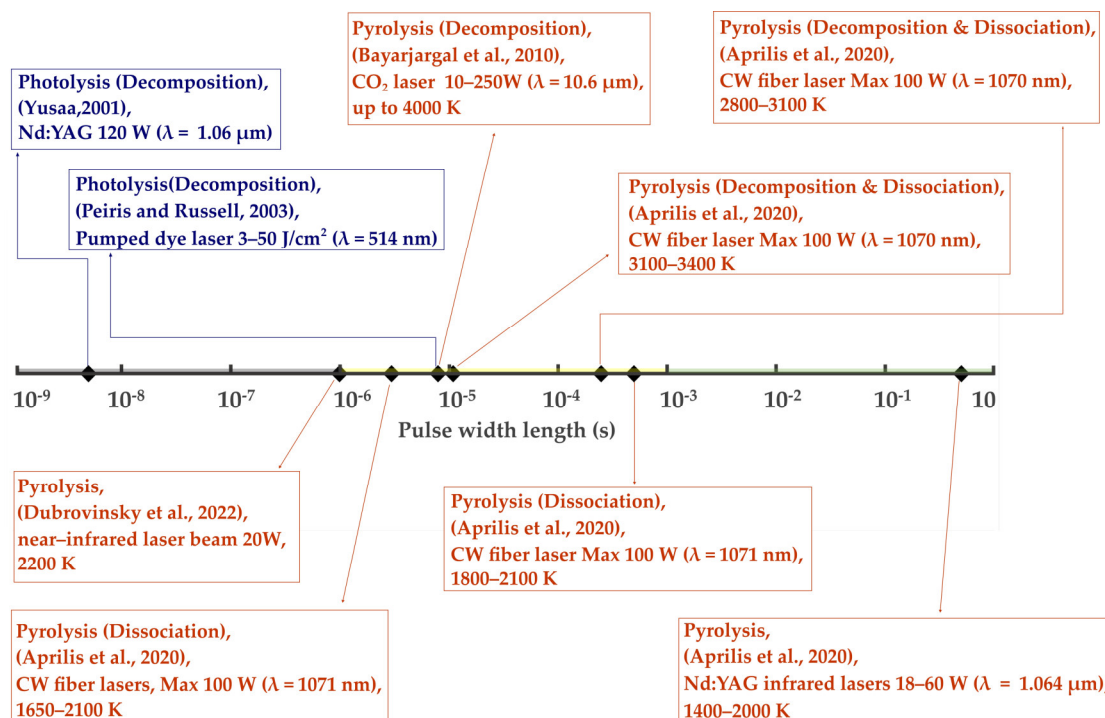


**Figure 9.** Classes of laser-induced reactions obtained (pyrolysis, photoexcitation, photolysis, etc.) vs. laser beam pulse widths employed, including Q-switched, electrooptically pulsed, and chopped beams [60,77,82–84,237].

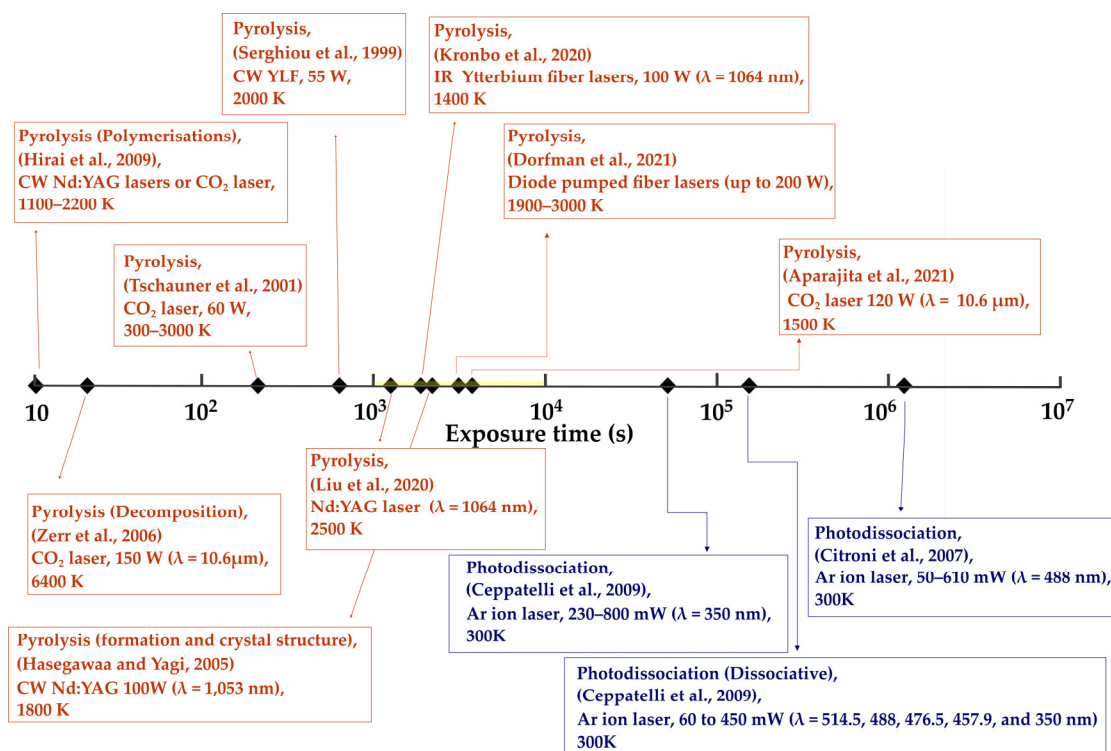


**Figure 10.** Classes of laser-induced reactions obtained (pyrolysis, photoexcitation, photolysis, etc.) vs. laser illumination time for continuous-wave lasers, including laser wavelengths, from the ultraviolet (350 nm) to the infrared (10.6 μm) [19,22,23,61,71,74–76,78–81].

In Figure 9, one can see a range of LRS-DAC laser pulse widths being employed, from nanoseconds to long pulses approaching 1 s. Yusaa et al., who in 2001 conducted photolytic decomposition experiments on silver iodide, used the shortest-pulse laser to date, with 5 ns pulse widths [237]. Similarly, Peiris and Russell used a dye laser in 2003 to carry out photolysis experiments on sodium azide (NaN<sub>3</sub>), with 7–8 μs pulses [77]. These are the two *pulsed* photolysis LRS-DAC experiments of which we are aware. The pulse energy in Yusaa's and Peiris/Russell's experiments were 120 W and 3–50 J/cm<sup>2</sup>, respectively, which are near the ablation threshold.

Meanwhile, pulsed LRS-DAC pyrolysis experiments included: (1) Aprilis et al. (2020) at 11, 250, and 500 microsecond pulse widths; (2) Bayarjargal et al. (2010) at 8 microsecond pulse widths; and (3) Semenok et al., with long pulses of 300–500 ms [60,82,83], approaching that of cw lasers. In all these cases, the intent was to heat and pyrolyze chemical precursors at temperatures ranging from 1400 to over 4000 K. As a result, most of these lasers had high average powers, capable of 100 W or more.

Interestingly, there is an absence of LRS-DAC processing at laser pulse widths shorter than 5 ns, despite many short-pulsed lasers (<100 ps) now being widely available. This is certainly an area ripe for further exploration, i.e., the combination of high pressures with ultrashort time duration processing could lead to the syntheses of many novel materials, including those with glassy and nanocrystalline structures [294,295].

Figure 10 gives an overview of selected LRS-DAC experiments with laser exposure durations longer than 1 s. For these durations, it is presumed that the lasers were being used in cw mode, and where any modulation was employed, it was through the use of chopped beams or shutters. As anticipated, most of these LRS-DAC experiments involved pyrolysis of precursors at high average power lasers, combined with relatively long time durations of hundreds to thousands of seconds. These included the works of Zerr et al. (2006), Hirai et al. (2009), Tschauner et al. (2001), Serghiou et al. (1999), Liu et al. (2020), Hasegawa & Yagi (2005), Kronbo et al. (2020), Aparijita et al. (2021), and Dorfman et al.

(2021) [19,22,23,61,71,75,79–81]. Induced temperatures ranged from 300 K to 6400 K, with the average maximum temperature being ~2000 K. These are extremely high temperatures, in many cases relevant to chemical reactions in planetary and geophysical studies, rather than for high-temperature high-pressure (HTHP) chemical synthesis of novel materials.

Now, while elevated temperatures may often be required for reaction kinetics to proceed, long-duration heating may also lead to large-scale grain growth and Ostwald ripening. This can be seen in the formation of diamond from CaCO<sub>3</sub> samples produced by Bayarjargal et al. of Figure 9 [83]. Grain growth may be desirable where large single crystals are the intended product, but such is often not the case. The rate of grain growth,  $r_{xtl}$ , often follows an Arrhenius-like relationship, similar to Equation (8), of the form:

$$r_{xtl} = r_{xtl,0} \cdot e^{-E_b/RT}, \quad (22)$$

but here,  $E_b$  is the activation energy of boundary mobility and  $r_{xtl,0}$  is an empirically derived rate constant for grain growth. As one can see from Equation (22), the grain growth rises exponentially with temperature, so extreme temperatures are likely to produce large crystalline structures.

On the right side of Figure 10, one can also see three important photolysis experiments by Cintroni et al., which were performed using the ultraviolet/visible lines of a cw Ar+ laser. The exposure times in this case were on the order of 10<sup>4</sup>–10<sup>6</sup> s, as they were conducting experiments on the polymerisation of isoprene [74].

#### 4.3. LRS-DAC: Historical Development & Key Experiments

To our knowledge, the first LRS-DAC-related chemical synthesis was the disproportionation of olivine [(Fe,Mg)<sub>2</sub>SiO<sub>4</sub>] to stishovite [(Fe,Mg)O + SiO<sub>2</sub>] by L. Ming and A. Bassett in 1973 [157]. However, purposeful LRS-DAC research (intentionally inducing reactions) began in earnest during the 1990s. In 1991, Shekar et al. synthesised a novel binary intermetallic, indium antimonide (InSb), from elemental In and Sb [251]. The authors indicated that an exothermic reaction occurred when the cubic phase (and other “high-pressure” phases) of InSb were generated for the first time. Since this successful reaction, interest in LRS-DAC syntheses has been growing steadily. In 1992, Goarant, Guyot, Peyronneau, and Poirier of the Institut de Physique du Globe de Paris mixed iron, iron sulphide, and various metal silicates (e.g., forsterite, enstatite, and olivine), pressurising them to 130 GPa; the mixture was subsequently laser-heated until it melted, and the iron and other metallic phases were partially oxidised [296]. The authors observed significant temperature gradients within the gasket chamber during this process. These three initial events are displayed on the left side of the timeline in Figure 11.

In 1997, Yoo et al., from Lawrence Livermore National Laboratory (LLNL) and the University of California Los Angeles, explored the kinetics of boron nitride synthesis from elemental boron and nitrogen at high pressures [96]. This is the fourth event shown in Figure 11. No pressure-induced reactions were observed at room temperature, but with laser heating, hexagonal wurtzite and cubic boron nitride were synthesised at temperatures above 1300 K. They concluded that the activation energy for BN synthesis must be quite large, despite a highly exothermal reaction. This work encouraged others to explore the synthesis of boron–nitrogen compounds via L-DAC methods.

In 1999, another useful LRS-DAC experiment was conducted by Serghiou et al. of the Max Planck Institute in Germany, where a novel cubic spinel phase of germanium nitride (Ge<sub>3</sub>N<sub>4</sub>) was produced from elemental germanium and molecular nitrogen (See 5th event in Figure 11). They heated the Ge-N mix to over 2000 K with a YLF laser at various pressures between 3.7–20 GPa. This work opened the door for additional researchers to explore novel nitride-based compounds/structures for new semiconductor and ceramics materials.

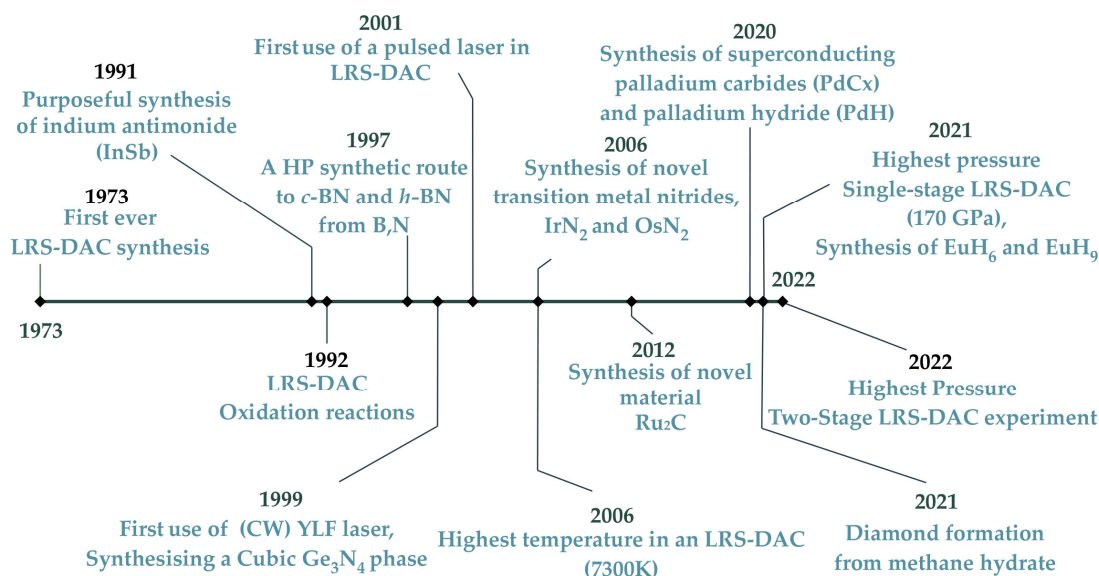


**Figure 11.** Chronology of key LRS-DAC developmental events, from 1973 to 2022.

The first utilisation of a pulsed laser, rather than cw lasers, was in 2001 by H. Yusa of the Japanese National Institute for Research in Inorganic Materials [237]. Importantly, Yusa stimulated a photochemical reaction (via photolysis) to decompose silver halides as a source of high-pressure halides for reactions in future experiments (see event location in the middle of Figure 11). A pulsed KrF excimer laser at ultraviolet wavelengths (248 nm) was used at a peak pulse energy of 5 mJ and pulse repetition rates (PRR) of 10 Hz. This work was also the first example of laser photolysis being conducted in an LRS-DAC experiment. Importantly, Yusa et al. suggested that tuning the laser excitation wavelength to chemical-specific absorption bands, e.g., using an optical parametric amplifier (OPA), could be used to target specific chemical bonds and realise selective photolytic reactions.

In 2006, A. F. Young, together with an international team of researchers from the USA, Italy, France, and the UK, demonstrated the growth of new metal nitrides, including iridium nitride, IrN<sub>2</sub>, and osmium nitride, OsN<sub>2</sub> (see middle of Figure 11) [53]. These binary compounds proved to be superhard, highly incompressible materials, with IrN<sub>2</sub> having a measured bulk modulus of 428 GPa—just under that of diamond at 455 GPa. This LRS-DAC effort demonstrated that new transition metal compounds can yet be discovered with the aid of laser-induced reactions at high pressure, and inspired others to search for new superhard materials via this approach.

The highest laser-induced temperature in an LRS-DAC experiment to date was attempted by Zerr, Gerghiou, Boehler, and Ross in 2006, with temperatures of up to 7300 K (see event in middle of Figure 11) [79]. They studied the decomposition of straight-chain alkanes into diamond and hydrogen, with alkane chain lengths up to nonane. The decomposition of methane initiated at applied pressures >13 GPa and temperatures over 2500 K. This is a significantly higher decomposition temperature than is normally observed at atmospheric pressures (typically >900–1000 K) [297]. Remarkably, the greatest diamond yield was obtained from the longer-chain alkanes. During the experiments, strong thermal gradients were observed laterally from the centre of the laser focus. Gradients were also observed axially (along the laser beam axis); the authors suggested that this was (plausibly) caused by insufficient insulation between the samples and the diamond anvils.

In 2012, Kumar et al. of the Gandhi Centre for Atomic Research, demonstrated the synthesis of a novel intermetallic of ruthenium and carbon, Ru<sub>2</sub>C, using an LRS-DAC (see the middle of Figure 11) [14]. Pure ruthenium and graphite were mixed, and pressure was applied to 5 GPa. The sample was then laser-heated to approximately 2000 K using a CO<sub>2</sub> laser with a 40 μm focal spot size. The bulk modulus for the resulting Ru<sub>2</sub>C sample was 178 GPa—a new highly incompressible material (compare to diamond's bulk modulus

at  $\sim 455$  GPa). This work demonstrated that novel advanced materials could actually be realised via the LRS-DAC technique, even at relatively “low” pressures of 5 GPa.

Recent LRS-DAC advances in 2020 have seen the chemical syntheses of palladium carbide and palladium hydride compounds, which under certain P-T conditions exhibit superconductivity [99]. Fedotenko et al. placed palladium foils inside an LRS-DAC with neon as a pressure medium. They then reacted the foils with carbon from the system’s diamond anvils to produce palladium carbide at pressures and temperatures of 50 GPa and 2500+ K, respectively. Likewise, palladium hydride was derived from the reaction of palladium foils with paraffin oil at 39 GPa and 1500 K. In this case, the paraffin also acted as the pressure medium. This work was important because it encouraged further high-pressure research into the synthesis and testing of metal hydride superconductors.

In 2021, Ma et al., an international team from China and Japan, synthesised europium hydrides,  $\text{EuH}_6$  and  $\text{EuH}_9$ , using an LRS-DAC, which exhibited clathrate superhydride structures [6]. Such superhydride structures are known to contribute toward high-temperature superconductivity in other metal hydrides, including lanthanum hydride,  $\text{LaH}_{10}$ , which has a very-high critical temperature of  $\approx 250$  K (nearly room temperature) [50,51]. Ma et al. reacted europium with ammonia borane ( $\text{BH}_3\text{NH}_3$ ) at pressures between 80–170 GPa and heated them with a 1050 nm laser beam. The ammonia borane served as a source of hydrogen.  $\text{EuH}_6$  formed at 152 GPa and 1700 K, while  $\text{EuH}_9$  was generated at 170 GPa and 2800 K. This study used the greatest hydrostatic pressure of any single-stage LRS-DAC experiment to date, at 170 GPa (see event on right hand side of Figure 11). This work also contributed to growing interest in the synthesis of high-temperature superconductors using the LRS-DAC technique.

Next to last on the timeline of Figure 11 (in 2021) is the decomposition of methane hydrate [ $(\text{CH}_4)_8(\text{H}_2\text{O})_{46}$ ] within an LRS-DAC system to produce diamond [252]. At high pressures/temperatures, Kadobayashi et al. demonstrated that methane hydrate dissociates into methane and water, and that the methane subsequently polymerises and dehydrogenates to rapidly form diamond. They also observed rapid convection within the DAC at temperatures above 1200 K. The C-O-H system produced diamond at less extreme pressures and temperatures (13–45 GPa, 1600 K) than had been observed previously using only hydrocarbon precursors and hydrogen. This article contributed because it provided a useful synthetic route to diamond, and because it demonstrated that diamond likely forms within the mantles of icy planets, like Uranus and Neptune, so that it “rains” diamond within the icy planets’ interiors.

Finally, at the end of the Figure 11 timeline, the work of L. Dubrovinsky et al. (in 2022) is notable for achieving the highest pressures to date in an LRS-DAC experiment (900 GPa) using a toroidal, two-stage DAC [84]. In this study, a metastable binary intermetallic of rhenium nitride,  $\text{Re}_7\text{N}_3$ , was synthesised from a few rhenium (Re) metal powder grains and nitrogen at temperatures of 2200 K and 2900 K, inside a focused-ion-beam machined Re gasket chamber only 6  $\mu\text{m}$  across. This metastable compound was only stable under highly compressed conditions.

## 5. LRS-DAC Synthesis: Summary of Important Material Classes

To date, over 100 separate binary/ternary compounds have been produced using LRS-DAC systems. For the reader’s reference, a summary is provided in Figure 12 of all the product materials synthesised successfully using LRS-DAC methods thus far, together with their peak reported processing pressures (blue curves) and temperatures (orange bars); further details of processing conditions are provided in the following sections. LRS-DAC materials are grouped into the following material classes (roughly according to their position on the periodic table):

- Low-Z Carbon-Containing Compounds/Materials.
- Binary Metal Hydrides.
- Binary Metal Borides.
- Binary Metal Carbides.
- Binary Metal Nitrides.

- Binary Metal Oxides.
- High-Z Intermetallics and Metallic Compounds.

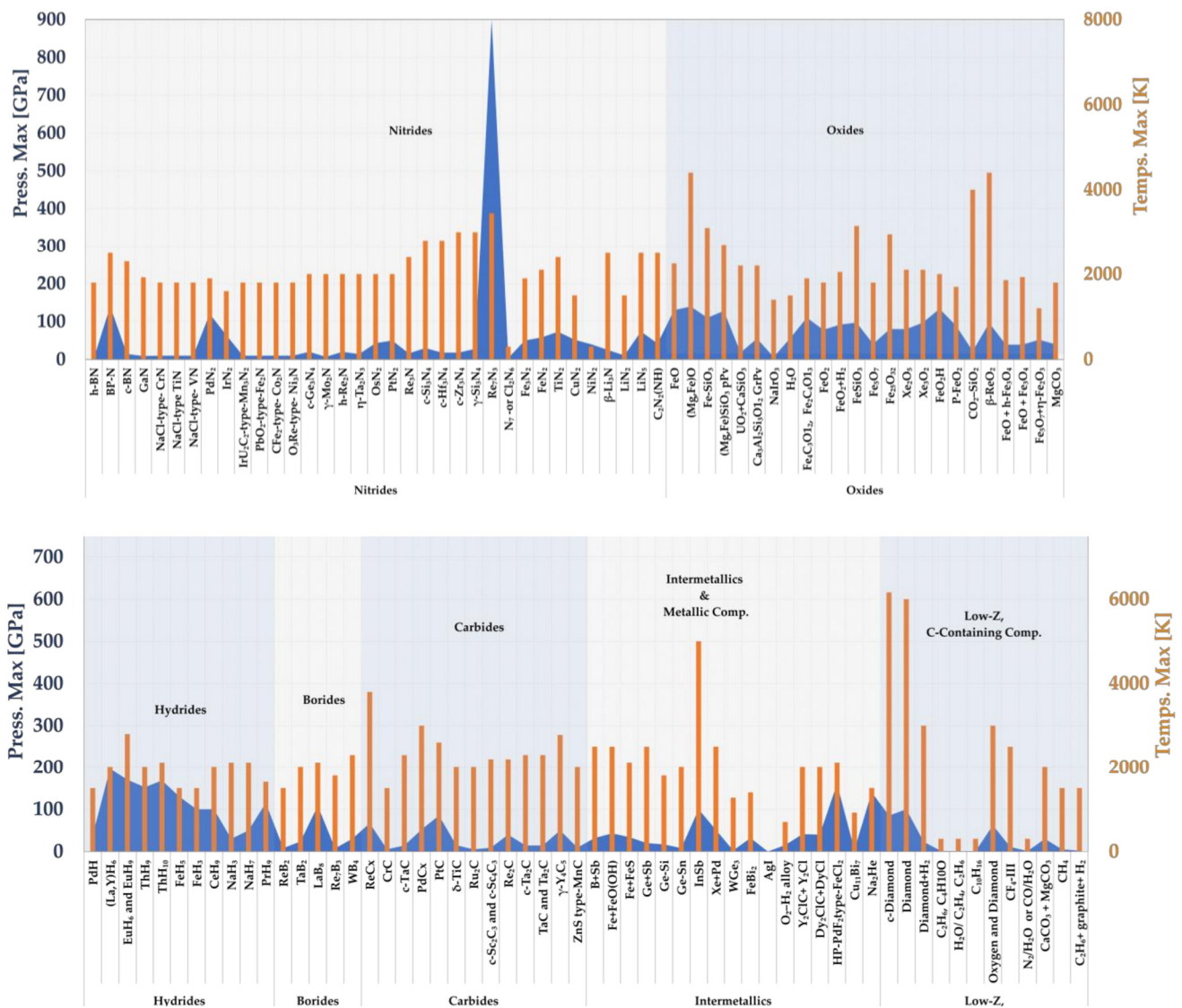


**Figure 12.** Peak P-T Conditions Realised During LRS-DAC Synthesis of Low-Z, Carbon-Containing Compounds.

### 5.1. Low-Z Carbon-Containing Compounds/Materials

The low-Z carbon containing compounds/materials primarily includes the synthesis of diamond, with additional products of methane, various alkanes, alkenes, and hydrocarbons. Note in Figure 12 the extreme processing temperatures involved in these reactions, many of which were over 2000 K, while applied pressures were under 50 GPa. Several impactful articles were published in 2021–2022 on diamond synthesis in this materials class. A group of Japanese researchers, including authors at Rissho University and Ehime University, demonstrated low-pressure polymerisation of methane and subsequent dehydrogenation into diamond using the C-O-H system [252]; this occurred at more moderate temperatures and pressures ( $P = 13\text{--}45$  GPa,  $T \approx 1600$  K) than are typically observed in the C-H system. This work demonstrated a novel lower-energy route to diamond. In addition, the same group decomposed polyethylene  $(C_2H_4)_n$  into diamond nanoparticles and hydrocarbon byproducts at pressures of 13–45 GPa and temperatures between 1600–3800 K. These pressures were significantly lower than related gas-gun dynamic compression experiments with the same precursors, and produced more diamond. This suggests that the timescale of

the process is very important for the decomposition of polymers into diamond, which is an important insight into the process kinetics.

Similar results were obtained by a group comprising authors from the University of California, Berkeley, Lawrence Livermore National Laboratory (LLNL), the University of Missouri (UM), the University of Tsukuba, Tokyo University, and the National Institute of Advanced Industrial Science and Technology in Japan. They were able to verify that methane polymerised and dissociated to diamond at pressures as low as 10–20 GPa, which contradicts current theories that predict polymerisation above 100 GPa. This provided new insights into the process kinetics. Finally, two additional groups explored novel pathways to diamond, including the decomposition of calcium carbonate, CaCO<sub>3</sub>, and carbon dioxide, CO<sub>2</sub>. For further processing details of the low-Z carbon-containing compounds, see Table 1.

**Table 1.** Low-Z, Carbon-Containing Compounds: Low-Z Carbon-Containing Materials Synthesised During Selected LRS-DAC Studies.

Product Material(s)	Precursor(s)	Press. [GPa]	Laser Type [nm or μm]	Laser Parameters: Pulse Length/Exposure Time [s], Powers/Energies [W/J], Spots [μm], or Induced Temps. [K]	Refs.
c-Diamond	a: methane hydrate b: (C <sub>2</sub> H <sub>4</sub> ) <sub>n</sub>	a: 13–45 b: 11–29	a: CO <sub>2</sub> [10.6 μm] b: CO <sub>2</sub> [10.6 μm]	a: [200 W], 50 μm b: [80 W], 2500–4000 K	a: [252] b: [9]
Diamond	a: CH <sub>4</sub> b: CH <sub>4</sub>	a: 10 to 50 b: 16.8	a: Nd: YAG [1062 nm] b: Nd: YAG or CO <sub>2</sub>	a: CW, 2000 to 3000 K b: CW, >3000 K	a: [48] b: [75]
Diamond	CaCO <sub>3</sub>	9–21	CO <sub>2</sub> [10.6 μm]	PW: 8 μs, [10–250 W], 40 μm, 3500 K	[83]
Diamond	CO <sub>2</sub>	30–80	CO <sub>2</sub> [10.6 μm]	100–200 s, [60 W], <30 μm, 300–3000 K	[80]
CaCO <sub>3</sub> + MgCO <sub>3</sub>	(CaMg(CO <sub>3</sub> ) <sub>2</sub> )	20–30	Nd: YAG [1062 nm]	30 μm, 2000 K	[58]
C <sub>8</sub> H <sub>12</sub>	C <sub>4</sub> H <sub>6</sub>	0.6–0.8	Ar [458/488 nm]	10–20 mW	[63]
C <sub>3</sub> H <sub>8</sub> + H <sub>2</sub>	C <sub>2</sub> H <sub>6</sub>	5	Nd: YLF	20–25 μm, 1500 K	[70]
CH <sub>4</sub>	C <sub>2</sub> H <sub>6</sub> , H <sub>2</sub>	5	Nd: YLF	20–25 μm, 1500 K	[70]
C <sub>2</sub> H <sub>6</sub> + C + H <sub>2</sub>	CH <sub>4</sub>	2	Nd: YLF	20–25 μm, 1000–1500 K	[70]

### 5.2. Binary Metal Hydrides

This class of compounds is important for many technologies, including (1) high-temperature superconductivity, (2) catalysis where hydrogen is present, and (3) hydrogen separation membranes. One can see in Figure 12 that the pressures and temperatures applied with the class of materials thus far have not exceeded 200 GPa and 3000 K.

The emphasis for many metal-hydride LRS-DAC studies was on creating compounds with the highest possible critical temperature for superconductivity, while applying the lowest possible pressures. Research in metal hydrides as superconductors was originally inspired by the 1968 theoretical work of Ashcroft et al., who proposed hydrogen becoming metallic (and superconducting) at pressures above 500 GPa [298]. Ashcroft et al. later theorised that hydrogen-rich compounds and alloys could reduce the external compression needed to achieve superconductivity [299,300]. Recently, this theoretical work has been extended to hydrogen chains and networks [301].

Some of the metal hydrides investigated thus far include: palladium hydride [99], PdH; the lanthanum-yttrium hydrides, (La,Y) H<sub>6</sub> and (La,Y) H<sub>10</sub> [101]; the europium hydrides, EuH<sub>6</sub> and EuH<sub>9</sub> [6]; and thorium hydride, ThH<sub>10</sub> [60]. Perhaps the most noteworthy of

these studies was the synthesis of lanthanum-yttrium hydrides, (La,Y) H<sub>6</sub> and (La,Y) H<sub>10</sub>, in which a critical temperature of 253 K was measured for the latter compound. Importantly, the critical current density for (La,Y) H<sub>10</sub> may actually be greater than that of yttrium barium copper oxide (YBCO), which was the first superconductor discovered possessing a critical temperature greater than liquid nitrogen's boiling point of 77 K (which is technologically enabling). The lanthanum-yttrium hydride study (and related metal hydride works) are exciting because they may ultimately lead to practical room-temperature superconductors. For additional processing specifics concerning the binary metal hydrides, refer to Table 2.

**Table 2.** Binary Metal Hydrides: Metal Hydrides Synthesised During Selected LRS-DAC Studies.

Product Material(s)	Precursor(s)	Press. [GPa]	Laser Type [nm or μm]	Laser Parameters: Pulse Length/Exposure Time [s], Powers/Energies [W/J], Spots [μm], or Induced Temps. [K]	Refs.
a: (La,Y)H <sub>6</sub> b: (La,Y) H <sub>10</sub>	La, Y, NH <sub>3</sub> BH <sub>3</sub>	170–196	Data N/A	PW: 100–400 ms, <2000 K	[101]
EuH <sub>6</sub> and EuH <sub>9</sub>	Eu, NH <sub>3</sub> BH <sub>3</sub>	152 & 170	YDFL [1050 nm]	1700 & 2800 K	[6]
PdH	Pd, Paraffin oil	39	Nd: YAG [1.06 μm]	≈1500 K	[99]
FeH <sub>3</sub>	Fe, H <sub>2</sub>	100–125	Nd: YAG [1.06 μm]	<1500 K	[67]
FeH <sub>5</sub>	Fe, H <sub>2</sub>	130–140	Nd: YAG [1.06 μm]	<1500 K	[67]
CeH <sub>9</sub>	Ce, H <sub>2</sub>	80–100	Nd: YAG [1.06 μm]	PW: 1 μs, 10 μm, ~2000 K	[302]
NaH <sub>3</sub>	NaH, H <sub>2</sub>	≥30	Data N/A	>2000 K	[303]
NaH <sub>7</sub>	NaH, H <sub>2</sub>	40–50	Data N/A	>2000 K	[303]
PrH <sub>9</sub>	Pr, NH <sub>3</sub> BH <sub>3</sub>	115–130	Nd: YAG [1.06 μm]	1650 K	[304]

### 5.3. Binary Metal Borides

Binary metal borides are an important class of high-hardness, high-temperature, oxidation-resistant materials that in some cases exhibit superconductivity (e.g., MgB<sub>2</sub>). LRS-DAC studies focused on the synthesis of refractory or rare-earth compounds, including: tantalum boride, TaB<sub>2</sub> [305]; rhenium boride, Re<sub>2</sub>B [69]; and the lanthanum borides, LaB<sub>5</sub> and LaB<sub>8</sub> [18].

Juarez-Arellano et al. verified that Re<sub>2</sub>B was the most stable high-pressure phase of rhenium boride and measured its compressive moduli [17]. Intriguingly, it is a superhard material with a bulk modulus of ~405 GPa; this value is akin to that of tungsten carbide. However, the bulk modulus is anisotropic—along one crystal plane, [001], Re<sub>2</sub>B is estimated to have a linear compressibility of 500 GPa. This finding, along with modelling analogous phases of Os<sub>2</sub>B, provided a noteworthy contribution in the search for materials harder than diamond.

Among all the metal borides, the lanthanum borides were processed under the most extreme conditions of 108 GPa and ~2100 K (See Figure 12). LaB<sub>8</sub> was found to have a clathrate structure and to be a tuneable superconductor, through the substitution of alkaline earth metals into its lattice. This has important implications for potential microelectronic devices, as well as the pursuit of room-temperature superconductors. For further processing details about the binary metal borides, see Table 3.

**Table 3.** Binary Metal Borides: Metal Borides Synthesised During Selected LRS-DAC Studies.

Product Material(s)	Precursor(s)	Press. [GPa]	Laser Type [nm or $\mu\text{m}$ ]	Laser Parameters:		Refs.
				Pulse Length/Exposure Time [s], Powers/Energies [W/J], Spots [ $\mu\text{m}$ ], or Induced Temps. [K]		
<b>LaB<sub>8</sub></b>	2B + LaB <sub>6</sub>	108	Nd: YAG [1.06 $\mu\text{m}$ ]	PW, $\approx$ 2100 K		[18]
<b>TaB<sub>2</sub></b>	Ta, B	14–23.7	Nd: YLF	[10–15 W], 1600–2000 K		[305]
<b>ReB<sub>2</sub></b>	Re, B	8	Data N/A	1500 K		[69]
<b>Re<sub>7</sub>B<sub>3</sub></b>	Re, B	8.9–22.1	Data N/A	120–360 s, [8–25 W], 30 $\mu\text{m}$ , 1500–4000 K		[306]
<b>WB<sub>4</sub></b>	W, B	30.3	Data N/A	10 $\mu\text{m}$ , 2300 K		[307]

#### 5.4. Binary Metal Carbides

Many of the binary metal carbides exhibit high stiffnesses/hardnesses, extreme melting points, and high thermal conductivities; these materials are commonly used as coatings in industrial processes where cutting, grinding, or boring are needed. Metal carbides have thus far been studied using LRS-DAC systems at relatively moderate pressures <100 Gpa, but at temperatures of up to 3000 K (See Figure 12). Some of the carbides investigated thus far include (sorted into groups):

- Transition Metal Carbides: The scandium carbides (Sc<sub>2</sub>C<sub>5</sub> and Sc<sub>4</sub>C<sub>3</sub>), titanium carbide (TiC), chromium carbide (CrC),
- Refractory Metal Carbides: The titanium carbides (TaC and Ta<sub>2</sub>C), and rhenium carbides (ReC<sub>x</sub> and Re<sub>2</sub>C).
- Platinum Group Metal Carbides: Palladium carbide (PdC<sub>x</sub>), ruthenium carbide (Ru<sub>2</sub>C), and platinum carbide (PtC).

One highly cited article on the metal carbides was that of Ono et al. in 2005 [57]. They reacted platinum powder with high-purity carbon at 85 GPa and 2600 K to obtain a new high-pressure phase, PtC, in a rock-salt-like structure. By discovering a new carbide phase, the work inspired researchers to investigate other HPHT carbides.

One interesting later study was that of a large international group, Juarez-Arellano et al., studying the synthesis of scandium carbide [308]. Scandium is a less common transition metal, and, in its elemental form, is highly reactive. For this work, scandium carbide was synthesised from scandium flakes and graphite at pressures of 10 GPa and temperatures of 1600–2200 K, and it was found to have the stoichiometry Sc<sub>4</sub>C<sub>3</sub>. This article contributed by suggesting that there are a wide variety of compounds and minerals yet to be investigated via the LRS-DAC approach, and they studied a less conventional material. For additional processing details of the binary metal carbides, refer to Table 4.

**Table 4.** Binary Metal Carbides: Metal Carbides Synthesised During Selected LRS-DAC Studies.

Product Material(s)	Precursor(s)	Press. [GPa]	Laser Type [nm or $\mu\text{m}$ ]	Laser Parameters:		Refs.
				Pulse Length/Exposure Time [s], Powers/Energies [W/J], Spots [ $\mu\text{m}$ ], or Induced Temps. [K]		
<b>Ru<sub>2</sub>C</b>	Ru, C	5	CO <sub>2</sub> [10.6 $\mu\text{m}$ ]	CW, [120 W], $\approx$ 40 $\mu\text{m}$ , 2000 K		[14]
<b>PdC<sub>x</sub></b>	Pd and C	52	Nd: YAG [1.06 $\mu\text{m}$ ]	$\approx$ 2500 to 3000 K		[99]
<b>c-Sc<sub>2</sub>C<sub>3</sub> and c-Sc<sub>4</sub>C<sub>3</sub></b>	Sc <sub>0.87(6)</sub> O <sub>0.13(6)</sub>	9	Nd: YLF [1090 nm]	CW, 10–15 W, $\approx$ 25 $\mu\text{m}$ $\approx$ 1600–2200 K		[308]

Table 4. Cont.

Product Material(s)	Precursor(s)	Press. [GPa]	Laser Type [nm or $\mu\text{m}$ ]	Laser Parameters: Pulse Length/Exposure Time [s], Powers/Energies [W/J], Spots [ $\mu\text{m}$ ], or Induced Temps. [K]	Refs.
$\delta\text{-TiC}$	Ti, graphite	15	Nd: YLF [1090 nm]	CW, [ $<20$ W], 1600–2000 K	[309]
c-TaC	Ta, graphite	8.6–14.3	Data N/A	$\leq 2300$ K	[69]
c-Ta <sub>2</sub> C	Ta, graphite	8.6–14.3	Data N/A	$\leq 2300$ K	[69]
a: ReC <sub>x</sub> b: Re <sub>2</sub> C	Re, graphite	a: 67 b: 20–40	a: Nd: YAG b: Nd: YLF	a: [80 W], 3800 K b: CW, [10–15 W], 15–30 $\mu\text{m}$ , 1000–2200 K	a: [310] b: [17]
PtC	Pt,C	85	Nd: YLF, Nd: YAG	$\approx 2600$ K	[57]
CrC	Cr, C, RCH <sub>2</sub> OH	5–5.3	CO <sub>2</sub> [10.6 $\mu\text{m}$ ]	50 min, [120 W], $\sim 30$ $\mu\text{m}$ , 1500 K	[19]
ZnS type-MnC	Mn, C	4.7–9.2	CO <sub>2</sub> [10.6 $\mu\text{m}$ ]	[120 W], 30 $\mu\text{m}$ , 2000 K	[7]

### 5.5. Binary Metal Nitrides

Metal nitrides are important technological materials, known for their hardnesses, wear resistances, high melting points, and optoelectronic properties. By far the most LRS-DAC studies have been carried out on the binary metal nitrides. This includes synthesis of the following compounds, within the groups shown:

- Metalloid-based Nitrides: Boron nitride (BN), silicon nitride (Si<sub>3</sub>N<sub>4</sub>), and germanium nitride (Ge<sub>3</sub>N<sub>4</sub>). (See Table 5).
- Transition Metal Nitrides: Manganese nitride (Mn<sub>3</sub>N<sub>2</sub>), iron nitride (Fe<sub>2</sub>N), cobalt nitride (Co<sub>2</sub>N), nickel nitride (Ni<sub>3</sub>N), and gallium nitride (GaN). (See Table 6).
- Refractory Metal Nitrides: Titanium nitride (TiN), vanadium nitride (VN), chromium nitride (CrN), zirconium nitride (Zr<sub>3</sub>N<sub>4</sub>), molybdenum nitride (Mo<sub>2</sub>N), hafnium nitride (Hf<sub>3</sub>N<sub>4</sub>), tantalum nitride (Ta<sub>2</sub>N<sub>3</sub>), and the rhenium nitrides (Re<sub>2</sub>N and Re<sub>3</sub>N). (See Table 7).
- Platinum Group Metal Nitrides: Palladium nitride (PdN<sub>2</sub>), osmium nitride (OsN<sub>2</sub>), iridium nitride (IrN<sub>2</sub>), and platinum nitride (PtN<sub>2</sub>). (See Table 8).

Table 5. Binary Metalloid-Based Nitrides: Metalloid Nitrides Synthesised During Selected LRS-DAC Studies.

Product Material(s)	Precursor(s)	Press. [GPa]	Laser Type [nm or $\mu\text{m}$ ]	Laser Parameters: Pulse Length/Exposure Time [s], Powers/Energies [W/J], Spots [ $\mu\text{m}$ ], or Induced Temps. [K]	Refs.
a. c-BN b. h-BN	B, N	a. 14.6 b. 2	Nd: YAG [1.06 $\mu\text{m}$ ]	a. $\approx 30$ W, 2300 K b. $\approx 30$ W, $\approx 1800$ K	[96]
c-Si <sub>3</sub> N <sub>4</sub>	a: Si, N b: $\beta\text{-Si}_3\text{N}_4$	a: 15 b: 30	a: Nd: YLF [527 nm] b: CO <sub>2</sub> [10.6 $\mu\text{m}$ ]	a: CW: 1–10 min, [14.5 W], 2200 K b: [ $\leq 120$ W], $\approx 2800$ K	[200]
BP-N	pure N and TiN/Pb + N <sub>2</sub> precursors	130–140	Nd: YAG [1.06 $\mu\text{m}$ ]	$\approx 15$ $\mu\text{m}$ , 2500 K	[22]
c-Ge <sub>3</sub> N <sub>4</sub>	Ge, N	14–20	Nd: YLF [1.053 $\mu\text{m}$ ]	55 W, 2000 K	[61]
Fe <sub>3</sub> N <sub>2</sub> + FeN	Fe, N <sub>2</sub>	49.6	[1.07 $\mu\text{m}$ ]	1900 K	[65]

Table 5. Cont.

Product Material(s)	Precursor(s)	Press. [GPa]	Laser Type [nm or $\mu\text{m}$ ]	Laser Parameters: Pulse Length/Exposure Time [s], Powers/Energies [W/J], Spots [ $\mu\text{m}$ ], or Induced Temps. [K]	Refs.
FeN <sub>2</sub> + FeN	Fe, N <sub>2</sub>	58.5–69.6	[1.07 $\mu\text{m}$ ]	2100–2200 K	[65]
FeN <sub>4</sub>	FeN <sub>2</sub> , FeN, N <sub>2</sub>	106–135	[1.07 $\mu\text{m}$ ]	>2000 K	[65]
TiN <sub>2</sub>	TiN, N <sub>2</sub>	73	YLF [1.06 $\mu\text{m}$ ]	2400 K	[311]
CoN <sub>2</sub>	Co, N <sub>2</sub>	39.9	IR laser	Data N/A	[312]
CuN <sub>2</sub>	Cu, N <sub>2</sub>	>50	Nd: YAG [1.064 $\mu\text{m}$ ]	>1500	[313]
NiN <sub>2</sub>	Ni, N <sub>2</sub>	~40	IR [1.09 $\mu\text{m}$ ]	300 K	[314]
C <sub>3</sub> N <sub>4</sub>	C <sub>2</sub> (CN) <sub>4</sub>	40	YLF [1.054 $\mu\text{m}$ ]	Data N/A	[315]
C <sub>2</sub> N <sub>2</sub> (NH)	C <sub>2</sub> N <sub>4</sub> H <sub>4</sub>	27–42	YLF [1.054 $\mu\text{m}$ ]	~1950–2500 K	[316]
$\beta$ -Li <sub>3</sub> N	Li, N <sub>2</sub>	3.5, 25.2	YLF	~1500, ~2500 K	[317]
LiN <sub>2</sub>	Li, N <sub>2</sub>	10.5–73.6	YLF	~1500–2500 K	[317]
LiN <sub>5</sub>	Li, N <sub>2</sub>	73.6	YLF	~2500 K	[317]

Table 6. Binary Transition Metal Nitrides: Transition Metal Nitrides Synthesised During Selected LRS-DAC Studies.

Product Material(s)	Precursor(s)	Press. [GPa]	Laser Type [nm or $\mu\text{m}$ ]	Laser Parameters: Pulse Length/Exposure Time [s], Powers/Energies [W/J], Spots [ $\mu\text{m}$ ], or Induced Temps. [K]	Refs.
GaN	Ga, LN <sub>2</sub>	9	YDFL [1.07 $\mu\text{m}$ ]	CW: 90 min, [17 W], 1925 K	[318]
NaCl-type-TiN	Ti, N <sub>2</sub>	≈10	Nd: YAG	CW: 30 min, [100 W], ≈1800 K	[71]
IrU <sub>2</sub> C <sub>2</sub> -type-Mn <sub>3</sub> N <sub>2</sub>	Mn, N <sub>2</sub>	≈10	Nd: YAG	CW: 30 min, [100 W], ≈1800 K	[71]
PbO <sub>2</sub> -type-Fe <sub>2</sub> N	Fe, N <sub>2</sub>	≈10	Nd: YAG	CW: 30 min, [100 W], ≈1800 K	[71]
CFe <sub>2</sub> -type-Co <sub>2</sub> N	Co, N <sub>2</sub>	≈10	Nd: YAG	CW: 30 min, [100 W], ≈1800 K	[71]
NaCl-type-VN	V, N <sub>2</sub>	≈10	Nd: YAG	CW: 30 min, [100 W], ≈1800 K	[71]
NaCl-type-CrN	Cr, N <sub>2</sub>	≈10	Nd: YAG	CW: 30 min, [100 W], ≈1800 K	[71]
O <sub>3</sub> Re-type-Ni <sub>3</sub> N	Ni, N <sub>2</sub>	≈10	Nd: YAG	CW: 30 min, [100 W], ≈1800 K	[71]

Table 7. Binary Refractory Metal Nitrides: Refractory Metal Nitrides Synthesised During Selected LRS-DAC Studies.

Product Material(s)	Precursor(s)	Press. [GPa]	Laser Type [nm or $\mu\text{m}$ ]	Laser Parameters: Pulse Length/Exposure time [s], Powers/Energies [W/J], Spots [ $\mu\text{m}$ ], or Induced Temps. [K]	Refs.
$\gamma$ -Mo <sub>2</sub> N	Mo, N	7	YDFL [1.07 $\mu\text{m}$ ]	600s, [30 W], 2000 K	[41]
c-Hf <sub>3</sub> N <sub>4</sub>	Hf, MN, N <sub>2</sub>	18	Nd: YAG [1053 nm]	CW: 2–20 min, [55 W], 2800 K	[49]
c-Zr <sub>3</sub> N <sub>4</sub>	Zr, N <sub>2</sub>	15.6–18	Nd: YAG [1053 nm]	CW: 2–20 min [55 W], 2500–3000 K	[49]
a: Re <sub>3</sub> N b:h-Re <sub>2</sub> N	Re, N <sub>2</sub>	a: 13–16 b: 20	Nd: YLF [1090 nm]	[100 W], ≈25 $\mu\text{m}$ , a: 1600–2400 K b: 2000 K	[62]
$\eta$ -Ta <sub>2</sub> N <sub>3</sub>	Ta, N <sub>2</sub>	11–14.1	Yb fiber	[8–9 W], 1600–2000 K	[319]

**Table 8.** Platinum-Group Metal Nitrides: Platinum-Group Metal Nitrides Synthesised During Selected LRS-DAC Studies.

Product Material(s)	Precursor(s)	Press. [GPa]	Laser Type [nm or $\mu\text{m}$ ]	Laser Parameters: Pulse Length/Exposure Time [s], Powers/Energies [W/J], Spots [ $\mu\text{m}$ ], or Induced Temps. [K]	Refs.
OsN <sub>2</sub>	Os, N <sub>2</sub>	43	N/A	>2000 K	[53]
IrN <sub>2</sub>	Ir, N <sub>2</sub>	47–64	N/A	1600 K	[52,53]
PtN <sub>2</sub>	Pt, N <sub>2</sub>	45–50	N/A	2000 K	[52,54]
PdN <sub>2</sub>	Pd, N <sub>2</sub>	a: 60 b: >58	a: Nd: YAG [1053 nm] b: Nd: YAG [1064 nm]	a: CW, [55 W], >1000 K b: CW, 1 $\mu\text{m}$ , 800–900 K	a: [59] b: [320]

One of the more technologically significant metal nitride articles was the first synthesis of a novel silicon nitride phase in 1999, which exhibited a cubic spinel-type structure, and was metastable at room pressures and <700 K [200]. This phase was likely a superhard material with a hardness similar to those of stishovite and c-boron nitride. The Si<sub>3</sub>N<sub>4</sub> was synthesised from elemental silicon and nitrogen at 30 GPa and 2800 K. Soon after this work, Zerr et al. synthesised the first zirconium and hafnium nitrides with a M<sub>3</sub>N<sub>4</sub> stoichiometry [49]. These studies were significant because they stimulated others to explore the synthesis of superhard materials and novel metal nitrides through the LRS-DAC technique.

The most cited LRS-DAC article on the metal nitrides, by Gregoryanz et al., described the first synthesis of a *noble metal* nitride, platinum nitride, (PtN) [54]. They combined elemental platinum and nitrogen in the diamond anvil cell and obtained PtN at pressures between 45–50 GPa and temperatures of ~2000 K. Similar results were obtained by Crowhurst et al. at ~50 GPa and ~2000 K [52]. These experiments were influential in that they demonstrated that novel metal nitrides could be realised within an LRS-DAC system—even when a chemical reaction would not ordinarily occur.

Another notable article was the LRS-DAC synthesis of polymeric nitrogen, with the structure of black phosphorus [22]. Liu et al. heated TiN and Pb powders with nitrogen at 130–132 GPa and 2200–2500 K to polymerise the nitrogen. This form of nitrogen is a very high energy-density material, as there is a considerable difference in energy between single bonds in a nitrogen polymeric chain and that of triple bonds in diatomic nitrogen. This difference can be used as the basis for novel, potentially environmentally friendly, fuels. For further processing particulars of the binary metal nitrides, see Tables 5 and 6, and the highly cited early high-pressure review of metal nitrides by Horvath-Bordon et al. [47].

### 5.6. Binary Metal Oxides

Metal oxides are often used as protective coatings in high-temperature applications (as they are already oxidised), or as dielectric materials, e.g., for optoelectronics applications. Referring to Figure 12, metal oxides have been processed under more severe conditions than most other materials—up to 130 GPa and 3400 K. There have been many metal-oxide LRS-DAC studies, focused primarily on iron oxide, silicates, and related compounds important in geophysical studies of the interior of terrestrial planets (Table 9). For example, two of these works examined reactions between common minerals, e.g., reacting FeS + Mg<sub>2</sub>SiO<sub>4</sub> to form iron oxide [296], or reacting iron oxide (FeO) with silica (SiO<sub>2</sub>) to form Fe-SiO<sub>3</sub> [321].

One of the most cited of these works is that of Hu et al., who demonstrated that goethite (FeOOH) decomposed to FeO<sub>2</sub> and H<sub>2</sub> at pressures of 76 GPa and 1800 K, allowing for hydrogen to be separated from oxygen in the lower mantle. This mechanism may have contributed to the current high-oxygen concentration in Earth's atmosphere [55]. Related studies include the dissociation of Fe<sub>2</sub>O<sub>3</sub> to Fe<sub>5</sub>O<sub>7</sub> + O<sub>2</sub> [56], and the reaction of water with Fe<sub>2</sub>O<sub>3</sub> to form FeO<sub>2</sub>H [298].

**Table 9.** Binary Metal Oxides: Metal Oxides Synthesised During Selected LRS-DAC Studies.

Product Material(s)	Precursor(s)	Press. [GPa]	Laser Type [nm or $\mu\text{m}$ ]	Laser Parameters: Pulse Length/Exposure Time [s], Powers/Energies [W/J], Spots [ $\mu\text{m}$ ], or Induced Temps. [K]	Refs.
FeO	FeS + Mg <sub>2</sub> SiO <sub>4</sub>	70, 75 and 130	Nd: YAG [1.06 $\mu\text{m}$ ]	[60 W], $\approx$ 2250 K	[296]
FeO <sub>2</sub>	$\alpha$ -Fe <sub>2</sub> O <sub>3</sub> + O <sub>2</sub>	76–78	Nd: YAG [1.06 $\mu\text{m}$ ]	1800 K	[55]
FeO <sub>2</sub>	FeOOH	92	Nd: YAG [1.06 $\mu\text{m}$ ]	2050 K	[55]
Fe <sub>5</sub> O <sub>7</sub>	$\alpha$ -Fe <sub>2</sub> O <sub>3</sub> + Fe <sub>2</sub> O <sub>3</sub>	40.7	[1.07 $\mu\text{m}$ ]	4 to 30 $\mu\text{m}$ , 1800 K	[64]
Fe <sub>5</sub> O <sub>7</sub> + O <sub>2</sub>	$\eta$ -Fe <sub>2</sub> O <sub>3</sub>	71	[1.07 $\mu\text{m}$ ]	4 to 30 $\mu\text{m}$ , $\sim$ 2700–3000 K	[64]
Fe <sub>25</sub> O <sub>32</sub>	Fe <sub>3</sub> O <sub>4</sub>	80.1	[1.07 $\mu\text{m}$ ]	4 to 30 $\mu\text{m}$ , 2950 K	[64]
FeO + Fe <sub>3</sub> O <sub>4</sub>	Fe <sub>5</sub> O <sub>6</sub>	38–59	Yb fiber	100 W, 30 $\mu\text{m}$ , 1930–2350 K	[322]
FeO + <i>h</i> -Fe <sub>3</sub> O <sub>4</sub>	Fe <sub>4</sub> O <sub>5</sub>	39	Yb fiber	100 W, 30 $\mu\text{m}$ , 1860 K	[322]
$\epsilon$ -Fe, Fe <sub>n</sub> O	Fe, Fe <sub>2</sub> O <sub>3</sub>	220–260	Data N/A	1 s, 20–30 $\mu\text{m}$ 3000–3500 K	[323]
Fe-SiO <sub>3</sub>	FeO and SiO <sub>2</sub>	45, 110	Nd: YAG [1.06 $\mu\text{m}$ ]	2200 $\sim$ 3100 K	[321]
FeSiO <sub>3</sub>	(Mg,Fe)SiO <sub>3</sub> + Fe	25–97	Nd: YLF	$\sim$ 50 $\mu\text{m}$ , 2300–3150 K	[66]
Xe <sub>2</sub> O <sub>5</sub>	Xe, O <sub>2</sub>	$\sim$ 77–83	Data N/A	>2000 K	[324]
Xe <sub>3</sub> O <sub>2</sub>	Xe, O <sub>2</sub>	$\sim$ 97	Data N/A	>2000 K	[324]
FeO <sub>2</sub> H	Fe <sub>2</sub> O <sub>3</sub> , H <sub>2</sub> O	133.5	Nd: YAG	2000 K	[325]
Fe <sub>5</sub> O <sub>7</sub> + $\eta$ -Fe <sub>2</sub> O <sub>3</sub>	FeOOH	52	Data N/A	1200 K	[326]
<i>P</i> -FeO <sub>2</sub>	$\alpha$ -FeO <sub>2</sub> H	72–132	Nd: YAG	1700–2000 K	[325]
CO <sub>2</sub> -SiO <sub>2</sub>	SiO <sub>2</sub> , CO <sub>2</sub>	16–22	CO <sub>2</sub> [10.6 $\mu\text{m}$ ]	30 s, 150 W, 30–40 $\mu\text{m}$ , >4000 K	[327]
$\beta$ -ReO <sub>2</sub>	CO <sub>2</sub> , SiO <sub>2</sub> , Re	8–48	[1.07 $\mu\text{m}$ ]	30 $\mu\text{m}$ , 1500–2400 K	[30,328]
MgCO <sub>3</sub>	MgO, CO <sub>2</sub>	5–40	Nd: YLF [1.05 $\mu\text{m}$ ]	1400–1800 K	[329]

### 5.7. High-Z Intermetallics and Metallic Compounds

Unlike metallic alloys, where metallic bonding dominates, intermetallic compounds show at least some evidence of chemical bonding with specific structures and occur in distinct elemental ratios, which can be stoichiometric or nonstoichiometric [330]. They are included in this review, as there are frequently chemical reactions associated with their formation. Intermetallics are known for their high melting points, high hardnesses, and corrosion resistances. Several intermetallic binary compounds have been synthesised using LRS-DAC systems from mixtures of their respective elements, including germanium tin (GeSn), indium antimonide (InSb), tungsten germanide, (W-Ge<sub>3</sub>), and iron bismuthide, (FeBi<sub>2</sub>) (Table 10). Also included here is the dissociation of water to “alloys” and ionic species at high pressures and temperatures observed by Lin et al. and Goncharov et al. [56,331].

**Table 10.** Intermetallics and Metallic Compounds: Metallic Compounds and Intermetallics Synthesised During Selected LRS-DAC Studies.

Product Material(s)	Precursor(s)	Press. [GPa]	Laser Type [nm or $\mu\text{m}$ ]	Laser Parameters: Pulse Length/Exposure Time [s], Powers/Energies [W/J], Spots [ $\mu\text{m}$ ], or Induced Temps. [K]	Refs.
$\text{O}_2\text{-H}_2$	$\text{H}_2\text{O}$	8.8	Data N/A	Up to 700 K	[331]
$\text{H}_3\text{O}^+, \text{OH}^-$	$\text{H}_2\text{O}$	56	Nd: YAG [1.06 $\mu\text{m}$ ]	5–20 s, [50 W], 20–30 $\mu\text{m}$ , 1600 K	[56]
GeSn	Ge, Sn	8	$\text{CO}_2$ [10.6 $\mu\text{m}$ ]	CW, [ $\leq 125$ W], $\approx 30$ $\mu\text{m}$ , up to 2000 K	[98]
InSb	In, Sb	a: 100, b: 0.2–10	$\text{CO}_2$ [10.6 $\mu\text{m}$ ]	a: $\text{CO}_2$ , 40 $\mu\text{m}$ , $\geq 5000$ K b: CW, [10–15 W], 20 $\mu\text{m}$	a: [250] b: [251]
$\text{WGe}_3$	W, Ge	2.6	Nd: YAG [1.06 $\mu\text{m}$ ]	CW, [30 W], $\approx 1274$ K	[332]
$\text{FeBi}_2$	Fe, Bi	32	Nd: YLF [1053 nm]	[170 W], 1400 K	[24]
$\text{Y}_2\text{ClC} + \text{Y}_2\text{Cl}$	Y, NaCl	41	Nd: YAG [1.06 $\mu\text{m}$ ]	2000 K	[333]
$\text{Dy}_2\text{ClC} + \text{DyCl}$	Dy, NaCl	40	Nd: YAG [1.06 $\mu\text{m}$ ]	2000 K	[333]
<i>HP-PdF<sub>2</sub>type-FeCl<sub>2</sub></i>	FeO, KCl	160	Nd: YAG [1.06 $\mu\text{m}$ ]	2100 K	[333]
CuBi	Cu, Bi	3.19–4.88	IR	$\sim 40$ $\mu\text{m}$ , $\sim 450$ K	[274]
$\text{Cu}_{11}\text{Bi}_7$	CuBi	4.16–10	IR	$\sim 40$ $\mu\text{m}$ , $\sim 920$ K	[274]

One thought-provoking article discussed the synthesis of the  $\text{FeBi}_2$  intermetallic by Walsh et al. in 2018 [24]. In addition to surveying similar work, they demonstrated the formation of a new intermetallic between two normally immiscible elements, Fe and Bi, for which there are no previously known intermetallics. As they state in their article, “the uncovered compounds represent the first intermetallics in their respective classes and hint at the enormous promise of this method as a way to isolate families of currently ‘impossible’ compounds”. This points the way for many others in their study of potential new intermetallic compounds using the LRS-DAC approach.

Another article focused on the HTHP dissociation of water ( $\text{H}_2\text{O}$ ) into its constitutive elements. This article is significant because the dissociation of water at high pressures and temperatures ultimately can affect the internal composition/structure within dwarf planets and similar planetary bodies; this could greatly revise current models of planetary dynamics.

## 6. Conclusions & Future Work

This article reviewed laser-induced reactive chemical processing within diamond anvil cells, where 186 articles have been published and over 100 separate materials have been synthesised so far. Clearly, there is an enormous potential for discovery in this field, where high pressures and laser excitation provide additional degrees of freedom to the thermodynamic phase space for materials synthesis. Many chemical reaction pathways that do not occur at STP may yet be realised at high pressures within a diamond anvil cell. For example, even normally stable compounds, e.g., water at STP, may be dissociated at high pressures and temperatures. Novel reactions have been observed at high pressures, such as the polymerisation of nitrogen, which ordinarily does not polymerise, as it is an extremely stable diatomic molecule. It is also clear that process kinetics within diamond anvil cells may be altered at high pressures relative to those at STP; indeed, one must

determine the sign of the volume activation energy,  $\Delta V^\ddagger$ , to determine whether a reaction rate will increase or decrease with pressure.

Much of the focus in the literature has been on the synthesis of novel binary metal nitrides, carbides, or diamond. However, new advanced functional materials, such as high temperature superconductors (viz. lanthanum-yttrium hydrides), or superhard materials (viz. rhenium carbides) have been developed. It has even been proposed that devices using these materials can be fabricated inside L-DACs. New compounds and novel phases of even highly unreactive materials, e.g., the platinum group metals, as well as uncommon materials, e.g., scandium carbide ( $\text{Sc}_4\text{C}_3$ ), have been synthesised, and new routes to diamond synthesis are being explored in the C-O-H system. Although some experiments emulating chemical reactions deep within terrestrial or icy planets have been carried out, much remains to be done to create realistic models. Currently, chemical reactions have been induced at pressures approaching 1 TPa, but many planetary/geochemical research questions will require even greater pressures.

To date, most LRS-DAC studies have employed cw lasers for thermally induced reactions (pyrolysis), rather than pulsed lasers. Few photolysis experiments have been conducted, and no experiments with short pulse lasers (<100 ps) appear in the literature (thus far). However, it is apparent in many cw laser experiments that extreme thermal gradients are present during LRS-DAC processing, which likely influence the transport and concentration of precursors during the reaction. It has also been observed that rapid mass transport may occur within an LRS-DAC, including convective mass and heat transfer when fluids are present. Finally, it was determined that the diffusive reaction flux for two (or more) reaction zones depends on the reaction zone radii,  $a_0$ , and the centre-to-centre distance between these zones,  $L$ . The mass transport (diffusion) limited reaction rate was shown to be proportional to the inverse of the reaction zone radius.

Throughout this review, it can be seen that there is vast potential for new discoveries to be made through LRS-DAC research, and that there remain many opportunities for important contributions to be made, such as: (1) the potential discovery of new binary and ternary intermetallic compounds, consisting of elements that ordinarily are considered normally immiscible or otherwise “impossible” to synthesise; (2) more exploratory research into the binary metal hydrides, borides, carbides, and oxides would be worthwhile; (3) LRS-DAC methods may ultimately provide a route to materials that exhibit room-temperature superconductivity, and more work should be done there; (4) there are massive opportunities to measure (and model) chemical kinetics at high pressures for the first time (and compare their differences to measurements at STP), thereby furthering the fundamental understanding of kinetics; (5) much more research into photoexcited or photolytic reactions could be carried out using modern, intense ultraviolet-visible tuneable lasers to achieve selective chemistry; (6) the exploration of reactive materials synthesis using modern ultrafast and short-pulsed lasers has yet to begin, where either heating can be minimised or thermally excited states can be accessed; (7) the use of short-pulsed lasers to simultaneously heat, shock, and induce chemical reactions has been minimal and is open for further investigation; (8) explorations of very extreme conditions, well above 7000 K (including plasmas), to induce chemical reactions have not been realised; (9) no detailed studies/modellings of reactive mass transport processes within diamond anvil cells have been carried out (an entirely new field); (10) there has been limited use of multiple laser spots within an L-DAC for the simultaneous processing of multiple samples, which can enhance the throughput of LRS-DAC experiments; (11) LRS-DAC methods have been limited to relatively small sample volumes, limiting this type of work to scientific examinations rather than manufacturing of commercial products; (12) few ternary, quaternary, and higher compounds (such as high-entropy alloys) have been investigated using LRS-DAC synthesis; (13) most chemical reactions have been either simple redox reactions or dissociation reactions involving two elements, rather than more complex molecules (e.g., CVD precursors with multiple ligands)—this presents many opportunities for innovation; and

finally, (14) further research into the mechanisms of diamond formation in the C-O-H and similar systems are needed. Indeed, the future looks bright for LRS-DAC-related research.

**Author Contributions:** Conceptualization, M.E.A. and J.L.M.; methodology, M.E.A.; investigation, M.E.A.; resources, M.E.A.; data curation, M.E.A.; writing—original draft preparation, M.E.A.; proofreading—review and editing, M.E.A., W.D.M., V.T. and J.L.M.; visualisation, M.E.A.; supervision, J.L.M.; project administration, J.L.M. All authors have read and agreed to the published version of the manuscript.

**Funding:** Funding provided by La Trobe University Research Infrastructure Fund.

**Institutional Review Board Statement:** Not applicable.

**Informed Consent Statement:** Not applicable.

**Data Availability Statement:** Not applicable.

**Acknowledgments:** We would like to thank C. Ada and the La Trobe University Research Infrastructure Fund for their generous support of fundamental high-pressure research within the EeMC<sup>2</sup> Labs. This work is dedicated to our parents and grandparents, who have greatly supported us in our education and research endeavors.

**Conflicts of Interest:** The authors declare no conflict of interest.

## References

1. Bini, R.; Schettino, V. *Materials Under Extreme Conditions: Molecular Crystals at High Pressure*; Imperial College Press: London, UK, 2014; Volume 1, p. 18.
2. Kestell, A.E.; DeLorey, G.T. *Nanoparticles: Properties, Classification, Characterization, and Fabrication: Properties, Classification, Characterization, and Fabrication*; Nova Science Publishers, Incorporated: Hauppauge, NY, USA, 2010.
3. Kim, T.; Hyeon, T. Applications of inorganic nanoparticles as therapeutic agents. *Nanotechnology* **2013**, *25*, 012001. [[CrossRef](#)] [[PubMed](#)]
4. Duong, T.-H.; Kim, H.-C. A high productivity and speedy synthesis process for copper nanowires via an ethylenediamine-mediated method. *Int. Nano Lett.* **2017**, *7*, 165–169. [[CrossRef](#)]
5. Ganachari, S.V.; Banapurmath, N.R.; Salimath, B.; Yaradoddi, J.S.; Shettar, A.S.; Hunashyal, A.M.; Venkataraman, A.; Patil, P.; Shoba, H.; Hiremath, G.B. Synthesis Techniques for Preparation of Nanomaterials. In *Handbook of Ecomaterials*; Martínez, L.M.T., Kharissova, O.V., Kharisov, B.I., Eds.; Springer International Publishing: Cham, Switzerland, 2019; pp. 83–103.
6. Ma, L.; Zhou, M.; Wang, Y.; Kawaguchi, S.; Ohishi, Y.; Peng, F.; Liu, H.; Liu, G.; Wang, H.; Ma, Y. Experimental clathrate superhydrides  $\text{EuH}_6$  and  $\text{EuH}_9$  at extreme pressure conditions. *Phys. Rev. Res.* **2021**, *3*, 043107. [[CrossRef](#)]
7. Arpita Aparajita, A.N.; Sanjay Kumar, N.R.; Chandra, S.; Amirthapandian, S.; Shekar, N.V.C.; Sridhar, K. High-Pressure Synthesis of Manganese Monocarbide: A Potential Superhard Material. *Inorg. Chem.* **2018**, *57*, 14178–14185. [[CrossRef](#)] [[PubMed](#)]
8. Bayarjargal, L.; Morgenroth, W.; Schrodt, N.; Winkler, B.; Milman, V.; Stanek, C.R.; Uberuaga, B.P. Synthesis of  $\text{Hf}_8\text{O}_7$ , a new binary hafnium oxide, at high pressures and high temperatures. *High Press. Res.* **2017**, *37*, 147–158. [[CrossRef](#)]
9. Watkins, E.B.; Huber, R.C.; Childs, C.M.; Salamat, A.; Pigott, J.S.; Chow, P.; Xiao, Y.; Coe, J.D. Diamond and methane formation from the chemical decomposition of polyethylene at high pressures and temperatures. *Sci. Rep.* **2022**, *12*, 631. [[CrossRef](#)]
10. Robertson, J. 3.06—Diamond-Like Carbon Films, Properties and Applications. In *Comprehensive Hard Materials*; Sarin, V.K., Ed.; Elsevier: Oxford, UK, 2014; pp. 101–139.
11. Taniguchi, T. 3.23—Synthesis and Properties of Single Crystalline cBN and Its Sintered Body. In *Comprehensive Hard Materials*; Sarin, V.K., Ed.; Elsevier: Oxford, UK, 2014; pp. 587–605.
12. Thapliyal, V.; Alabdulkarim, M.E.; Whelan, D.R.; Mainali, B.; Maxwell, J.L. A concise review of the Raman spectra of carbon allotropes. *Diam. Relat. Mater.* **2022**, *127*, 109180. [[CrossRef](#)]
13. Suzuki, S.; Niwa, K.; Honda, A.; Muto, S.; Ando, A.; Hasegawa, M. High-pressure synthesis and Sn valence state analysis of  $\text{BaTiO}_3$ - $\text{SnO}$  solid solution. *J. Mater. Res.* **2014**, *29*, 2928–2933. [[CrossRef](#)]
14. Sanjay Kumar, N.R.; Chandra Shekar, N.V.; Chandra, S.; Basu, J.; Divakar, R.; Sahu, P.C. Synthesis of novel  $\text{Ru}_2\text{C}$  under high pressure–high temperature conditions. *J. Phys. Condens. Matter* **2012**, *24*, 362202. [[CrossRef](#)]
15. Riedel, R.; Horvath-Bordon, E.; Kroll, P.; Mieke, G.; Dzivenko, D.; Kleebe, H.-J.; Aken, P.A.v.; Lauterbach, S. Novel binary and ternary phases in the Si-C-N system. *J. Ceram. Soc. Jpn.* **2008**, *116*, 674–680. [[CrossRef](#)]
16. Ratzker, B.; Wagner, A.; Favelukis, B.; Ayalon, I.; Shrem, R.; Kalabukhov, S.; Frage, N. Effect of synthesis route on optical properties of  $\text{Cr:Al}_2\text{O}_3$  transparent ceramics sintered under high pressure. *J. Alloys Compd.* **2022**, *913*, 165186. [[CrossRef](#)]
17. Juarez-Arellano, E.A.; Winkler, B.; Friedrich, A.; Bayarjargal, L.; Milman, V.; Yan, J.; Clark, S.M. Stability field of the high-(P, T)  $\text{Re}_2\text{C}$  phase and properties of an analogous osmium carbide phase. *J. Alloys Compd.* **2009**, *481*, 577–581. [[CrossRef](#)]
18. Ma, L.; Yang, X.; Liu, G.; Liu, H.; Yang, G.; Wang, H.; Cai, J.; Zhou, M.; Wang, H. Design and synthesis of clathrate  $\text{LaB}_8$  with superconductivity. *Phys. Rev. B* **2021**, *104*, 174112. [[CrossRef](#)]

19. Arpita Aparajita, A.N.; Sanjay Kumar, N.R.; Chandra, S.; Chandra Shekar, N.V.; Kalavathi, S. Synthesis of novel chromium carbide using laser heated diamond anvil cell. *J. Solid State Chem.* **2021**, *295*, 121899. [[CrossRef](#)]
20. Aslandukova, A.; Aslandukov, A.; Yuan, L.; Laniel, D.; Khandarkhaeva, S.; Fedotenko, T.; Steinle-Neumann, G.; Glazyrin, K.; Dubrovinskaia, N.; Dubrovinsky, L. Novel High-Pressure Yttrium Carbide  $\gamma$ -Y<sub>4</sub>C<sub>5</sub> Containing [C<sub>2</sub>] and Nonlinear [C<sub>3</sub>] Units with Unusually Large Formal Charges. *Phys. Rev. Lett.* **2021**, *127*, 135501. [[CrossRef](#)]
21. Daviau, K.; Lee, K.K.M. Experimental Constraints on Solid Nitride Phases in Rocky Mantles of Reduced Planets and Implications for Observable Atmosphere Compositions. *J. Geophys. Res. Planets* **2021**, *126*, e2020JE006687. [[CrossRef](#)]
22. Liu, Y.; Su, H.; Niu, C.; Wang, X.; Zhang, J.; Ge, Z.; Li, Y. Synthesis of black phosphorus structured polymeric nitrogen. *Chin. Phys. B* **2020**, *29*, 106201. [[CrossRef](#)]
23. Kronbo, C.H.; Ottesen, M.; Hansen, M.F.; Ehrenreich-Petersen, E.; Meng, Y.; Bremholm, M. Discovery of Rhombohedral NaIrO<sub>3</sub> Polymorph by In Situ High-Pressure Synthesis of High-Oxidation-State Materials Using Laser Heating in Diamond Anvil Cells. *Inorg. Chem.* **2020**, *59*, 15780–15787. [[CrossRef](#)]
24. Walsh, J.P.S.; Freedman, D.E. High-Pressure Synthesis: A New Frontier in the Search for Next-Generation Intermetallic Compounds. *Acc. Chem. Res.* **2018**, *51*, 1315–1323. [[CrossRef](#)] [[PubMed](#)]
25. Tamerius, A.D.; Clarke, S.M.; Gu, M.; Walsh, J.P.S.; Esters, M.; Meng, Y.; Hendon, C.H.; Rondinelli, J.M.; Jacobsen, S.D.; Freedman, D.E. Discovery of Cu<sub>3</sub>Pb. *Angew. Chem. Int. Ed.* **2018**, *57*, 12809–12813. [[CrossRef](#)] [[PubMed](#)]
26. Alabdulkarim, M.E.; Maxwell, W.D.; Thapliyal, V.; Maxwell, J.L. A Comprehensive Review of High-Pressure Laser-Induced Materials Processing, Part I: Laser-Heated Diamond Anvil Cells. *J. Manuf. Mater. Process.* **2022**, *6*, 111. [[CrossRef](#)]
27. Bassett, W.A. Diamond anvil cell, 50th birthday. *High Press. Res.* **2009**, *29*, 163–186. [[CrossRef](#)]
28. Shukla, B.; Shekar, N.V.C.; Kumar, N.R.S.; Ravindran, T.R.; Sahoo, P.; Dhara, S.; Sahu, P.C. Twin chamber sample assembly in DAC and HPHT studies on GaN nano-particles. *J. Phys. Conf. Ser.* **2012**, *377*, 012014. [[CrossRef](#)]
29. Shim, S.H.; Duffy, T.S.; Jeanloz, R.; Shen, G. Stability and crystal structure of MgSiO<sub>3</sub> perovskite to the core-mantle boundary. *Geophys. Res. Lett.* **2004**, *31*, GL019639. [[CrossRef](#)]
30. Santamaría-Pérez, D.; McGuire, C.; Makhluif, A.; Kavner, A.; Chuliá-Jordán, R.; Pellicer-Porres, J.; Martínez-García, D.; Doran, A.; Kunz, M.; Rodríguez-Hernández, P.; et al. Exploring the Chemical Reactivity between Carbon Dioxide and Three Transition Metals (Au, Pt, and Re) at High-Pressure, High-Temperature Conditions. *Inorg. Chem.* **2016**, *55*, 10793–10799. [[CrossRef](#)]
31. Chuliá-Jordán, R.; Santamaría-Pérez, D.; Marqueño, T.; Ruiz-Fuertes, J.; Daisenberger, D. Oxidation of High Yield Strength Metals Tungsten and Rhenium in High-Pressure High-Temperature Experiments of Carbon Dioxide and Carbonates. *Crystals* **2019**, *9*, 676. [[CrossRef](#)]
32. Beyer, M.K.; Clausen-Schaumann, H. Mechanochemistry: The Mechanical Activation of Covalent Bonds. *Chem. Rev.* **2005**, *105*, 2921–2948. [[CrossRef](#)]
33. Cruz, C. Ultrafast Spectroscopy of Force- or Light-induced Chemical and Electronic Changes in Condensed Phase Materials. Ph.D. Thesis, University of California, Ann Arbor, MI, USA, 2019.
34. Alabdulkarim, M.E.; Maxwell, W.D.; Thapliyal, V.; Maxwell, J.L. A Comprehensive Review of High-Pressure Laser-Induced Materials Processing, Part II: Laser-Driven Dynamic Compression within Diamond Anvil Cells. *J. Manuf. Mater. Process.* **2022**, *6*, 142. [[CrossRef](#)]
35. Dadashev, A.; Pasternak, M.P.; Rozenberg, G.K.; Taylor, R.D. Applications of perforated diamond anvils for very high-pressure research. *Rev. Sci. Instrum.* **2001**, *72*, 2633–2637. [[CrossRef](#)]
36. Shen, G.; Mao, H.K. High-pressure studies with x-rays using diamond anvil cells. *Rep. Prog. Phys.* **2016**, *80*, 016101. [[CrossRef](#)]
37. Lenz, J.A.; Perottoni, C.A.; Balzaretti, N.M.; Jornada, J.A.H.d. Processing of amorphous carbon films by ultrafast temperature treatment in a confined geometry. *J. Appl. Phys.* **2001**, *89*, 8284–8290. [[CrossRef](#)]
38. Jingzhu, H.; Jian, X.; Somayazulu, M.; Guo, Q.; Hemley, R.; Mao, H.K. X-ray diffraction and laser heating: Application of a moissanite anvil cell. *J. Phys. Condens. Matter* **2002**, *14*, 10479. [[CrossRef](#)]
39. Xu, J.-a.; Mao, H.-k.; Hemley, R.J. The gem anvil cell: High-pressure behaviour of diamond and related materials. *J. Phys. Condens. Matter* **2002**, *14*, 11549–11552. [[CrossRef](#)]
40. Kimura, T.; Ozaki, N.; Okuchi, T.; Terai, T.; Sano, T.; Shimizu, K.; Sano, T.; Koenig, M.; Hirose, A.; Kakeshita, T.; et al. Significant static pressure increase in a precompression cell target for laser-driven advanced dynamic compression experiments. *Phys. Plasma* **2010**, *17*, 054502. [[CrossRef](#)]
41. Patel, N.N.; Sunder, M.; Sharma, S.M. Laser heated diamond anvil cell facility for high temperature high pressure research: Application to material synthesis and melting studies. *Indian J. Phys.* **2018**, *92*, 1259–1269. [[CrossRef](#)]
42. Badding, J.V.; Nesting, D.C. Thermodynamic Analysis of the Formation of Carbon Nitrides under Pressure. *Chem. Mater.* **1996**, *8*, 535–540. [[CrossRef](#)]
43. Zhang, R. Pressure Effects on Crystal and Electronic Structures of Materials. Ph.D. Thesis, The University of Utah, Salt Lake City, UT, USA, 2018.
44. Drickamer, H.G.; Frank, C.W. Shifts of Energy Levels with Pressure. In *Electronic Transitions and the High Pressure Chemistry and Physics of Solids*; Springer: Dordrecht, The Netherlands, 1973; pp. 72–109.
45. Miao, M.; Sun, Y.; Zurek, E.; Lin, H. Chemistry under high pressure. *Nat. Rev. Chem.* **2020**, *4*, 508–527. [[CrossRef](#)]

46. Jeanloz, R.; Celliers Peter, M.; Collins Gilbert, W.; Eggert Jon, H.; Lee Kanani, K.M.; McWilliams, R.S.; Brygoo, S.; Loubeyre, P. Achieving high-density states through shock-wave loading of precompressed samples. *Proc. Natl. Acad. Sci. USA* **2007**, *104*, 9172–9177. [[CrossRef](#)]
47. Horvath-Bordon, E.; Riedel, R.; Zerr, A.; McMillan, P.F.; Auffermann, G.; Prots, Y.; Bronger, W.; Kniep, R.; Kroll, P. High-pressure chemistry of nitride-based materials. *Chem. Soc. Rev.* **2006**, *35*, 987–1014. [[CrossRef](#)]
48. Benedetti, L.R.; Nguyen, J.H.; Caldwell, W.A.; Liu, H.; Kruger, M.; Jeanloz, R. Dissociation of CH<sub>4</sub> at High Pressures and Temperatures: Diamond Formation in Giant Planet Interiors? *Science* **1999**, *286*, 100–102. [[CrossRef](#)]
49. Zerr, A.; Miehe, G.; Riedel, R. Synthesis of cubic zirconium and hafnium nitride having Th<sub>3</sub>P<sub>4</sub> structure. *Nat. Mater.* **2003**, *2*, 185–189. [[CrossRef](#)] [[PubMed](#)]
50. Somayazulu, M.; Ahart, M.; Mishra, A.K.; Geballe, Z.M.; Baldini, M.; Meng, Y.; Struzhkin, V.V.; Hemley, R.J. Evidence for Superconductivity above 260 K in Lanthanum Superhydride at Megabar Pressures. *Phys. Rev. Lett.* **2019**, *122*, 027001. [[CrossRef](#)] [[PubMed](#)]
51. Drozdov, A.P.; Kong, P.P.; Minkov, V.S.; Besedin, S.P.; Kuzovnikov, M.A.; Mozaffari, S.; Balicas, L.; Balakirev, F.F.; Graf, D.E.; Prakapenka, V.B.; et al. Superconductivity at 250 K in lanthanum hydride under high pressures. *Nature* **2019**, *569*, 528–531. [[CrossRef](#)] [[PubMed](#)]
52. Crowhurst, J.C.; Goncharov, A.F.; Sadigh, B.; Evans, C.L.; Morrall, P.G.; Ferreira, J.L.; Nelson, A.J. Synthesis and Characterization of the Nitrides of Platinum and Iridium. *Science* **2006**, *311*, 1275–1278. [[CrossRef](#)]
53. Young, A.F.; Sanloup, C.; Gregoryanz, E.; Scandolo, S.; Hemley, R.J.; Mao, H.-k. Synthesis of Novel Transition Metal Nitrides IrN<sub>2</sub> and OsN. *Phys. Rev. Lett.* **2006**, *96*, 155501. [[CrossRef](#)]
54. Gregoryanz, E.; Sanloup, C.; Somayazulu, M.; Badro, J.; Fiquet, G.; Mao, H.-K.; Hemley, R.J. Synthesis and characterization of a binary noble metal nitride. *Nat. Mater.* **2004**, *3*, 294–297. [[CrossRef](#)]
55. Hu, Q.; Kim, D.Y.; Yang, W.; Yang, L.; Meng, Y.; Zhang, L.; Mao, H.K. FeO<sub>2</sub> and FeOOH under deep lower-mantle conditions and Earth's oxygen-hydrogen cycles. *Nature* **2016**, *534*, 241–244. [[CrossRef](#)]
56. Goncharov, A.F.; Goldman, N.; Fried, L.E.; Crowhurst, J.C.; Kuo, I.F.W.; Mundy, C.J.; Zaug, J.M. Dynamic Ionization of Water under Extreme Conditions. *Phys. Rev. Lett.* **2005**, *94*, 125508. [[CrossRef](#)]
57. Ono, S.; Kikegawa, T.; Ohishi, Y. A high-pressure and high-temperature synthesis of platinum carbide. *Solid State Commun.* **2005**, *133*, 55–59. [[CrossRef](#)]
58. Biellmann, C.; Gillet, P.; Guyot, F.; Peyronneau, J.; Reynard, B. Experimental evidence for carbonate stability in the Earth's lower mantle. *Earth Planet. Sci. Lett.* **1993**, *118*, 31–41. [[CrossRef](#)]
59. Crowhurst, J.C.; Goncharov, A.F.; Sadigh, B.; Zaug, J.M.; Aberg, D.; Meng, Y.; Prakapenka, V.B. Synthesis and characterization of nitrides of iridium and palladium. *J. Mater. Res.* **2008**, *23*, 1–5. [[CrossRef](#)]
60. Semenok, D.V.; Kvashnin, A.G.; Ivanova, A.G.; Svitlyk, V.; Fomin, V.Y.; Sadakov, A.V.; Sobolevskiy, O.A.; Pudalov, V.M.; Troyan, I.A.; Oganov, A.R. Superconductivity at 161 K in thorium hydride ThH<sub>10</sub>: Synthesis and properties. *Mater. Today* **2020**, *33*, 36–44. [[CrossRef](#)]
61. Serghiou, G.; Miehe, G.; Tschauer, O.; Zerr, A.; Boehler, R. Synthesis of a cubic Ge<sub>3</sub>N<sub>4</sub> phase at high pressures and temperatures. *J. Chem. Phys.* **1999**, *111*, 4659–4662. [[CrossRef](#)]
62. Friedrich, A.; Winkler, B.; Bayarjargal, L.; Morgenroth, W.; Juarez-Arellano, E.A.; Milman, V.; Refson, K.; Kunz, M.; Chen, K. Novel Rhenium Nitrides. *Phys. Rev. Lett.* **2010**, *105*, 085504. [[CrossRef](#)] [[PubMed](#)]
63. Citroni, M.; Ceppatelli, M.; Bini, R.; Schettino, V. Laser-Induced Selectivity for Dimerization Versus Polymerization of Butadiene Under Pressure. *Science* **2002**, *295*, 2058–2060. [[CrossRef](#)] [[PubMed](#)]
64. Bykova, E.; Dubrovinsky, L.; Dubrovinskaia, N.; Bykov, M.; McCammon, C.; Ovsyannikov, S.V.; Liermann, H.P.; Kuppenko, I.; Chumakov, A.I.; Rüffer, R.; et al. Structural complexity of simple Fe<sub>2</sub>O<sub>3</sub> at high pressures and temperatures. *Nat. Commun.* **2016**, *7*, 10661. [[CrossRef](#)]
65. Bykov, M.; Bykova, E.; Aprilis, G.; Glazyrin, K.; Koemets, E.; Chuvashova, I.; Kuppenko, I.; McCammon, C.; Mezouar, M.; Prakapenka, V.; et al. Fe-N system at high pressure reveals a compound featuring polymeric nitrogen chains. *Nat. Commun.* **2018**, *9*, 2756. [[CrossRef](#)] [[PubMed](#)]
66. Takafuji, N.; Hirose, K.; Mitome, M.; Bando, Y. Solubilities of O and Si in liquid iron in equilibrium with (Mg,Fe)SiO<sub>3</sub> perovskite and the light elements in the core. *Geophys. Res. Lett.* **2005**, *32*. [[CrossRef](#)]
67. Pépin, C.M.; Geneste, G.; Dewaele, A.; Mezouar, M.; Loubeyre, P. Synthesis of FeH<sub>5</sub>: A layered structure with atomic hydrogen slabs. *Science* **2017**, *357*, 382–385. [[CrossRef](#)]
68. Caldwell, W.A.; Nguyen, J.H.; Pfrommer, B.G.; Mauri, F.; Louie, S.G.; Jeanloz, R. Structure, Bonding, and Geochemistry of Xenon at High Pressures. *Science* **1997**, *277*, 930–933. [[CrossRef](#)]
69. Friedrich, A.; Winkler, B.; Juarez-Arellano, E.A.; Bayarjargal, L. Synthesis of Binary Transition Metal Nitrides, Carbides and Borides from the Elements in the Laser-Heated Diamond Anvil Cell and Their Structure-Property Relations. *Materials* **2011**, *4*, 1648–1692. [[CrossRef](#)]
70. Kolesnikov, A.; Kutcherov, V.G.; Goncharov, A.F. Methane-derived hydrocarbons produced under upper-mantle conditions. *Nat. Geosci.* **2009**, *2*, 566–570. [[CrossRef](#)]

71. Hasegawa, M.; Yagi, T. Systematic Study of Formation and Crystal Structure of 3d-Transition Metal Nitrides Synthesized in a Supercritical Nitrogen Fluid under 10 GPa and 1800 K Using Diamond Anvil Cell and YAG Laser Heating. *ChemInform* **2006**, *37*, 131–142. [[CrossRef](#)]
72. Dong, X.; Oganov, A.R.; Goncharov, A.F.; Stavrou, E.; Lobanov, S.; Saleh, G.; Qian, G.-R.; Zhu, Q.; Gatti, C.; Deringer, V.L.; et al. A stable compound of helium and sodium at high pressure. *Nat. Chem.* **2017**, *9*, 440–445. [[CrossRef](#)] [[PubMed](#)]
73. Kiefer, B.; Duffy, T.S. Finite element simulations of the laser-heated diamond-anvil cell. *J. Appl. Phys.* **2005**, *97*, 114902. [[CrossRef](#)]
74. Citroni, M.; Ceppatelli, M.; Bini, R.; Schettino, V. Dimerization and Polymerization of Isoprene at High Pressures. *J. Phys. Chem. B* **2007**, *111*, 3910–3917. [[CrossRef](#)]
75. Hirai, H.; Konagai, K.; Kawamura, T.; Yamamoto, Y.; Yagi, T. Polymerization and diamond formation from melting methane and their implications in ice layer of giant planets. *Phys. Earth Planet. Inter.* **2009**, *174*, 242–246. [[CrossRef](#)]
76. Ceppatelli, M.; Bini, R.; Schettino, V. High-Pressure Reactivity of Model Hydrocarbons Driven by Near-UV Photodissociation of Water. *J. Phys. Chem. B* **2009**, *113*, 14640–14647. [[CrossRef](#)]
77. Peiris, S.M.; Russell, T.P. Photolysis of Compressed Sodium Azide (NaN<sub>3</sub>) as a Synthetic Pathway to Nitrogen Materials. *J. Phys. Chem. A* **2003**, *107*, 944–947. [[CrossRef](#)]
78. Ceppatelli, M.; Fanetti, S.; Citroni, M.; Bini, R. Photoinduced Reactivity of Liquid Ethanol at High Pressure. *J. Phys. Chem. B* **2010**, *114*, 15437–15444. [[CrossRef](#)]
79. Zerr, A.; Serghiou, G.; Boehler, R.; Ross, M. Decomposition of alkanes at high pressures and temperatures. *High Press. Res.* **2006**, *26*, 23–32. [[CrossRef](#)]
80. Tschauer, O.; Mao, H.-k.; Hemley, R.J. New Transformations of CO<sub>2</sub> at High Pressures and Temperatures. *Phys. Rev. Lett.* **2001**, *87*, 075701. [[CrossRef](#)] [[PubMed](#)]
81. Dorfman, S.M.; Nabie, F.; Boukaré, C.-E.; Prakapenka, V.B.; Cantoni, M.; Badro, J.; Gillet, P. Composition and Pressure Effects on Partitioning of Ferrous Iron in Iron-Rich Lower Mantle Heterogeneities. *Minerals* **2021**, *11*, 512. [[CrossRef](#)]
82. Aprilis, G.; Pakhomova, A.; Chariton, S.; Khandarkhaeva, S.; Melai, C.; Bykova, E.; Bykov, M.; Fedotenko, T.; Koemets, E.; McCammon, C.; et al. The Effect of Pulsed Laser Heating on the Stability of Ferropicicase at High Pressures. *Minerals* **2020**, *10*, 542. [[CrossRef](#)]
83. Bayarjargal, L.; Shumilova, T.G.; Friedrich, A.; Winkler, B.R. Diamond formation from CaCO<sub>3</sub> at high pressure and temperature. *Eur. J. Mineral.* **2010**, *22*, 29–34. [[CrossRef](#)]
84. Dubrovinsky, L.; Khandarkhaeva, S.; Fedotenko, T.; Laniel, D.; Bykov, M.; Giacobbe, C.; Lawrence Bright, E.; Sedmak, P.; Chariton, S.; Prakapenka, V.; et al. Materials synthesis at terapascal static pressures. *Nature* **2022**, *605*, 274–278. [[CrossRef](#)]
85. Lee, S.H.; Lee, J.S.; Park, S.; Choi, Y.K. Numerical Analysis on Heat Transfer Characteristics of A Silicon Film Irradiated by Pico-To Femtosecond Pulse Lasers. *Numer. Heat Transf. Part A* **2003**, *44*, 833–850. [[CrossRef](#)]
86. Karu, T.I.; Tiphlova, O.A.; Matveyets Yu, A.; Yartsev, A.P.; Letokhov, V.S. Comparison of the effects of visible femtosecond laser pulses and continuous wave laser radiation of low average intensity on the clonogenicity of *Escherichia coli*. *J. Photochem. Photobiol. B* **1991**, *10*, 339–344. [[CrossRef](#)]
87. Du, Z.; Amulele, G.; Benedetti, L.R.; Lee, K.K. Mapping temperatures and temperature gradients during flash heating in a diamond-anvil cell. *Rev. Sci. Instrum.* **2013**, *84*, 075111. [[CrossRef](#)]
88. Bunn, H.A.; Schultz, C.P.; Jernigan, C.M.; Widicus Weaver, S.L. Laser-Induced Chemistry Observed during 248 nm Vacuum Ultraviolet Photolysis of an O<sub>3</sub> and CH<sub>3</sub>NH<sub>2</sub> Mixture. *J. Phys. Chem. A* **2020**, *124*, 10838–10848. [[CrossRef](#)]
89. Huang, L.; Zeng, L.; Chen, Y.; Yu, N.; Wang, L.; Huang, K.; Zhao, Y.; Han, G. Long wavelength single photon like driven photolysis via triplet triplet annihilation. *Nat. Commun.* **2021**, *12*, 122. [[CrossRef](#)] [[PubMed](#)]
90. Toyota, K.; Nakashima, S.; Okada, T. Near-infrared laser-induced breakdown of liquid benzene. *Chem. Phys. Lett.* **2000**, *323*, 323–328. [[CrossRef](#)]
91. Wallace, M. High-Pressure High-Temperature (HPHT) Synthesis of Functional Materials. In *Sintering of Functional Materials*; Igor, S., Ed.; IntechOpen: Rijeka, Croatia, 2017; Chapter 8.
92. Tokita, M. Progress of Spark Plasma Sintering (SPS) Method, Systems, Ceramics Applications and Industrialization. *Ceramics* **2021**, *4*, 160–198. [[CrossRef](#)]
93. Stokes, C.S. Chemistry in High Temperature Plasma Jets. In *Chemical Reactions in Electrical Discharges*; Advances in Chemistry; American Chemical Society: Washington, DC, USA, 1969; Volume 80, pp. 390–405.
94. Ridha, F.; Junus, S.; Darsin, M. Synthesis of Zinc Oxide (ZnO) Nanoparticle using Non-Transferred DC Thermal Plasma Method: A Morphology Review. *Int. J. Emerg. Trends Eng. Res.* **2021**, *9*, 983–987. [[CrossRef](#)]
95. Elaissi, S.; Ben Gouider Trabelsi, A.; Alkallas, F.H.; Alrebdi, T.A.; Charrada, K. Modeling of Advanced Silicon Nanomaterial Synthesis Approach: From Reactive Thermal Plasma Jet to Nanosized Particles. *Nanomaterials* **2022**, *12*, 1763. [[CrossRef](#)]
96. Yoo, C.S.; Akella, J.; Cynn, H.; Nicol, M. Direct elementary reactions of boron and nitrogen at high pressures and temperatures. *Phys. Rev. B Condens. Matter* **1997**, *56*, 140–146. [[CrossRef](#)]
97. Sahu, P.C.; Takemura, K.; Yusa, H. Synthesis experiments on B-Sb, Ge-Sb, and Xe-Pd systems using a laser heated diamond anvil cell. *High Press. Res.* **2001**, *21*, 41–50. [[CrossRef](#)]
98. Sorb, Y.A.; Subramanian, N.; Ravindran, T.R.; Sahu, P.C. High Pressure in situ Micro-Raman Spectroscopy of Ge-Sn System Synthesized in a Laser Heated Diamond Anvil Cell. *AIP Conf. Proc.* **2011**, *1349*, 1305–1306. [[CrossRef](#)]

99. Fedotenko, T.; Dubrovinsky, L.; Khandarkhaeva, S.; Chariton, S.; Koemets, E.; Koemets, I.; Hanfland, M.; Dubrovinskaia, N. Synthesis of palladium carbides and palladium hydride in laser heated diamond anvil cells. *J. Alloys Compd.* **2020**, *844*, 156179. [[CrossRef](#)]
100. Gréaux, S.; Andraut, D.; Gautron, L.; Bolfan-Casanova, N.; Mezouar, M. Compressibility of  $\text{Ca}_3\text{Al}_2\text{Si}_3\text{O}_{12}$  perovskite up to 55 GPa. *Phys. Chem. Miner.* **2014**, *41*, 419–429. [[CrossRef](#)]
101. Semenov, D.V.; Troyan, I.A.; Ivanova, A.G.; Kvashnin, A.G.; Kruglov, I.A.; Hanfland, M.; Sadakov, A.V.; Sobolevskiy, O.A.; Pervakov, K.S.; Lyubutin, I.S.; et al. Superconductivity at 253 K in lanthanum–yttrium ternary hydrides. *Mater. Today* **2021**, *48*, 18–28. [[CrossRef](#)]
102. Ceppatelli, M.; Bini, R.; Schettino, V. High-pressure reactivity of clathrate hydrates by two-photon dissociation of water. *Phys. Chem. Chem. Phys.* **2011**, *13*, 1264–1275. [[CrossRef](#)]
103. Ceppatelli, M.; Bini, R.; Schettino, V. High-pressure photodissociation of water as a tool for hydrogen synthesis and fundamental chemistry. *Proc. Natl. Acad. Sci. USA* **2009**, *106*, 11454–11459. [[CrossRef](#)] [[PubMed](#)]
104. Mao, W.L.; Mao, H.-k.; Meng, Y.; Eng, P.J.; Hu, M.Y.; Chow, P.; Cai, Y.Q.; Shu, J.; Hemley, R.J. X-ray-Induced Dissociation of  $\text{H}_2\text{O}$  and Formation of an  $\text{O}_2\text{-H}_2$  Alloy at High Pressure. *Science* **2006**, *314*, 636–638. [[CrossRef](#)]
105. Duffy, T.S.; Smith, R.F. Ultra-High Pressure Dynamic Compression of Geological Materials. *Front. Earth Sci.* **2019**, *7*. [[CrossRef](#)]
106. Yoo, C.-S.; Wei, H.; Dias, R.; Shen, G.; Smith, J.; Chen, J.-Y.; Evans, W. Time-Resolved Synchrotron X-ray Diffraction on Pulse Laser Heated Iron in Diamond Anvil Cell. *J. Phys. Conf. Ser.* **2012**, *377*, 012108. [[CrossRef](#)]
107. Dewaele, A.; Mezouar, M.; Guignot, N.; Loubeyre, P. High melting points of tantalum in a laser-heated diamond anvil cell. *Phys. Rev. Lett.* **2010**, *104*, 255701. [[CrossRef](#)] [[PubMed](#)]
108. Andraut, D.; Fiquet, G.; Kunz, M.; Visocekas, F.; Häusermann, D. The Orthorhombic Structure of Iron: An In Situ Study at High-Temperature and High-Pressure. *Science* **1997**, *278*, 831–834. [[CrossRef](#)]
109. Armstrong, L.S.; Walter, M.J. Tetragonal almandine pyrope phase (TAPP): Retrograde Mg-perovskite from subducted oceanic crust? *Eur. J. Mineral.* **2012**, *24*, 587–597. [[CrossRef](#)]
110. Armstrong, L.S.; Walter, M.J.; Tuff, J.R.; Lord, O.T.; Lennie, A.R.; Klepe, A.K.; Clark, S.M. Perovskite Phase Relations in the System  $\text{CaO-MgO-TiO}_2\text{-SiO}_2$  and Implications for Deep Mantle Lithologies. *J. Petrol.* **2012**, *53*, 611–635. [[CrossRef](#)]
111. Benedetti, L.R.; Loubeyre, P. Temperature gradients, wavelength-dependent emissivity, and accuracy of high and very-high temperatures measured in the laser-heated diamond cell. *High Press. Res.* **2004**, *24*, 423–445. [[CrossRef](#)]
112. Boehler, R. Melting of the  $\text{FeFeO}$  and the  $\text{FeFeS}$  systems at high pressure: Constraints on core temperatures. *Earth Planet. Sci. Lett.* **1992**, *111*, 217–227. [[CrossRef](#)]
113. Boehler, R. Temperatures in the Earth's core from melting-point measurements of iron at high static pressures. *Nature* **1993**, *363*, 534–536. [[CrossRef](#)]
114. Boehler, R.; Ross, M.; Boercker, D.B. High-pressure melting curves of alkali halides. *Phys. Rev. B Condens. Matter* **1996**, *53*, 556–563. [[CrossRef](#)] [[PubMed](#)]
115. Boehler, R.; Chopelas, A. A new approach to laser heating in high pressure mineral physics. *Geophys. Res. Lett.* **1991**, *18*, 1147–1150. [[CrossRef](#)]
116. Boehler, R.; Ross, M.; Boercker, D.B. Melting of  $\text{LiF}$  and  $\text{NaCl}$  to 1 Mbar: Systematics of Ionic Solids at Extreme Conditions. *Phys. Rev. Lett.* **1997**, *78*, 4589–4592. [[CrossRef](#)]
117. Bolfan-Casanova, N.; Andraut, D.; Amiguet, E.; Guignot, N. Equation of state and post-stishovite transformation of Al-bearing silica up to 100GPa and 3000K. *Phys. Earth Planet. Inter.* **2009**, *174*, 70–77. [[CrossRef](#)]
118. Meade, C.; Mao, H.K.; Hu, J. High-Temperature Phase Transition and Dissociation of  $(\text{Mg, Fe})\text{SiO}_3$  Perovskite at Lower Mantle Pressures. *Science* **1995**, *268*, 1743–1745. [[CrossRef](#)]
119. Dewaele, A.; Mezouar, M.; Guignot, N.; Loubeyre, P. Melting of lead under high pressure studied using second-scale time-resolved x-ray diffraction. *Phys. Rev. B Condens. Matter* **2007**, *76*, 144106. [[CrossRef](#)]
120. Dewaele, A.; Belonoshko, A.B.; Garbarino, G.; Ocelli, F.; Bouvier, P.; Hanfland, M.; Mezouar, M. High-pressure–high-temperature equation of state of  $\text{KCl}$  and  $\text{KBr}$ . *Phys. Rev. B Condens. Matter* **2012**, *85*, 214105. [[CrossRef](#)]
121. Dobson, D.P.; Hunt, S.A.; Ahmed, J.; Lord, O.T.; Wann, E.T.H.; Santangeli, J.; Wood, I.G.; Vočadlo, L.; Walker, A.M.; Thomson, A.R.; et al. The phase diagram of  $\text{NiSi}$  under the conditions of small planetary interiors. *Phys. Earth Planet. Inter.* **2016**, *261*, 196–206. [[CrossRef](#)]
122. Dubrovinsky, L.S.; Saxena, S.K.; Lazor, P.; Ahuja, R.; Eriksson, O.; Wills, J.M.; Johansson, B. Experimental and theoretical identification of a new high-pressure phase of silica. *Nature* **1997**, *388*, 362–365. [[CrossRef](#)]
123. Errandonea, D.; Schwager, B.; Ditz, R.; Gessmann, C.; Boehler, R.; Ross, M. Systematics of transition-metal melting. *Phys. Rev. B Condens. Matter* **2001**, *63*, 132104. [[CrossRef](#)]
124. Errandonea, D.; Somayazulu, M.; Häusermann, D.; Mao, H.K. Melting of tantalum at high pressure determined by angle dispersive x-ray diffraction in a double-sided laser-heated diamond-anvil cell. *J. Phys. Condens. Matter* **2003**, *15*, 7635–7649. [[CrossRef](#)]
125. Errandonea, D.; Boehler, R.; Japel, S.; Mezouar, M.; Benedetti, L.R. Structural transformation of compressed solid Ar: An X-ray diffraction study to 114 GPa. *Phys. Rev. B Condens. Matter* **2006**, *73*, 092106. [[CrossRef](#)]

126. Errandonea, D.; MacLeod, S.G.; Burakovsky, L.; Santamaria-Perez, D.; Proctor, J.E.; Cynn, H.; Mezouar, M. Melting curve and phase diagram of vanadium under high-pressure and high-temperature conditions. *Phys. Rev. B Condens. Matter* **2019**, *100*, 094111. [[CrossRef](#)]
127. Fedotenko, T.; Dubrovinsky, L.; Aprilis, G.; Koemets, E.; Snigirev, A.; Snigireva, I.; Barannikov, A.; Ershov, P.; Cova, F.; Hanfland, M.; et al. Laser heating setup for diamond anvil cells for in situ synchrotron and in house high and ultra-high pressure studies. *Rev. Sci. Instrum.* **2019**, *90*, 104501–104511. [[CrossRef](#)]
128. Fiquet, G.; Andrault, D. Powder X-ray diffraction under extreme conditions of pressure and temperature. *J. Synchrotron Radiat.* **1999**, *6*, 81–86. [[CrossRef](#)]
129. Fiquet, G.; Andrault, D.; Itié, J.P.; Gillet, P.; Richet, P. X-ray diffraction of periclase in a laser-heated diamond-anvil cell. *Phys. Earth Planet. Inter.* **1996**, *95*, 1–17. [[CrossRef](#)]
130. Fiquet, G.; Dewaele, A.; Andrault, D.; Kunz, M.; Le Bihan, T. Thermoelastic properties and crystal structure of MgSiO<sub>3</sub> perovskite at lower mantle pressure and temperature conditions. *Geophys. Res. Lett.* **2000**, *27*, 21–24. [[CrossRef](#)]
131. Friedrich, A.; Morgenroth, W.; Bayarjargal, L.; Juarez-Arellano, E.A.; Winkler, B.; Konôpková, Z. In situ study of the high pressure high-temperature stability field of TaN and of the compressibilities of  $\vartheta$ -TaN and TaON. *High Press. Res.* **2013**, *33*, 633–641. [[CrossRef](#)]
132. Golberg, D.; Bando, Y.; Eremets, M.; Takemura, K.; Kurashima, K.; Yusa, H. Nanotubes in boron nitride laser heated at high pressure. *Appl. Phys. Lett.* **1996**, *69*, 2045–2047. [[CrossRef](#)]
133. Heinz, D.L.; Sweeney, J.S.; Miller, P. A laser heating system that stabilizes and controls the temperature: Diamond anvil cell applications. *Rev. Sci. Instrum.* **1991**, *62*, 1568–1575. [[CrossRef](#)]
134. Hrubyak, R.; Meng, Y.; Shen, G. Microstructures define melting of molybdenum at high pressures. *Nat. Commun.* **2017**, *8*, 14562. [[CrossRef](#)] [[PubMed](#)]
135. Huang, X.; Li, F.; Zhou, Q.; Meng, Y.; Litasov, K.D.; Wang, X.; Liu, B.; Cui, T. Thermal equation of state of Molybdenum determined from in situ synchrotron X-ray diffraction with laser-heated diamond anvil cells. *Sci. Rep.* **2016**, *6*, 19923. [[CrossRef](#)] [[PubMed](#)]
136. Japel, S.; Schwager, B.; Boehler, R.; Ross, M. Melting of copper and nickel at high pressure: The role of d electrons. *Phys. Rev. Lett.* **2005**, *95*, 167801. [[CrossRef](#)]
137. Kavner, A.; Duffy, T.S. Pressure–volume–temperature paths in the laser-heated diamond anvil cell. *J. Appl. Phys.* **2001**, *89*, 1907–1914. [[CrossRef](#)]
138. Kesson, S.E.; Fitz Gerald, J.D. Partitioning of MgO, FeO, NiO, MnO and Cr<sub>2</sub>O<sub>3</sub> between magnesian silicate perovskite and magnesiowüstite: Implications for the origin of inclusions in diamond and the composition of the lower mantle. *Earth Planet. Sci. Lett.* **1992**, *111*, 229–240. [[CrossRef](#)]
139. Kesson, S.E.; Fitz Gerald, J.D.; Shelley, J.M.G. Mineral chemistry and density of subducted basaltic crust at lower-mantle pressures. *Nature* **1994**, *372*, 767–769. [[CrossRef](#)]
140. Kim, Y.-H.; Ming, L.C.; Manghnani, M.H. High-pressure phase transformations in a natural crystalline diopside and a synthetic CaMgSi<sub>2</sub>O<sub>6</sub> glass. *Phys. Earth Planet. Inter.* **1994**, *83*, 67–79. [[CrossRef](#)]
141. Kimura, T.; Kuwayama, Y.; Yagi, T. Melting temperatures of H<sub>2</sub>O up to 72 GPa measured in a diamond anvil cell using CO<sub>2</sub> laser heating technique. *J. Chem. Phys.* **2014**, *140*, 074501. [[CrossRef](#)]
142. Young-Ho, K.O.; Kyoung Hun, O.H.; Kwang Joo, K.I.M. Installation and Operation of a Double-Sided Laser Heating System for the Synthesis of Novel Materials Under Extreme Conditions. *Sae Mulli (NPSM)* **2019**, *69*, 1107–1114. [[CrossRef](#)]
143. Knittle, E.; Jeanloz, R. Synthesis and Equation of State of (Mg,Fe) SiO<sub>3</sub> Perovskite to Over 100 Gigapascals. *Science* **1987**, *235*, 668–670. [[CrossRef](#)] [[PubMed](#)]
144. Sanjay, N.R.; Kumar, N.; Chandra Shekar, N.V.; Sekar, M.; Natarajan, S.; Mohan, P.; Srinivasan, M.; Padmanabhan, P.; Sahu, P.C. Diamond and diamond-like carbon in laser heated diamond anvil cell at 16.5 GPa and above 2000 K from pyrolytic graphite. *Indian J. Pure Appl. Phys.* **2008**, *46*, 783–787.
145. Kuppenko, I.; Strohm, C.; McCammon, C.; Cerantola, V.; Glazyrin, K.; Petitgirard, S.; Vasiukov, D.; Aprilis, G.; Chumakov, A.I.; Rüffer, R.; et al. Time differentiated nuclear resonance spectroscopy coupled with pulsed laser heating in diamond anvil cells. *Rev. Sci. Instrum.* **2015**, *86*, 114501. [[CrossRef](#)]
146. Lavina, B.; Dera, P.; Kim, E.; Meng, Y.; Downs Robert, T.; Weck Philippe, F.; Sutton Stephen, R.; Zhao, Y. Discovery of the recoverable high-pressure iron oxide Fe<sub>4</sub>O. *Proc. Natl. Acad. Sci. USA* **2011**, *108*, 17281–17285. [[CrossRef](#)] [[PubMed](#)]
147. Lazicki, A.; Dewaele, A.; Loubeyre, P.; Mezouar, M. High-pressure–temperature phase diagram and the equation of state of beryllium. *Phys. Rev. B Condens. Matter* **2012**, *86*, 174118. [[CrossRef](#)]
148. Lin, J.-F.; Santoro, M.; Struzhkin, V.V.; Mao, H.-k.; Hemley, R.J. In situ high pressure-temperature Raman spectroscopy technique with laser-heated diamond anvil cells. *Rev. Sci. Instrum.* **2004**, *75*, 3302–3306. [[CrossRef](#)]
149. Lin, J.-F.; Sturhahn, W.; Zhao, J.; Shen, G.; Mao, H.-K.; Hemley, R.J. Absolute temperature measurement in a laser-heated diamond anvil cell. *Geophys. Res. Lett.* **2004**, *31*, L14611. [[CrossRef](#)]
150. Lin, Y.; Hu, Q.; Zhu, L.; Meng, Y. Structure and Stability of Iron Fluoride at High Pressure–Temperature and Implication for a New Reservoir of Fluorine in the Deep Earth. *Minerals* **2020**, *10*, 783. [[CrossRef](#)]
151. Liu, L.-G. A new high-pressure phase of spinel. *Earth Planet. Sci. Lett.* **1978**, *41*, 398–404. [[CrossRef](#)]
152. Liu, L.-G. High pressure NaAlSiO<sub>4</sub>: The first silicate calcium ferrite isotype. *Geophys. Res. Lett.* **1977**, *4*, 183–186. [[CrossRef](#)]

153. Liu, J.; Wang, C.; Lv, C.; Su, X.; Liu, Y.; Tang, R.; Chen, J.; Hu, Q.; Mao, H.-K.; Mao, W.L. Evidence for oxygenation of Fe-Mg oxides at mid-mantle conditions and the rise of deep oxygen. *Natl. Sci. Rev.* **2020**, *8*, 1–6. [[CrossRef](#)] [[PubMed](#)]
154. Lord, O.T.; Wann, E.T.H.; Hunt, S.A.; Walker, A.M.; Santangeli, J.; Walter, M.J.; Dobson, D.P.; Wood, I.G.; Vočadlo, L.; Morard, G.; et al. The NiSi melting curve to 70GPa. *Phys. Earth Planet. Inter.* **2014**, *233*, 13–23. [[CrossRef](#)]
155. Lord, O.T.; Wood, I.G.; Dobson, D.P.; Vočadlo, L.; Wang, W.; Thomson, A.R.; Wann, E.T.H.; Morard, G.; Mezouar, M.; Walter, M.J. The melting curve of Ni to 1 Mbar. *Earth Planet. Sci. Lett.* **2014**, *408*, 226–236. [[CrossRef](#)]
156. Meng, Y.; Shen, G.; Mao, H.K. Double-sided laser heating system at HPCAT for *in situ* x-ray diffraction at high pressures and high temperatures. *J. Phys. Condens. Matter* **2006**, *18*, S1097–S1103. [[CrossRef](#)]
157. Ming, L.c.; Bassett, W.A. Laser heating in the diamond anvil press up to 2000°C sustained and 3000°C pulsed at pressures up to 260 kilobars. *Rev. Sci. Instrum.* **1974**, *45*, 1115–1118. [[CrossRef](#)]
158. Miyagi, L.; Kanitpanyacharoen, W.; Raju, S.V.; Kaercher, P.; Knight, J.; MacDowell, A.; Wenk, H.-R.; Williams, Q.; Alarcon, E.Z. Combined resistive and laser heating technique for *in situ* radial X-ray diffraction in the diamond anvil cell at high pressure and temperature. *Rev. Sci. Instrum.* **2013**, *84*, 025118. [[CrossRef](#)]
159. Nabiei, F.; Badro, J.; Boukaré, C.; Hébert, C.; Cantoni, M.; Borensztajn, S.; Wehr, N.; Gillet, P. Investigating Magma Ocean Solidification on Earth Through Laser-Heated Diamond Anvil Cell Experiments. *Geophys. Res. Lett.* **2021**, *48*, e2021GL092446. [[CrossRef](#)]
160. Ohfujii, H.; Irifune, T.; Okada, T.; Yagi, T.; Sumiya, H. Laser heating in nano-polycrystalline diamond anvil cell. *J. Phys. Conf. Ser.* **2010**, *215*, 5. [[CrossRef](#)]
161. Ohtaka, O.; Andraut, D.; Bouvier, P.; Schultz, E.; Mezouar, M. Phase relations and equation of state of ZrO<sub>2</sub> to 100 GPa. *J. Appl. Crystallogr.* **2005**, *38*, 727–733. [[CrossRef](#)]
162. Panero, W.R.; Jeanloz, R. Temperature gradients in the laser-heated diamond anvil cell. *J. Geophys. Res. Solid Earth* **2001**, *106*, 6493–6498. [[CrossRef](#)]
163. Santamaría-Pérez, D.; Boehler, R. FeSi melting curve up to 70 GPa. *Earth Planet. Sci. Lett.* **2008**, *265*, 743–747. [[CrossRef](#)]
164. Pigott, J.S.; Reaman, D.M.; Panero, W.R. Microfabrication of controlled-geometry samples for the laser-heated diamond-anvil cell using focused ion beam technology. *Rev. Sci. Instrum.* **2011**, *82*, 115106. [[CrossRef](#)] [[PubMed](#)]
165. Pigott, J.S.; Velisavljevic, N.; Moss, E.K.; Draganic, N.; Jacobsen, M.K.; Meng, Y.; Hrubiak, R.; Sturtevant, B.T. Experimental melting curve of zirconium metal to 37 GPa. *J. Phys. Condens. Matter* **2020**, *32*, 355402. [[CrossRef](#)]
166. Polvani, D.A.; Meng, J.F.; Hasegawa, M.; Badding, J.V. Measurement of the thermoelectric power of very small samples at ambient and high pressures. *Rev. Sci. Instrum.* **1999**, *70*, 3586–3589. [[CrossRef](#)]
167. Prakapenka, V.B.; Kubo, A.; Kuznetsov, A.; Laskin, A.; Shkurikhin, O.; Dera, P.; Rivers, M.L.; Sutton, S.R. Advanced flat top laser heating system for high pressure research at GSECARS: Application to the melting behavior of germanium. *High Press. Res.* **2008**, *28*, 225–235. [[CrossRef](#)]
168. Prakapenka, V.B.; Shen, G.; Dubrovinsky, L.S. Carbon transport in diamond anvil cells. *High Temp.-High Press.* **2003**, *35/36*, 237–249. [[CrossRef](#)]
169. Raju, S.V.; Hrubiak, R.; Drozd, V.; Saxena, S. Laser-assisted processing of Ni-Al-Co-Ti under high pressure. *Mater. Manuf. Process.* **2017**, *32*, 1606–1611. [[CrossRef](#)]
170. Ross, M.; Boehler, R.; Söderlind, P. Xenon Melting Curve to 80 GPa and *5p-d* Hybridization. *Phys. Rev. Lett.* **2005**, *95*, 257801. [[CrossRef](#)]
171. Runge, C.E.; Kubo, A.; Kiefer, B.; Meng, Y.; Prakapenka, V.B.; Shen, G.; Cava, R.J.; Duffy, T.S. Equation of state of MgGeO<sub>3</sub> perovskite to 65 GPa: Comparison with the post-perovskite phase. *Phys. Chem. Miner.* **2006**, *33*, 699–709. [[CrossRef](#)]
172. Sadovyi, B.; Wierzbowska, M.; Stelmakh, S.; Boccato, S.; Gierlotka, S.; Irifune, T.; Porowski, S.; Grzegory, I. Experimental and theoretical evidence of the temperature-induced wurtzite to rocksalt phase transition in GaN under high pressure. *Phys. Rev. B Condens. Matter* **2020**, *102*, 235109. [[CrossRef](#)]
173. Saha, P.; Mukherjee, G.D. Temperature measurement in double-sided laser-heated diamond anvil cell and reaction of carbon. *Indian J. Phys.* **2021**, *95*, 621–628. [[CrossRef](#)]
174. Saha, P.; Mazumder, A.; Mukherjee, G.D. Thermal conductivity of dense hcp iron: Direct measurements using laser heated diamond anvil cell. *Geosci. Front.* **2020**, *11*, 1755–1761. [[CrossRef](#)]
175. Salem, R.; Matityahu, S.; Melchior, A.; Nikolaevsky, M.; Noked, O.; Sterer, E. Image analysis of speckle patterns as a probe of melting transitions in laser-heated diamond anvil cell experiments. *Rev. Sci. Instrum.* **2015**, *86*, 093907. [[CrossRef](#)]
176. Santamaría-Pérez, D.; Ross, M.; Errandonea, D.; Mukherjee, G.D.; Mezouar, M.; Boehler, R. X-ray diffraction measurements of Mo melting to 119 GPa and the high pressure phase diagram. *J. Chem. Phys.* **2009**, *130*, 124509. [[CrossRef](#)]
177. Saxena, S.K.; Dubrovinsky, L.S.; Häggkvist, P.; Cerenius, Y.; Shen, G.; Mao, H.K. Synchrotron X-Ray Study of Iron at High Pressure and Temperature. *Science* **1995**, *269*, 1703–1704. [[CrossRef](#)]
178. Schultz, E.; Mezouar, M.; Crichton, W.; Bauchau, S.; Blattmann, G.; Andraut, D.; Fiquet, G.; Boehler, R.; Rambert, N.; Sitaud, B.; et al. Double-sided laser heating system for *in situ* high pressure–high temperature monochromatic X-ray diffraction at the esrf. *High Press. Res.* **2005**, *25*, 71–83. [[CrossRef](#)]
179. Shen, G.; Mao, H.-K.; Hemley, R.J.; Duffy, T.S.; Rivers, M.L. Melting and crystal structure of iron at high pressures and temperatures. *Geophys. Res. Lett.* **1998**, *25*, 373–376. [[CrossRef](#)]

180. Shen, G.; Rivers, M.L.; Wang, Y.; Sutton, S.R. Laser heated diamond cell system at the Advanced Photon Source for in situ X-ray measurements at high pressure and temperature. *Rev. Sci. Instrum.* **2001**, *72*, 1273–1282. [[CrossRef](#)]
181. Shen, G.; Prakapenka, V.B.; Rivers, M.L.; Sutton, S.R. Structure of Liquid Iron at Pressures up to 58 GPa. *Phys. Rev. Lett.* **2004**, *92*, 185701. [[CrossRef](#)]
182. Shen, G.; Mao, H.-k.; Hemley, R. Laser-Heated Diamond Anvil Cell Technique: Double-Sided Heating with Multimode Nd:YAG Laser. In *Advanced Materials '96 New Trends in High Pressure Research*; Akaishi, M., Ed.; The Institute: Tsukuba, Japan, 1996.
183. Shieh, S.R.; Duffy, T.S.; Shen, G. X-ray diffraction study of phase stability in SiO<sub>2</sub> at deep mantle conditions. *Earth Planet. Sci. Lett.* **2005**, *235*, 273–282. [[CrossRef](#)]
184. Singh, A.K.; Andrault, D.; Bouvier, P. X-ray diffraction from stishovite under nonhydrostatic compression to 70GPa: Strength and elasticity across the tetragonal→orthorhombic transition. *Phys. Earth Planet. Inter.* **2012**, *208–209*, 1–10. [[CrossRef](#)]
185. Sinmyo, R.; Hirose, K. The Soret diffusion in laser-heated diamond-anvil cell. *Phys. Earth Planet. Inter.* **2010**, *180*, 172–178. [[CrossRef](#)]
186. Sinmyo, R.; Pesce, G.; Greenberg, E.; McCammon, C.; Dubrovinsky, L. Lower mantle electrical conductivity based on measurements of Al, Fe-bearing perovskite under lower mantle conditions. *Earth Planet. Sci. Lett.* **2014**, *393*, 165–172. [[CrossRef](#)]
187. Spiekermann, G.; Kuppenko, I.; Petitgirard, S.; Harder, M.; Nyrow, A.; Weis, C.; Albers, C.; Biedermann, N.; Libon, L.; Sahle, C.J.; et al. A portable on-axis laser-heating system for near-90degrees X-ray spectroscopy: Application to ferropericlase and iron silicide. *J. Synchrotron Radiat.* **2020**, *27*, 414–424. [[CrossRef](#)] [[PubMed](#)]
188. Stutzmann, V.; Dewaele, A.; Bouchet, J.; Bottin, F.; Mezouar, M. High-pressure melting curve of titanium. *Phys. Rev. B Condens. Matter.* **2015**, *92*, 224110. [[CrossRef](#)]
189. Auzende, A.-L.; Gillot, J.; Coquet, A.; Hennet, L.; Ona-Nguema, G.; Bonnin, D.; Esteve, I.; Roskosz, M.; Fiquet, G. Synthesis of amorphous MgO-rich peridotitic starting material for laser-heated diamond anvil cell experiments—Application to iron partitioning in the mantle. *High Press. Res.* **2011**, *31*, 199–213. [[CrossRef](#)]
190. Tateno, S.; Hirose, K.; Ohishi, Y.; Tatsumi, Y. The Structure of Iron in Earth's Inner Core. *Science* **2010**, *330*, 359–361. [[CrossRef](#)]
191. Watanuki, T.; Shimomura, O.; Yagi, T.; Kondo, T.; Isshiki, M. Construction of laser-heated diamond anvil cell system for in situ x-ray diffraction study at SPring-8. *Rev. Sci. Instrum.* **2001**, *72*, 1289–1292. [[CrossRef](#)]
192. Weck, G.; Recoules, V.; Queyroux, J.-A.; Datchi, F.; Bouchet, J.; Ninet, S.; Garbarino, G.; Mezouar, M.; Loubeyre, P. Determination of the melting curve of gold up to 110 GPa. *Phys. Rev. B Condens. Matter.* **2020**, *101*, 014106. [[CrossRef](#)]
193. Yagi, T.; Susaki, J.-I. A Laser Heating System for Diamond Anvil Using CO<sub>2</sub>. In *High-Pressure Research: Application to Earth and Planetary Sciences*; Terra Scientific Publishing Company: Tokyo, Japan, 1992; pp. 51–54.
194. Yang, L.; Karandikar, A.; Boehler, R. Flash heating in the diamond cell: Melting curve of rhenium. *Rev. Sci. Instrum.* **2012**, *83*, 063905. [[CrossRef](#)] [[PubMed](#)]
195. Yoo, C.S.; Akella, J.; Moriarty, J.A. High-pressure melting temperatures of uranium: Laser-heating experiments and theoretical calculations. *Phys. Rev. B Condens. Matter.* **1993**, *48*, 15529–15534. [[CrossRef](#)] [[PubMed](#)]
196. Yoo, C.S.; Akella, J.; Campbell, A.J.; Mao, H.K.; Hemley, R.J. Phase Diagram of Iron by in Situ X-ray Diffraction: Implications for Earth's Core. *Science* **1995**, *270*, 1473–1475. [[CrossRef](#)]
197. Yoo, C.S.; Söderlind, P.; Moriarty, J.A.; Cambell, A.J. dhcp as a possible new e' phase of iron at high pressures and temperatures. *Phys. Lett. A* **1996**, *214*, 65–70. [[CrossRef](#)]
198. Yusa, H.; Takemura, K.; Matsui, Y.; Morishima, H.; Watanabe, K.; Yamawaki, H.; Aoki, K. Direct transformation of graphite to cubic diamond observed in a laser-heated diamond anvil cell. *Appl. Phys. Lett.* **1998**, *72*, 1843–1845. [[CrossRef](#)]
199. Zerr, A.; Boehler, R. Melting of (Mg, Fe)SiO<sub>3</sub>-Perovskite to 625 Kilobars: Indication of a High Melting Temperature in the Lower Mantle. *Science* **1993**, *262*, 553–555. [[CrossRef](#)]
200. Zerr, A.; Miehe, G.; Serghiou, G.; Schwarz, M.; Kroke, E.; Riedel, R.; Fueß, H.; Kroll, P.; Boehler, R. Synthesis of cubic silicon nitride. *Nature* **1999**, *400*, 340–342. [[CrossRef](#)]
201. Zhang, L.; Meng, Y.; Mao, H.-k. Unit cell determination of coexisting post-perovskite and H-phase in (Mg,Fe)SiO<sub>3</sub> using multigrain XRD: Compositional variation across a laser heating spot at 119 GPa. *Prog. Earth Planet. Sci.* **2016**, *3*, 13. [[CrossRef](#)]
202. Zhang, D.; Jackson, J.M.; Zhao, J.; Sturhahn, W.; Alp, E.E.; Hu, M.Y.; Toellner, T.S.; Murphy, C.A.; Prakapenka, V.B. Temperature of Earth's core constrained from melting of Fe and Fe<sub>0.9</sub>Ni<sub>0.1</sub> at high pressures. *Earth Planet. Sci. Lett.* **2016**, *447*, 72–83. [[CrossRef](#)]
203. Zinin, P.V.; Prakapenka, V.B.; Burgess, K.; Odake, S.; Chigarev, N.; Sharma, S.K. Combined laser ultrasonics, laser heating, and Raman scattering in diamond anvil cell system. *Rev. Sci. Instrum.* **2016**, *87*, 123908. [[CrossRef](#)] [[PubMed](#)]
204. Zou, G.; Ma, Y.; Mao, H.-K.; Hemley, R.J.; Gramsch, S.A. A diamond gasket for the laser-heated diamond anvil cell. *Rev. Sci. Instrum.* **2001**, *72*, 1298–1301. [[CrossRef](#)]
205. Weathers, M.S.; Bassett, W.A. Melting of carbon at 50 to 300 kbar. *Phys. Chem. Miner.* **1987**, *15*, 105–112. [[CrossRef](#)]
206. Huang, D.; Siebert, J.; Badro, J. High pressure partitioning behavior of Mo and W and late sulfur delivery during Earth's core formation. *Geochim. Cosmochim. Acta* **2021**, *310*, 19–31. [[CrossRef](#)]
207. Kurnosov, A.; Marquardt, H.; Dubrovinsky, L.; Potapkin, V. A waveguide-based flexible CO<sub>2</sub>-laser heating system for diamond-anvil cell applications. *C.R. Geosci.* **2019**, *351*, 280–285. [[CrossRef](#)]
208. Chidester, B.A.; Thompson, E.C.; Fischer, R.A.; Heinz, D.L.; Prakapenka, V.B.; Meng, Y.; Campbell, A.J. Experimental thermal equation of state of B2–KCl. *Phys. Rev. B Condens. Matter.* **2021**, *104*, 094107. [[CrossRef](#)]

209. Zhang, Y.; Tan, Y.; Geng, H.Y.; Salke, N.P.; Gao, Z.; Li, J.; Sekine, T.; Wang, Q.; Greenberg, E.; Prakapenka, V.B.; et al. Melting curve of vanadium up to 256 GPa: Consistency between experiments and theory. *Phys. Rev. B Condens. Matter.* **2020**, *102*, 214104. [[CrossRef](#)]
210. Gaida, N.A.; Niwa, K.; Sasaki, T.; Hasegawa, M. Phase relations and thermoelasticity of magnesium silicide at high pressure and temperature. *J. Chem. Phys.* **2021**, *154*, 144701. [[CrossRef](#)]
211. Anzellini, S.; Burakovskiy, L.; Turnbull, R.; Bandiello, E.; Errandonea, D. P–V–T Equation of State of Iridium Up to 80 GPa and 3100 K. *Crystals* **2021**, *11*, 452. [[CrossRef](#)]
212. Liu, L.-g. Silicate perovskite from phase transformations of pyrope-garnet at high pressure and temperature. *Geophys. Res. Lett.* **1974**, *1*, 277–280. [[CrossRef](#)]
213. Nishiyama, N.; Langer, J.; Sakai, T.; Kojima, Y.; Holzheid, A.; Gaida, N.A.; Kulik, E.; Hirao, N.; Kawaguchi, S.I.; Irifune, T.; et al. Phase relations in silicon and germanium nitrides up to 98 GPa and 2400 °C. *J. Am. Ceram. Soc.* **2019**, *102*, 2195–2202. [[CrossRef](#)]
214. Bassett, W.A.; Li-Chung, M. Disproportionation of Fe<sub>2</sub>SiO<sub>4</sub> to 2FeO+SiO<sub>2</sub> at pressures up to 250kbar and temperatures up to 3000 °C. *Phys. Earth Planet. Inter.* **1972**, *6*, 154–160. [[CrossRef](#)]
215. Kavner, A.; Jeanloz, R. The high-pressure melting curve of Allende meteorite. *Geophys. Res. Lett.* **1998**, *25*, 4161–4164. [[CrossRef](#)]
216. Boehler, R.; von Bagen, N.; Chopelas, A. Melting, thermal expansion, and phase transitions of iron at high pressures. *J. Geophys. Res. Solid Earth* **1990**, *95*, 21731–21736. [[CrossRef](#)]
217. Wakamatsu, T.; Ohta, K.; Yagi, T.; Hirose, K.; Ohishi, Y. Measurements of sound velocity in iron–nickel alloys by femtosecond laser pulses in a diamond anvil cell. *Phys. Chem. Miner.* **2018**, *45*, 589–595. [[CrossRef](#)]
218. Deemyad, S.; Sterer, E.; Barthel, C.; Rekhi, S.; Tempere, J.; Silvera, I.F. Pulsed laser heating and temperature determination in a diamond anvil cell. *Rev. Sci. Instrum.* **2005**, *76*, 125104. [[CrossRef](#)]
219. Deemyad, S.; Silvera, I.F. Melting Line of Hydrogen at High Pressures. *Phys. Rev. Lett.* **2008**, *100*, 155701. [[CrossRef](#)]
220. Eremets, M.I.; Gavriluk, A.G.; Trojan, I.A.; Dzivenko, D.A.; Boehler, R. Single-bonded cubic form of nitrogen. *Nat. Mater.* **2004**, *3*, 558–563. [[CrossRef](#)]
221. Brygoo, S.; Loubeyre, P.; Millot, M.; Rygg, J.R.; Celliers, P.M.; Eggert, J.H.; Jeanloz, R.; Collins, G.W. Evidence of hydrogen–helium immiscibility at Jupiter-interior conditions. *Nature* **2021**, *593*, 517–521. [[CrossRef](#)] [[PubMed](#)]
222. Nissim, N.; Eliezer, S.; Werdiger, M. The sound velocity throughout the P–ρ phase-space with application to laser induced shock wave in matter precompressed by a diamond anvil cell. *J. Appl. Phys.* **2014**, *115*, 213503. [[CrossRef](#)]
223. Brygoo, S.; Millot, M.; Loubeyre, P.; Lazicki, A.E.; Hamel, S.; Qi, T.; Celliers, P.M.; Coppari, F.; Eggert, J.H.; Fratanduono, D.E.; et al. Analysis of laser shock experiments on precompressed samples using a quartz reference and application to warm dense hydrogen and helium. *J. Appl. Phys.* **2015**, *118*, 195901. [[CrossRef](#)]
224. Loubeyre, P.; Celliers, P.M.; Hicks, D.G.; Henry, E.; Dewaele, A.; Pasley, J.; Eggert, J.; Koenig, M.; Occelli, F.; Lee, K.M.; et al. Coupling static and dynamic compressions: First measurements in dense hydrogen. *High Press. Res.* **2004**, *24*, 25–31. [[CrossRef](#)]
225. Loubeyre, P.; Brygoo, S.; Eggert, J.; Celliers, P.M.; Spaulding, D.K.; Rygg, J.R.; Boehly, T.R.; Collins, G.W.; Jeanloz, R. Extended data set for the equation of state of warm dense hydrogen isotopes. *Phys. Rev. B Condens. Matter.* **2012**, *86*, 144115. [[CrossRef](#)]
226. Nissim, N.; Eliezer, S.; Werdiger, M.; Perelmutter, L. Approaching the “cold curve” in laser-driven shock wave experiment of a matter precompressed by a partially perforated diamond anvil. *Laser Part. Beams* **2013**, *31*, 73–79. [[CrossRef](#)]
227. Coppari, F.; Smith, R.F.; Eggert, J.H.; Wang, J.; Rygg, J.R.; Lazicki, A.; Hawreliak, J.A.; Collins, G.W.; Duffy, T.S. Experimental evidence for a phase transition in magnesium oxide at exoplanet pressures. *Nat. Geosci.* **2013**, *6*, 926–929. [[CrossRef](#)]
228. Vance, S.; Hammeijer, J.; Kimura, J.; Hussmann, H.; deMartin, B.; Brown, J.M. Hydrothermal Systems in Small Ocean Planets. *Astrobiology* **2007**, *7*, 987–1005. [[CrossRef](#)]
229. Helled, R.; Anderson, J.D.; Podolak, M.; Schubert, G. Interior Models of Uranus and Neptune. *Astrophys. J.* **2010**, *726*, 15. [[CrossRef](#)]
230. Faure, G.; Mensing, T. *Introduction to Planetary Science*; Springer: Berlin/Heidelberg, Germany, 2007.
231. Guillot, T.; Gautier, D. 10.13—Giant Planets. In *Treatise on Geophysics*; Schubert, G., Ed.; Elsevier: Amsterdam, The Netherlands, 2007; pp. 439–464.
232. Walker, D.; Lord, O.T.; Walter, M.J.; Clark, S.M. X-ray absorption contrast images of binary chemical reactions. *Chem. Geol.* **2009**, *260*, 211–220. [[CrossRef](#)]
233. Ladlow, M.; Legge, C.H.; Neudeck, T.; Pipe, A.J.; Sheppard, T.; Yang, L.L. Wavelength dependent photo-controlled differential release of compounds from solid phase resin. *Chem. Commun.* **2003**, 2048–2049. [[CrossRef](#)] [[PubMed](#)]
234. Sarkar, S.K. Lasers in Materials Processing and Synthesis. In *Handbook on Synthesis Strategies for Advanced Materials: Volume-II: Processing and Functionalization of Materials*; Tyagi, A.K., Ningthoujam, R.S., Eds.; Springer Nature Singapore: Singapore, 2022; pp. 791–831.
235. Andrei, F.; Tiliakos, A.; Scarisoreanu, M.; Scarisoreanu, N.D. Advanced Laser Methods for Synthesizing Photocatalysts. In *Green Photocatalytic Semiconductors: Recent Advances and Applications*; Garg, S., Chandra, A., Eds.; Springer International Publishing: Cham, Switzerland, 2022; pp. 399–444.
236. Theerthagiri, J.; Karuppasamy, K.; Lee, S.J.; Shwetharani, R.; Kim, H.-S.; Pasha, S.K.K.; Ashokkumar, M.; Choi, M.Y. Fundamentals and comprehensive insights on pulsed laser synthesis of advanced materials for diverse photo- and electrocatalytic applications. *Light Sci. Appl.* **2022**, *11*, 250. [[CrossRef](#)]

237. Yusa, H. Laser-heated diamond anvil cell system for photochemical reaction measurements. *Rev. Sci. Instrum.* **2001**, *72*, 1309. [[CrossRef](#)]
238. Ishida, Y.; Iwasaki, N.; Asaumi, K.; Yajima, T.; Maruyama, Y. Tunable picosecond pulses from a short-cavity dye laser under ultra-high pressure using diamond-anvil cell. *Appl. Phys. B* **1985**, *38*, 159–163. [[CrossRef](#)]
239. Mao, H.K.; Bell, P.M.; Shaner, J.W.; Steinberg, D.J. Specific volume measurements of Cu, Mo, Pd, and Ag and calibration of the ruby R<sub>1</sub> fluorescence pressure gauge from 0.06 to 1 Mbar. *J. Appl. Phys.* **1978**, *49*, 3276–3283. [[CrossRef](#)]
240. Bassett, W.A. The birth and development of laser heating in diamond anvil cells. *Rev. Sci. Instrum.* **2001**, *72*, 1270–1272. [[CrossRef](#)]
241. Hernandez, H. *Collision Energy between Maxwell-Boltzmann Molecules: An Alternative Derivation of Arrhenius Equation*. *ForsChem Res.* **2019**. [[CrossRef](#)]
242. Akhtar, M. Synthesis and fundamental property studies of energy material under high pressure. Ph.D. Thesis, University of Louisville, Louisville, KY, USA, 2017.
243. Spooner, J.; Wiebe, H.; Louwse, M.; Reader, B.; Weinberg, N. Theoretical analysis of high-pressure effects on conformational equilibria. *Can. J. Chem.* **2018**, *96*, 178–189. [[CrossRef](#)]
244. Daviau, K.; Meng, Y.; Lee, K.K.M. SiO<sub>2</sub>-SiC Mixtures at High Pressures and Temperatures: Implications for Planetary Bodies Containing SiC. *J. Geophys. Res. Planets* **2019**, *124*, 2294–2305. [[CrossRef](#)]
245. Arora, A.K.; Sakuntala, T. Decomposition of binary sulphate KHSO<sub>4</sub> at high pressure. *High Press. Res.* **2000**, *17*, 1–11. [[CrossRef](#)]
246. Kuznetsov, A.Y.; Pereira, A.S.; Shiryaev, A.A.; Haines, J.; Dubrovinsky, L.; Dmitriev, V.; Pattison, P.; Guignot, N. Pressure-Induced Chemical Decomposition and Structural Changes of Boric Acid. *J. Phys. Chem. A* **2006**, *110*, 13858–13865. [[CrossRef](#)]
247. Greaves, R.J.; Schlecht, K.D. Gibbs free energy: The criteria for spontaneity. *J. Chem. Educ.* **1992**, *69*, 417. [[CrossRef](#)]
248. Demazeau, G. High Pressure and Chemical Bonding in Materials Chemistry. *Z. Naturforsch. B* **2006**, *61*, 799–807. [[CrossRef](#)]
249. Cai, W.; Katrusiak, A. Giant negative linear compression positively coupled to massive thermal expansion in a metal–organic framework. *Nat. Commun.* **2014**, *5*, 4337. [[CrossRef](#)] [[PubMed](#)]
250. Subramanian, N.; Shekar, N.V.C.; Kumar, N.R.S.; Sahu, P.C. Development of laser-heated diamond anvil cell facility for synthesis of novel materials. *Curr. Sci.* **2006**, *91*, 175–182.
251. Shekar, N.V.C.; Takemura, K.; Yusa, H. Synthesis experiments on in-Sb and B-Sb systems in a laser heated diamond-anvil cell. *High Press. Res.* **1997**, *15*, 393–398. [[CrossRef](#)]
252. Kadobayashi, H.; Ohnishi, S.; Ohfuji, H.; Yamamoto, Y.; Muraoka, M.; Yoshida, S.; Hirao, N.; Kawaguchi-Imada, S.; Hirai, H. Diamond formation from methane hydrate under the internal conditions of giant icy planets. *Sci. Rep.* **2021**, *11*, 8165. [[CrossRef](#)]
253. Vyazovkin, S.; Wight, C.A. Kinetics In Solids. *Annu. Rev. Phys. Chem.* **1997**, *48*, 125–149. [[CrossRef](#)]
254. Vyazovkin, S. Kinetic effects of pressure on decomposition of solids. *Int. Rev. Phys. Chem.* **2020**, *39*, 35–66. [[CrossRef](#)]
255. Arrhenius, S. Über die Reaktionsgeschwindigkeit bei der Inversion von Rohrzucker durch Säuren. *Z. Phys. Chem.* **1889**, *4U*, 226–248. [[CrossRef](#)]
256. Laidler, K.J.; King, M.C. Development of transition-state theory. *J. Phys. Chem.* **1983**, *87*, 2657–2664. [[CrossRef](#)]
257. Haring, M.M. The Theory of Rate Processes (Glasstone, Samuel; Laidler, Keith J.; Eyring, Henry). *J. Chem. Educ.* **1942**, *19*, 249. [[CrossRef](#)]
258. Eyring, H. The Activated Complex in Chemical Reactions. *J. Chem. Phys.* **1935**, *3*, 107–115. [[CrossRef](#)]
259. Asano, T.; Le Noble, W.J. Activation and reaction volumes in solution. *Chem. Rev.* **1978**, *78*, 407–489. [[CrossRef](#)]
260. Kornilov, D.A.; Kiselev, V.D. Activation and Reaction Volumes and Their Correlations with the Entropy and Enthalpy Parameters. *J. Chem. Eng. Data* **2015**, *60*, 3571–3580. [[CrossRef](#)]
261. Brosh, E.; Shneck, R.Z.; Makov, G. Explicit Gibbs free energy equation of state for solids. *J. Phys. Chem. Solids* **2008**, *69*, 1912–1922. [[CrossRef](#)]
262. Lin, W.; Murphy, C.J. A Demonstration of Le Chatelier’s Principle on the Nanoscale. *ACS Cent. Sci.* **2017**, *3*, 1096–1102. [[CrossRef](#)] [[PubMed](#)]
263. Le Chatelier, H. *Recherches Expérimentales et Théoriques sur les Équilibres Chimiques*; Dunod: Malakoff, France, 1888.
264. Laidler, K.J. *Chemical kinetics*, 3rd ed.; Harper Collins: New York, NY, USA, 1987.
265. Kyaw, K.; Kubota, M.; Watanabe, F.; Matsuda, H.; Hasatani, M. Study of Carbonation of CaO for High Temperature Thermal Energy Storage. *J. Chem. Eng. Jpn.* **1998**, *31*, 281–284. [[CrossRef](#)]
266. Benton, A.F.; Drake, L.C. Kinetics of Reaction and Adsorption in the System Silver—Oxygen. *J. Am. Chem. Soc.* **1934**, *56*, 255–263. [[CrossRef](#)]
267. Liavitskaya, T.; Vyazovkin, S. Delving into the Kinetics of Reversible Thermal Decomposition of Solids Measured on Heating and Cooling. *J. Phys. Chem. C* **2017**, *121*, 15392–15401. [[CrossRef](#)]
268. Laniel, D.; Bykov, M.; Fedotenko, T.; Ponomareva, A.V.; Abrikosov, I.A.; Glazyrin, K.; Svitlyk, V.; Dubrovinsky, L.; Dubrovinskaia, N. High Pressure Investigation of the S–N<sub>2</sub> System up to the Megabar Range: Synthesis and Characterization of the SN<sub>2</sub> Solid. *Inorg. Chem.* **2019**, *58*, 9195–9204. [[CrossRef](#)] [[PubMed](#)]
269. Mattesini, M.; de Almeida, J.S.; Dubrovinsky, L.; Dubrovinskaia, N.; Johansson, B.; Ahuja, R. High-pressure and high-temperature synthesis of the cubic TiO<sub>2</sub> polymorph. *Phys. Rev. B* **2004**, *70*, 212101. [[CrossRef](#)]
270. Lobanov, S.S.; Zhu, Q.; Holtgrewe, N.; Prescher, C.; Prakapenka, V.B.; Oganov, A.R.; Goncharov, A.F. Stable magnesium peroxide at high pressure. *Sci. Rep.* **2015**, *5*, 13582. [[CrossRef](#)] [[PubMed](#)]

271. Zhang, W.; Oganov, A.R.; Zhu, Q.; Lobanov, S.S.; Stavrou, E.; Goncharov, A.F. Stability of numerous novel potassium chlorides at high pressure. *Sci. Rep.* **2016**, *6*, 26265. [[CrossRef](#)] [[PubMed](#)]
272. Gurlo, A.; Dzivenko, D.; Kroll, P.; Riedel, R. High-pressure high-temperature synthesis of Rh<sub>2</sub>O<sub>3</sub>-II-type In<sub>2</sub>O<sub>3</sub> polymorph. *Phys. Stat. Sol.* **2008**, *2*, 269–271. [[CrossRef](#)]
273. Soignard, E.; Machon, D.; McMillan, P.F.; Dong, J.; Xu, B.; Leinenweber, K. Spinel-Structured Gallium Oxynitride (Ga<sub>3</sub>O<sub>3</sub>N) Synthesis and Characterization: An Experimental and Theoretical Study. *Chem. Mater.* **2005**, *17*, 5465–5472. [[CrossRef](#)]
274. Clarke, S.M.; Amsler, M.; Walsh, J.P.S.; Yu, T.; Wang, Y.; Meng, Y.; Jacobsen, S.D.; Wolverton, C.; Freedman, D.E. Creating Binary Cu–Bi Compounds via High-Pressure Synthesis: A Combined Experimental and Theoretical Study. *Chem. Mater.* **2017**, *29*, 5276–5285. [[CrossRef](#)]
275. Yadav, R.R.; Kumar, L.K. One-dimensional spatially dependent solute transport in semi-infinite porous media: An analytical solution. *Int. J. Eng. Sci. Technol.* **2017**, *9*, 20–27. [[CrossRef](#)]
276. Jacob, A.C.; Zeidler, M.D. Self-diffusion in binary mixtures: The system benzene/cyclohexane at high pressures. *Phys. Chem. Chem. Phys.* **2003**, *5*, 538–542. [[CrossRef](#)]
277. Noguchi, N.; Okuchi, T. Self-diffusion of protons in H<sub>2</sub>O ice VII at high pressures: Anomaly around 10 GPa. *J. Chem. Phys.* **2016**, *144*, 234503. [[CrossRef](#)]
278. Smoluchowski, M.V. Zur kinetischen Theorie der Transpiration und Diffusion verdünnter Gase. *Ann. Phys.* **1910**, *338*, 1559–1570. [[CrossRef](#)]
279. Herrero, M.A.; Rodrigo, M. A note on Smoluchowski's equations with diffusion. *Appl. Math. Lett.* **2005**, *18*, 969–975. [[CrossRef](#)]
280. Calef, D.F.; Deutch, J.M. Diffusion-Controlled Reactions. *Annu. Rev. Phys. Chem.* **1983**, *34*, 493–524. [[CrossRef](#)]
281. Ehrlich, D.J.; Tsao, J.Y.; Tsao, J.Y. *Laser Microfabrication: Thin Film Processes and Lithography*; Elsevier Science: Amsterdam, The Netherlands, 1989.
282. Maxwell, J.L.; Webb, N.; Bradshaw, D.; Black, M.R.; Maskaly, K.; Chavez, C.A.; Espinoza, M.; Vessard, S.; Art, B.; Johnson, S.; et al. On “how to start a fire”, or transverse forced-convection, hyperbaric laser chemical vapor deposition of fibers and textiles. *Text. Res. J.* **2014**, *84*, 1976–1986. [[CrossRef](#)]
283. Wang, R.; Chen, W.; Zhang, L.; Liu, D.; Li, X.; Du, Y.; Jin, Z. Diffusivities and atomic mobilities in the Al–Ce–Ni melts. *J. Non-Cryst. Solids* **2013**, *379*, 201–207. [[CrossRef](#)]
284. Sekido, N.; Hoshino, A.; Fukuzaki, M.; Maruko, T.; Yamabe-Mitarai, Y. Interdiffusion in the Ir-Rich Solid Solutions of Ir–Pt, Ir–Rh, and Ir–Re Binary Alloys. *J. Ph. Equilibria Diffus.* **2011**, *32*, 219–225. [[CrossRef](#)]
285. Liu, Z.; Emami-Meybodi, H. Apparent diffusion coefficient for adsorption-controlled gas transport in nanoporous media. *Chem. Eng. J.* **2022**, *450*, 138105. [[CrossRef](#)]
286. Nachtrieb, N.H.; Resing, H.A.; Rice, S.A. Effect of Pressure on Self-Diffusion in Lead. *J. Chem. Phys.* **1959**, *31*, 135–138. [[CrossRef](#)]
287. Jamieson, J.C.; Lawson, A.W.; Nachtrieb, N.D. New Device for Obtaining X-Ray Diffraction Patterns from Substances Exposed to High Pressure. *Rev. Sci. Instrum.* **1959**, *30*, 1016–1019. [[CrossRef](#)]
288. Gréaux, S.; Gautron, L.; Andraut, D.; Bolfan-Casanova, N.; Guignot, N.; Bouhifd, M.A. Experimental high pressure and high temperature study of the incorporation of uranium in Al-rich CaSiO<sub>3</sub> perovskite. *Phys. Earth Planet. Inter.* **2009**, *174*, 254–263. [[CrossRef](#)]
289. Toki, T.; Bellan, J. Investigation of species-mass diffusion in binary-species boundary layers at high pressure using direct numerical simulations. *J. Fluid Mech.* **2021**, *928*, A18. [[CrossRef](#)]
290. Alexandrov, D.V.; Galenko, P.K. Selected mode for rapidly growing needle-like dendrite controlled by heat and mass transport. *Acta Mater.* **2017**, *137*, 64–70. [[CrossRef](#)]
291. Gomez-Perez, N.; Rodriguez, J.F.; McWilliams, R.S. Finite element modeling of melting and fluid flow in the laser-heated diamond-anvil cell. *J. Appl. Phys.* **2017**, *121*, 145904. [[CrossRef](#)]
292. Lu, G.Q.; Nygren, E.; Aziz, M.J. Pressure-enhanced crystallization kinetics of amorphous Si and Ge: Implications for point-defect mechanisms. *J. Appl. Phys.* **1991**, *70*, 5323–5345. [[CrossRef](#)]
293. Kolasinski, K.W. Catalytic growth of nanowires: Vapor–liquid–solid, vapor–solid–solid, solution–liquid–solid and solid–liquid–solid growth. *Curr. Opin. Solid State Mater. Sci.* **2006**, *10*, 182–191. [[CrossRef](#)]
294. Sarjeant, P.T.; Roy, R. New Glassy and Polymorphic Oxide Phases Using Rapid Quenching Techniques. *J. Am. Ceram. Soc.* **1967**, *50*, 500–503. [[CrossRef](#)]
295. Steeb, S. *Rapidly Quenched Metals*. Elsevier Science: Amsterdam, The Netherlands, 2012.
296. Goarant, F.; Guyot, F.; Peyronneau, J.; Poirier, J.-P. High-pressure and high-temperature reactions between silicates and liquid iron alloys, in the diamond anvil cell, studied by analytical electron microscopy. *J. Geophys. Res. Solid Earth* **1992**, *97*, 4477–4487. [[CrossRef](#)]
297. Kobayashi, A.; Steinberg, M. *The Thermal Decomposition of Methane in a Tubular Reactor*; UD Department of Energy: Washington, DC, USA, 1992; 20p.
298. Ashcroft, N.W. Metallic Hydrogen: A High-Temperature Superconductor? *Phys. Rev. Lett.* **1968**, *21*, 1748–1749. [[CrossRef](#)]
299. Liu, H.; Naumov, I.I.; Hoffmann, R.; Ashcroft, N.W.; Hemley, R.J. Potential high-*T<sub>c</sub>* superconducting lanthanum and yttrium hydrides at high pressure. *Proc. Natl. Acad. Sci. USA* **2017**, *114*, 6990–6995. [[CrossRef](#)] [[PubMed](#)]
300. Ashcroft, N.W. Hydrogen Dominant Metallic Alloys: High Temperature Superconductors? *Phys. Rev. Lett.* **2004**, *92*, 187002. [[CrossRef](#)] [[PubMed](#)]

301. Simons Collaboration on the Many Electron Problem; Motta, M.; Genovese, C.; Ma, F.; Cui, Z.-H.; Sawaya, R.; Chan, G.K.-L.; Chepiga, N.; Helms, P.; Jiménez-Hoyos, C.; et al. Ground-State Properties of the Hydrogen Chain: Dimerization, Insulator-to-Metal Transition, and Magnetic Phases. *Phys. Rev. X* **2020**, *10*, 031058. [[CrossRef](#)]
302. Salke, N.P.; Davari Esfahani, M.M.; Zhang, Y.; Kruglov, I.A.; Zhou, J.; Wang, Y.; Greenberg, E.; Prakapenka, V.B.; Liu, J.; Oganov, A.R.; et al. Synthesis of clathrate cerium superhydride CeH<sub>9</sub> at 80–100 GPa with atomic hydrogen sublattice. *Nat. Commun.* **2019**, *10*, 4453. [[CrossRef](#)] [[PubMed](#)]
303. Struzhkin, V.V.; Kim, D.Y.; Stavrou, E.; Muramatsu, T.; Mao, H.-k.; Pickard, C.J.; Needs, R.J.; Prakapenka, V.B.; Goncharov, A.F. Synthesis of sodium polyhydrides at high pressures. *Nat. Commun.* **2016**, *7*, 12267. [[CrossRef](#)] [[PubMed](#)]
304. Zhou, D.; Semenok, D.V.; Duan, D.; Xie, H.; Chen, W.; Huang, X.; Li, X.; Liu, B.; Oganov, A.R.; Cui, T. Superconducting praseodymium superhydrides. *Sci. Adv.* **2020**, *6*, eaax6849. [[CrossRef](#)] [[PubMed](#)]
305. Winkler, B.; Juarez-Arellano, E.A.; Friedrich, A.; Bayarjargal, L.; Schröder, F.; Biehler, J.; Milman, V.; Clark, S.M.; Yan, J. In situ synchrotron X-ray diffraction study of the formation of TaB<sub>2</sub> from the elements in a laser heated diamond anvil cell. *Solid State Sci.* **2010**, *12*, 2059–2064. [[CrossRef](#)]
306. Juarez-Arellano, E.A.; Winkler, B.; Friedrich, A.; Bayarjargal, L.; Morgenroth, W.; Kunz, M.; Milman, V. In situ study of the formation of rhenium borides from the elements at high-(p, T) conditions: Extreme incompressibility of Re<sub>7</sub>B<sub>3</sub> and formation of new phases. *Solid State Sci.* **2013**, *25*, 85–92. [[CrossRef](#)]
307. Bykova, E.; Ovsyannikov, S.V.; Bykov, M.; Yin, Y.; Fedotenko, T.; Holz, H.; Gabel, S.; Merle, B.; Chariton, S.; Prakapenka, V.B.; et al. Synthesis, crystal structure, and properties of stoichiometric hard tungsten tetraboride, WB. *J. Mater. Chem. A* **2022**, *10*, 20111–20120. [[CrossRef](#)]
308. Juarez-Arellano, E.A.; Winkler, B.; Bayarjargal, L.; Friedrich, A.; Milman, V.; Kammler, D.R.; Clark, S.M.; Yan, J.; Koch-Müller, M.; Schröder, F.; et al. Formation of scandium carbides and scandium oxycarbide from the elements at high-(P, T) conditions. *J. Solid State Chem.* **2010**, *183*, 975–983. [[CrossRef](#)]
309. Winkler, B.; Juarez-Arellano, E.A.; Friedrich, A.; Bayarjargal, L.; Yan, J.; Clark, S.M. Reaction of titanium with carbon in a laser heated diamond anvil cell and reevaluation of a proposed pressure-induced structural phase transition of TiC. *J. Alloys Compd.* **2009**, *478*, 392–397. [[CrossRef](#)]
310. Juarez-Arellano, E.A.; Winkler, B.; Friedrich, A.; Wilson, D.J.; Koch-Müller, M.; Knorr, K.; Vogel, S.C.; Wall, J.J.; Reiche, H.; Crichton, W.; et al. Reaction of rhenium and carbon at high pressures and temperatures. *Z. Kristallogr. Cryst. Mater.* **2008**, *223*, 492–501. [[CrossRef](#)]
311. Bhadram, V.S.; Kim, D.Y.; Strobel, T.A. High-Pressure Synthesis and Characterization of Incompressible Titanium Pernitride. *Chem. Mater.* **2016**, *28*, 1616–1620. [[CrossRef](#)]
312. Niwa, K.; Terabe, T.; Kato, D.; Takayama, S.; Kato, M.; Soda, K.; Hasegawa, M. Highly Coordinated Iron and Cobalt Nitrides Synthesized at High Pressures and High Temperatures. *Inorg. Chem.* **2017**, *56*, 6410–6418. [[CrossRef](#)]
313. Binns, J.; Donnelly, M.-E.; Peña-Alvarez, M.; Wang, M.; Gregoryanz, E.; Hermann, A.; Dalladay-Simpson, P.; Howie, R.T. Direct Reaction between Copper and Nitrogen at High Pressures and Temperatures. *J. Phys. Chem. Lett.* **2019**, *10*, 1109–1114. [[CrossRef](#)] [[PubMed](#)]
314. Niwa, K.; Fukui, R.; Terabe, T.; Kawada, T.; Kato, D.; Sasaki, T.; Soda, K.; Hasegawa, M. High-Pressure Synthesis and Phase Stability of Nickel Pernitride. *Eur. J. Inorg. Chem.* **2019**, *2019*, 3753–3757. [[CrossRef](#)]
315. Ravindran, T.R.; Badding, J.V. UV Raman studies on carbon nitride structures. *J. Mater. Sci.* **2006**, *41*, 7145–7149. [[CrossRef](#)]
316. Horvath-Bordon, E.; Riedel, R.; McMillan, P.F.; Kroll, P.; Miede, G.; van Aken, P.A.; Zerr, A.; Hoppe, P.; Shebanova, O.; McLaren, I.; et al. High-Pressure Synthesis of Crystalline Carbon Nitride Imide, C<sub>2</sub>N<sub>2</sub>(NH). *Angew. Chem. Int. Ed.* **2007**, *46*, 1476–1480. [[CrossRef](#)]
317. Laniel, D.; Weck, G.; Loubeyre, P. Direct Reaction of Nitrogen and Lithium up to 75 GPa: Synthesis of the Li<sub>3</sub>N, LiN, LiN<sub>2</sub>, and LiN<sub>5</sub> Compounds. *Inorg. Chem.* **2018**, *57*, 10685–10693. [[CrossRef](#)]
318. Patel, N.N.; Meenakshi, S.; Sharma, S.M. LHDAC setup for high temperature and high pressure studies. *AIP Conf. Proc.* **2014**, *1591*, 664–665. [[CrossRef](#)]
319. Friedrich, A.; Winkler, B.; Bayarjargal, L.; Juarez Arellano, E.A.; Morgenroth, W.; Biehler, J.; Schröder, F.; Yan, J.; Clark, S.M. In situ observation of the reaction of tantalum with nitrogen in a laser heated diamond anvil cell. *J. Alloys Compd.* **2010**, *502*, 5–12. [[CrossRef](#)]
320. Åberg, D.; Erhart, P.; Crowhurst, J.; Zaug, J.M.; Goncharov, A.F.; Sadigh, B. Pressure-induced phase transition in the electronic structure of palladium nitride. *Phys. Rev. B* **2010**, *82*, 104116. [[CrossRef](#)]
321. Ismailova, L.; Bykova, E.; Bykov, M.; Cerantola, V.; McCammon, C.; Ballaran, T.B.; Bobrov, A.; Sinmyo, R.; Dubrovinskaia, N.; Glazyrin, K.; et al. Stability of Fe,Al-bearing bridgmanite in the lower mantle and synthesis of pure Fe-bridgmanite. *Sci. Adv.* **2016**, *2*, e1600427. [[CrossRef](#)] [[PubMed](#)]
322. Hikosaka, K.; Sinmyo, R.; Hirose, K.; Ishii, T.; Ohishi, Y. The stability of Fe<sub>5</sub>O<sub>6</sub> and Fe<sub>4</sub>O<sub>5</sub> at high pressure and temperature. *Am. Mineral.* **2019**, *104*, 1356–1359. [[CrossRef](#)]
323. Liu, J.; Sun, Y.; Lv, C.; Zhang, F.; Fu, S.; Prakapenka, V.B.; Wang, C.; Ho, K.; Lin, J.; Wentzcovitch, R.M. Iron-rich Fe–O compounds at Earth’s core pressures. *Innovation* **2023**, *4*, 100354. [[CrossRef](#)] [[PubMed](#)]
324. Dewaele, A.; Worth, N.; Pickard, C.J.; Needs, R.J.; Pascarelli, S.; Mathon, O.; Mezouar, M.; Irifune, T. Synthesis and stability of xenon oxides Xe<sub>2</sub>O<sub>5</sub> and Xe<sub>3</sub>O<sub>2</sub> under pressure. *Nat. Chem.* **2016**, *8*, 784–790. [[CrossRef](#)] [[PubMed](#)]

325. Hu, Q.; Kim, D.Y.; Liu, J.; Meng, Y.; Yang, L.; Zhang, D.; Mao, W.L.; Mao, H.-K. Dehydrogenation of goethite in Earth's deep lower mantle. *Proc. Natl. Acad. Sci. USA* **2017**, *114*, 1498–1501. [[CrossRef](#)] [[PubMed](#)]
326. Koemets, E.; Fedotenko, T.; Khandarkhaeva, S.; Bykov, M.; Bykova, E.; Thielmann, M.; Chariton, S.; Aprilis, G.; Koemets, I.; Glazyrin, K.; et al. Chemical Stability of FeOOH at High Pressure and Temperature, and Oxygen Recycling in Early Earth History. *Eur. J. Inorg. Chem.* **2021**, *2021*, 3048–3053. [[CrossRef](#)]
327. Santoro, M.; Gorelli, F.A.; Bini, R.; Salamat, A.; Garbarino, G.; Levelut, C.; Cambon, O.; Haines, J. Retraction Note: Carbon enters silica forming a cristobalite-type CO<sub>2</sub>-SiO<sub>2</sub> solid solution. *Nat. Commun.* **2016**, *7*, 13417. [[CrossRef](#)]
328. Santamaria-Perez, D.; McGuire, C.; Makhluף, A.; Kavner, A.; Chuliá-Jordan, R.; Jorda, J.L.; Rey, F.; Pellicer-Porres, J.; Martínez-García, D.; Rodríguez-Hernández, P.; et al. Correspondence: Strongly-driven Re+CO<sub>2</sub> redox reaction at high-pressure and high-temperature. *Nat. Commun.* **2016**, *7*, 13647. [[CrossRef](#)]
329. Scott, H.P.; Doczy, V.M.; Frank, M.R.; Hasan, M.; Lin, J.-F.; Yang, J. Magnesite formation from MgO and CO<sub>2</sub> at the pressures and temperatures of Earth's mantle. *Am. Mineral.* **2013**, *98*, 1211–1218. [[CrossRef](#)]
330. Nesper, R. Bonding Patterns in Intermetallic Compounds. *Angew. Chem. Int. Ed.* **1991**, *30*, 789–817. [[CrossRef](#)]
331. Lin, J.-F.; Gregoryanz, E.; Struzhkin, V.V.; Somayazulu, M.; Mao, H.-K.; Hemley, R.J. Melting behavior of H<sub>2</sub>O at high pressures and temperatures. *Geophys. Res. Lett.* **2005**, *32*. [[CrossRef](#)]
332. Sanjay Kumar, N.R.; Chandra Shekar, N.V.; Sahu, P.C. Development of Nd-YAG laser heated diamond anvil cell facility and HPHT synthesis of WGe. *AIP Conf. Proc.* **2013**, *1512*, 474–475. [[CrossRef](#)]
333. Yin, Y.; Akbar, F.I.; Bykova, E.; Aslandukova, A.; Laniel, D.; Aslandukov, A.; Bykov, M.; Hanfland, M.; Garbarino, G.; Jia, Z.; et al. Synthesis of rare-earth metal compounds through enhanced reactivity of alkali halides at high pressures. *Commun. Chem.* **2022**, *5*, 122. [[CrossRef](#)] [[PubMed](#)]

**Disclaimer/Publisher's Note:** The statements, opinions and data contained in all publications are solely those of the individual author(s) and contributor(s) and not of MDPI and/or the editor(s). MDPI and/or the editor(s) disclaim responsibility for any injury to people or property resulting from any ideas, methods, instructions or products referred to in the content.